


NUREG/CR-3438
SAND83-1692
R7
Printed August 1984

Report on Large Scale Molten Core/Magnesia Interaction Test

Tze Yao Chu, John H. Bentz, Frank E. Arellano
John E. Brockmann, Michael E. Field, Jim D. Fish

Prepared by
Sandia National Laboratories
Albuquerque, New Mexico 87185 and Livermore, California 94550
for the United States Department of Energy
under Contract DE-AC04-76DP00789



Prepared for
U. S. NUCLEAR REGULATORY COMMISSION

8411290150 841031
PDR NUREG
CR-3438 R FDR

NOTICE

This report was prepared as an account of work sponsored by an agency of the United States Government. Neither the United States Government nor any agency thereof, or any of their employees, makes any warranty, expressed or implied, or assumes any legal liability or responsibility for any third party's use, or the results of such use, of any information, apparatus product or process disclosed in this report, or represents that its use by such third party would not infringe privately owned rights.

Available from
GPO Sales Program
Division of Technical Information and Document Control
U.S. Nuclear Regulatory Commission
Washington, D.C. 20555
and
National Technical Information Service
Springfield, Virginia 22161

NUREG/CR-3438
SAND83-1692
R7

REPORT ON LARGE SCALE MOLTEN CORE/MAGNESIA
INTERACTION TEST

Tze Yao Chu, John H. Bentz
and
Frank E. Arellano, John E. Brockmann,
Michael E. Field, Jim D. Fish

Date Published: August 1984

Sandia National Laboratories
Albuquerque, New Mexico 87185
Operated by
Sandia Corporation
for the
U.S. Department of Energy

Prepared for
Division of Reactor Safety Research
Office of Nuclear Regulatory Research
U. S. Nuclear Regulatory Commission
Washington, DC 20555
Under Memorandum of Understanding DOE 40-550-75
NRC FIN No. A-1227

NUREG/CR-3438
SAND83-1692
R7

Tze Yao Chu, John H. Bentz
and
Frank E. Arellano, John E. Brockmann,
Michael E. Field, Jim D. Fish

Sandia National Laboratories
Albuquerque, New Mexico 87185

ABSTRACT

A molten core/material interaction experiment was performed at the Large-Scale Melt Facility at Sandia National Laboratories. The experiment involved the release of 230 kg of core melt, heated to 2923°K, into a magnesia brick crucible. Descriptions of the facility, the melting technology, as well as results of the experiment, are presented. Preliminary evaluations of the results indicate that magnesia brick can be a suitable material for core ladle construction.

Table of Contents

	<u>Page</u>
Executive Summary	xiii-xiv
Acknowledgement	xii
I. Objective of the Test	1
a. Feasibility of Magnesia Brick Core Retention Concept	1-2
b. Role of Core Retention in Accident Mitigation	2-3
c. Experimental Verification of Recent Developments in Melting Technology	3
II. Physical Description of Test	5
a. Large-Scale Melt Facility (LMF)	5-8
b. Charge	8-15
c. Crucible for Melting	15-27
d. Magnesia Brick Crucible	27
e. Instrumentation	27-47
III. Events of the Test	47
a. Heating and Melting	47-60
b. CO Data	60
c. Displacement Gauge Data	60-63
d. Tapping	63-64
IV. Data From Test	64
a. Aerosol Data	64-80
b. Gas Data	80
c. Temperature Data	80-91
d. The Upward Heat Flux	91
e. Brick Cracking Data	91-108

Table of Contents (cont)

	<u>Page</u>
V. Early Stages of Post-Test Dissection	108
a. Melt Crucible	108-116
b. MgO Crucible	116
VI. Ongoing Analysis	116
a. Melt Crucible	116-119
b. MgO Crucible	119
c. MgO Thermal Test and Modeling of Thermal Process	119
VII. Future Improvements in Melting Technology	119
a. Tungsten Liner	119-120
b. Tapping	120
c. Temperature Measurements	120
VIII. Concluding Remarks	120-121
References	122

List of Figures

			Page
Figure	I.1	A Schematic of the LMF Furnace	4
Figure	II.1	Schematic of the Graphite Susceptor	6
Figure	II.2	Furnace Susceptor Bottom Support and Radiation Shield Assembly	7
Figure	II.3	LMF Furnace and Test Chamber	9
Figure	II.4	Shotgun Tapping Assembly	10
Figure	II.5	Typical Pressure and Temperature Histories for Manufacturing the Charge	11
Figure	II.6	Thermal Conductivity of the Charge, "Corrected" Value	13
Figure	II.7	The Melt Charge Assembly	14
Figure	II.8	Schematic of the Multi-Walled Crucible Assembly	16
Figure	II.9	Melt Interaction Zone in Tungsten	17
Figure	II.10	Melt Interaction Zone in Ta-10W	18
Figure	II.11	Photograph of Ta-10W Crucible with Thickness Measurement Marked	20
Figure	II.12	Schematic of CVD Liner Mandrel	21
Figure	II.13	A Typical CVD Processing Furnace	22
Figure	II.14	Charge/Crucible/Susceptor Assembly	24
Figure	II.15	Crucible and Charge Loading Fixture	25
Figure	II.16	Vacuum Chucks for Holding the Charge and Liner	26
Figure	II.17a	MgO Crucible Cavity Brick Pattern	29-30
Figure	II.17b	MgO Crucible Cavity	31
Figure	II.18	Schematic of Instrumentation Placement in the Charge and the Susceptor	32
Figure	II.19	Placement of Aerosol Instrumentations	38
Figure	II.20	Chamber Aerosol Sampling System	39

List of Figures (cont)

	Page
Figure II.21 Instrumentation Boom	41
Figure II.22a Bottom Thermocouple Locations	42
Figure II.22b Bottom Thermocouple Depths	43
Figure II.23a Sidewall Thermocouple Locations (Pool Region)(See Figure II.17a for Brick Locations)	44
Figure II.23b Sidewall Thermocouple Locations (Upper Region)(See Figure II.17a for Brick Locations)	45
Figure II.24 View of Cavity Bottom	46
Figure II.25 Electrical Schematic for Conductive Element Array of Thick Film Crack Detector	48
Figure II.26 Schematic of Brick with Crack Detection Elements	49
Figure II.27 Instrumented Brick in Partially-Assembled Crucible	50
Figure III.1 Pre-Test Thermal Calculation (Melt Thermal Conductivity 2.068 Btu/hr-in-°F, 42.9 W/mK)	53
Figure III.2 Comparison Between Pre-test Prediction and Actual Temperature History	54
Figure III.3a Susceptor and Charge Temperature During Test	55
Figure III.3b Power (Applied) History	56
Figure III.4 Comparison Between Pyrometer and Thermocouple Measurements of the Susceptor Temperature	58
Figure III.5 Comparisons of Susceptor UTs and Corresponding Thermocouples and Pyrometers	59
Figure III.6 CO Concentration in the Furnace	61
Figure III.7 Displacement Gauge Data	62

List of Figures (cont)

		Page
Figure IV.1	Aerosol Sampling Scheme	66
Figure IV.2a	Aerosol Sample Size Distribution, 0.0-1.0 Minutes	67
Figure IV.2b	Aerosol Sample Size Distribution, 2.0-5.0 Minutes	68
Figure IV.2c	Aerosol Sample Size Distribution, 10.0-15.0 Minutes	69
Figure IV.2d	Aerosol Sample Size Distribution, 15.0-30.0 Minutes	70
Figure IV.3a	Aerosol Sample Size Distribution (Accumulative), 0.0-1.0 Minutes	71
Figure IV.3b	Aerosol Sample Size Distribution (Accumulative), 2.0-5.0 Minutes	72
Figure IV.3c	Aerosol Sample Size Distribution (Accumulative), 10.0-15.0 Minutes	73
Figure IV.3d	Aerosol Sample Size Distribution (Accumulative), 15.0-30.0 Minutes	74
Figure IV.4	Aerosol Concentration Versus Time, Filter Data	75
Figure IV.5a	Aerosol Concentration Versus Time, Experimental Data and Maeros Runs	78
Figure IV.5b	Aerosol Deposition Rate versus Time Experimental Data and Maeros Runs	79
Figure IV.6	N ₂ and O ₂ Volume Percent Versus Time A-1	82
Figure IV.7	CO ₂ Volume Percent Versus Time	83
Figure IV.8	CO ₂ Volume Percent Versus Time	84
Figure IV.9	Ar Volume Percent Versus Time	85
Figure IV.10a	O ₂ /N ₂ Ratio Versus Time	86
Figure IV.10b	O ₂ /CO ₂ Ratio Versus Time	87
Figure IV.11	Temperature Responses on the Bottom of the Crucible, 1/2 in. Below the Surface 1.75 in. and 5.5 in. from Center of Crucible	88

List of Figures (cont)

		<u>Page</u>
Figure	IV.12 Thermal Responses in the Bottom of the Crucible	89
Figure	IV.13 Thermal Responses in the Bottom of the Crucible	90
Figure	IV.14 Temperature Histories in Cracks	92
Figure	IV.15 Temperature Responses in the Sidewall, Brick #1	93
Figure	IV.16 Temperature Responses in the Sidewall, Brick #4	94
Figure	IV.17 Temperature Responses in the Sidewall, Brick #7	95
Figure	IV.18 Temperature Responses in the Sidewall, Brick #13	96
Figure	IV.19 Temperature Responses in the Sidewall, Brick #16	97
Figure	IV.20 Temperature Responses in the Sidewall, Brick #19	98
Figure	IV.21 Schematic of Instrumentation in the Shield	99
Figure	IV.22 Heat Flux Impinging on the Nickel Heat Flux Gauge	100
Figure	IV.23 Heat Flux into the Heat Shield at Locations: A, C, E	101
Figure	IV.24 Temperature Profiles for Semi-Infinite Body Exposed to a Constant Temperature on One Surface	103
Figure	IV.25 Brick Isotherms Near the Floor of the Cavity	103
Figure	IV.26 Brick Temperature Data	105
Figure	IV.27 Recorded Data from Crack Detection Sensors	106
Figure	IV.28 Diagonal Crack Patterns Seen in Molten Thermite Tests	107

List of Figures (cont)

		<u>Page</u>	
Figure	V.1a	View of Bottom of Melt Crucible	109
Figure	V.1b	View of Bottom of Melt Crucible	110
Figure	V.2	Melt Crucible After the Test	111
Figure	V.3	Melt Crucible After the Test - A Closer View	112
Figure	V.4	A View of Inside of the Melt Crucible	113
Figure	V.5	Break in the Melt Crucible Above the Melt Line	114
Figure	V.6	Crack Like Break in the Liner	115
Figure	V.7	Bottom of Melt Crucible with Melt Charge Removed	117
Figure	V.8	Top View of Magnesia Crucible	118

List of Tables

Table	III.1	Heating Schedule for the Susceptor	52
Table	IV.1	Sampling Scheme for Aerosol	65
Table	IV.2	MAEROS Calculations	77
Table	IV.3	Gas Generation Data	81

Acknowledgement

The authors would like to acknowledge A.W. Mullendore (1831), F.J. Zanner (1833) and R.W. Fisher (1831) for their contribution in material studies, fabrication technology and furnace operation. Separate reports covering these subjects will be issued in the future.

Executive Summary

The largest interaction experiment ever conducted with prototypic core material, was carried out at the Large-Scale Melt Facility (LMF) at Sandia National Laboratories. In the experiment, 230 kg of a 70% UO_2 -30% ZrO_2 mixture was melted and drained into a magnesia brick crucible. The main objective of the test was to assess the use of magnesia bricks as a possible material for a core ladle in a nuclear reactor.

The melt was contained in a multi-walled refractory metal crucible. The heating and melting phase of the experiment lasted approximately twenty hours. The thermal response of the melt charge was found to be well predicted by pretest calculations. At the time of tapping, the melt was at 2923 K (2650°C). Approximately four minutes were required to drain all the melt into the magnesia interaction crucible.

The melt/magnesia interaction was relatively mild. No detectable amount of hydrogen was generated and aerosol production was minimal. The total production was estimated to be between 29 and 103 grams. Extrapolating to the reactor core (8×10^5 kg), the corresponding aerosol generation would be between 12 and 41 kg. The brick structure remained intact. Hairline cracks were observed but none was large enough to threaten the structural integrity of the crucible. No deep penetration of the melt into the crack was observed. The maximum temperature measured 1/8 in. beneath the surface of the brick was about 700°C and the upward heat flux as measured above the pool was in the range of $40W/cm^2$. Detailed analyses of the interaction are underway. Preliminary results seem to indicate the magnesia bricks to be a suitable candidate for core ladle construction.

I. Objective of the Test

A molten core material/MgO interaction test was carried out at Sandia. The main objective of the test was to study the core debris interactions with magnesia bricks for the FNP (floating nuclear plant) core ladle. In addition, the test also provided experimental verifications of recent advances made in melting technology.

a. Feasibility of Magnesia Brick Core Retention Concept

Core retention devices constitute one of several approaches that have been considered for mitigation of severe accidents at nuclear reactor plants. The unique feature of core retention is the possibility of suppressing the formation of fission-product-laden aerosols, steam, and gases instead of attempting to remove the various source terms after their creation.

A magnesia brick structure has been proposed as a core ladle for both floating nuclear plants [1] and for the Clinch River Breeder Reactor parallel design [2]. The primary advantage of the refractory brick concept is that it represents an inexpensive technique commonly practiced in the steel industry. The primary concerns with the concept include premature penetration of the cracks and spaces in the brick matrix by molten debris, gross failure of the crucible by floatation of bricks in the more dense debris, and the difficulty of assuring long-term coolability of the device and the contained debris.

These concerns and several of the phenomena to which they are related were addressed by this test:

(1) Mechanical Damage -- The test crucible included two bricks instrumented with crack detectors designed to show the formation of cracks resolved in both time and space. Early cracking, before the debris solidifies, can lead to premature penetration of the device by molten material. The combination of cracking and chemical attack of the penetrated cracks could lead to rapid, gross failure of the device.

(2) Chemical Interaction -- Evidence for chemical interactions between the debris and magnesia were sought in the gas samples taken during the test and in the posttest inspection of the sidewalls of the crucible.

(3) Thermal Partitioning -- Data from both heat-flux gauges and thermocouples were used to develop a heat balance for the debris cooling. Large sidewall and bottom heat fluxes would be advantageous

for cooling of the device and the contained debris. At the same time, large heat losses through the magnesia would imply rapid heatup of underlying structures. The effect of upward heat loss is no more clear-cut. That heat which is radiated from the top of the debris reduces the amount available to drive erosion of the device. Degradation of overhead structures by radiant energy, however, is a concern.

(4) Gap Penetration -- A series of calibrated slits was cut in one of the bricks used for the bottom of the crucible. Penetration of these cracks will give some indication of the care that must be taken in fitting together a brick matrix and of the possibility of device failure resulting from penetration of the spacing required for thermal expansion.

b. Role of Core Retention in Accident Mitigation

Sources of steam, gas, aerosol and fission products during a severe reactor accident can be divided into three categories: (1) those produced in-vessel; (2) those produced during expulsion of molten material from the primary vessel; and (3) those produced ex-vessel by interactions of the core debris with coolant and with structural or retention material in the reactor cavity.

The primary functional requirement of a core retention device is to delay, reduce, and in some cases, eliminate ex-vessel sources of steam, combustible gases, aerosols, and fission products.

VANESA* code calculations indicate that the integral aerosol source term due to core/concrete interactions, for example, is in the range of 3800 to 5000 kg for a reactor-scale melt release of 80,000 kg. In comparison, estimates of the in-vessel aerosol source term is in the range of 500 to 1000 kg. Clearly, eliminating core/concrete interactions can significantly reduce the aerosol load in containment. This reduction, in turn, can reduce the consequences of severe accidents by removing the major mechanism by which the more refractory fission products become airborne, and by assuring the proper performance of other mitigation devices that could be degraded by large aerosol loads.

One objective of the current test was to measure the aerosols produced during melt deposition and as a result of core/MgO interactions, and to compare these sources to the other aerosol source terms. As expected, aerosol production during the test was quite low.

The other source term measured during the test was gas production. This source term was also expected to be low. The only source of water is water of hydration in the MgO bricks. Some of this water

*VANESA is a mechanistic model of fission product release and aerosol generation during core debris interactions with concrete. The details of the code can be found in: D.A. Powers and J.E. Brockmann, Appendix C to BMI-2104 Vol. 1 (draft), Jan. 1983.

will be driven off and will interact with the molten material to produce hydrogen. Hydrogen production should be orders of magnitude less than if the melt were dropped onto concrete.

c. Experimental Verification of Recent Developments in Melting Technology

A schematic of the LMF furnace is shown in Figure I.1. The melt charge is contained in a multi-walled refractory metal crucible and the crucible is contained inside of a cavity in a graphite susceptor. The inductive power is coupled to the graphite susceptor which in turn heats the crucible and the charge inside. An opening is left on the bottom of the susceptor to facilitate tapping of the melt.

There have been a number of recent developments in the areas of heating procedure, melt containment technology and tapping of the crucible. The present test provides the opportunity for experimental verification of these developments under real conditions.

(1) Heating Procedure

Because of the brittleness of parts of the melt crucible assembly at low temperature, the poor thermal properties of the melt charge, and the proximity of the melting range of the charge and the failure point of the melt crucible, the heating procedure must be carefully designed to achieve successful melting. A thermal model of the susceptor-crucible-charge assembly was made first to assist in the design of the assembly and then to design a heating procedure for the test [3]. In this test the thermal modeling of the test was evaluated.

(2) Melt Containment Technology

The melt crucible must be able to withstand concurrently both the diffusion of carbon from the susceptor on the outside and the possible attack of the melt from the inside. Material compatibility tests at Sandia showed that no such material existed. Therefore, the crucible had to be a multi-walled structure with tantalum-10 W/O tungsten on the outside to resist carbon attack and tungsten inside to be compatible with the molten oxides. After materials were selected, manufacturing and assembly techniques were developed to fabricate the crucible. This test provides a check on the overall integrity of the crucible.

(3) Tapping

Once the melt is produced, the crucible is tapped by firing two slugs from a double barrel shotgun mounted on a swing arm. Extensive tests were made in the selection of the material for the slug, the amount of propellant to drive the slug, and the aiming and arming of the gun, the logical controls of the firing sequence, and emergency measures in case of failure to tap.

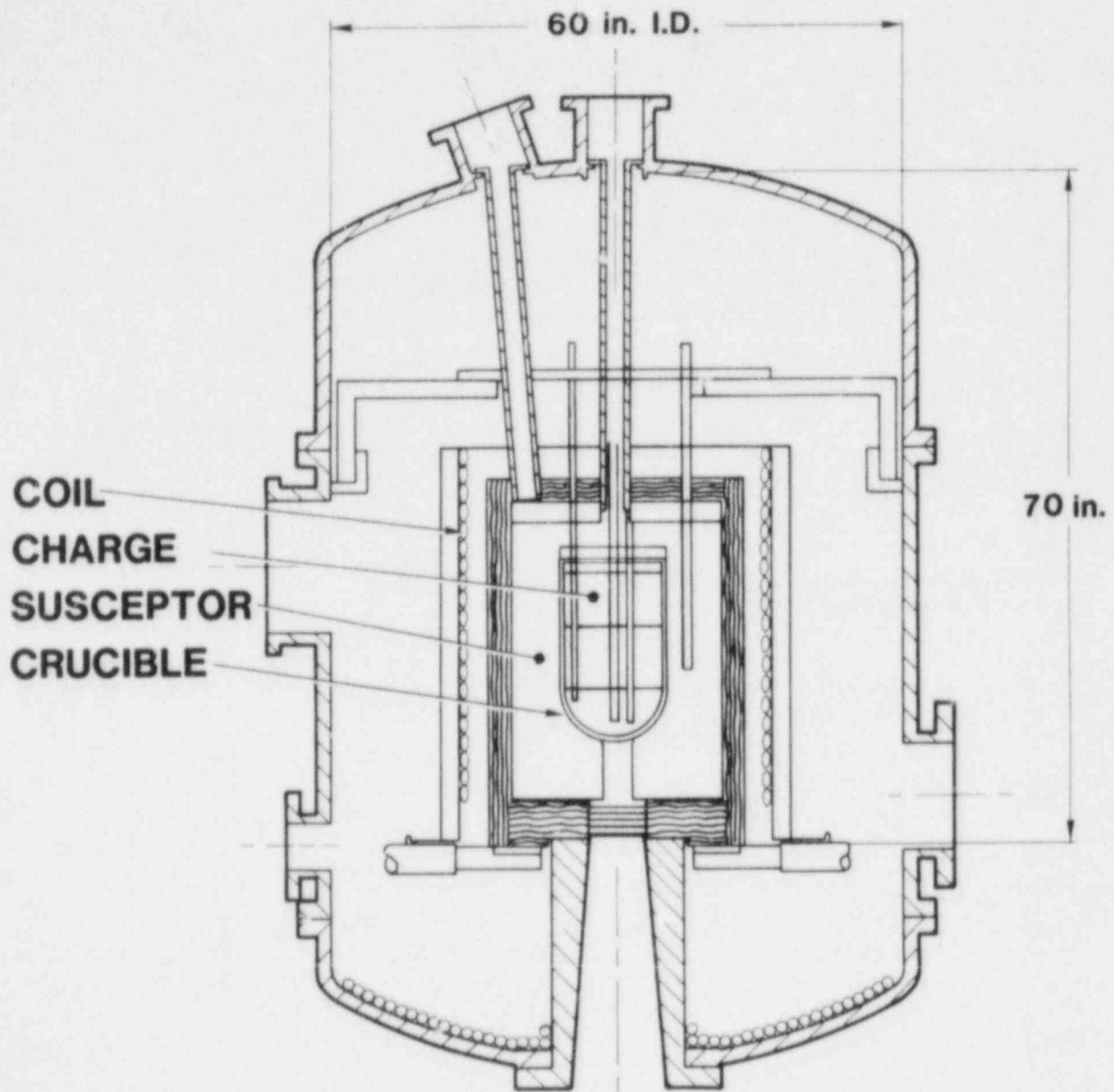


Figure I.1 A Schematic of the LMF Furnace

II. Physical Description of Test

a. Large-Scale Melt Facility (LMF)

(1) Furnace

The induction melting furnace is approximately 5 ft. in diameter and 7 ft. tall. It has a water cooled outer shell. The outside shell temperature never exceeds 308 K (35°C) during operation. The furnace is designed for a maximum internal pressure of 15 psig. During normal operation the furnace operates at approximately 2 psig, 740 mm absolute. The furnace is purged continuously with argon at a nominal rate of 500 ft³/hr. (equivalent to four change-overs of the furnace atmosphere per hour). A vacuum pump and a regulating valve (3/4 in.) are used to keep the furnace at the desired operating pressure. There is a pressure relief port on the side of the tank set at 3 psig. The relief port is spring loaded; it can reseal after a pressure transient.

The induction coil measures 31-in. I.D. x 37-in. long, wound in 4 sections with 20 mechanical turns or 5 electrical turns. The coil is made of hollow copper tubes 1 1/2 in. high x 3/4 in. wide with a wall thickness 0.148 in. The induction power is coupled to a graphite susceptor which in turn heats the crucible containing the charge. The induction power supply has a maximum power of 280 kW. It operates in the range of 1000 to 1200 Hz. The average coupling efficiency between the coil and the susceptor was experimentally determined to be 0.55. Therefore, the maximum power deposition into the susceptor is 154 kW.

The susceptor is made of HLM graphite. It has an overall outside diameter of 22 in., a height of 30 in. and a 4-in. thick sidewall, 6-in. thick bottom and 2-in.-thick lid. The susceptor cavity has a hemispherical bottom, see Figure II.1. There is a 4-in. diameter opening on the bottom of the susceptor for bottom tapping of the melt. The susceptor is supported from below with eight equally spaced graphite legs 1-in. diameter and 5-in. long on a 10 in. diameter circle. Four pyrolytic graphite disks 3/8-in. thick, 6-in. I.D. and 13 5/8-in. O.D. with the appropriate hole pattern for the legs to pass through provide for lateral support of the legs, see Figure II.2. The legs rest on a water cooled copper pedestal bolted to the furnace bottom shell. The susceptor is insulated with 2 in. (8 layers) of carbon felt on the top and the side. The bottom is insulated with 5 in. of carbon felt. To provide the flow path for the melt, a 4-in. diameter hole is left in each layer of the bottom felt. Radiation shields made of 0.004 in. thick GRAFOIL® are placed between each layer of the felt to reduce the heat loss from the bottom of the crucible, Figure II.2. There are in all 12 radiation shields. To drive out volatile contaminants that might be harmful to the crucible and interfere with pyrometry measurements, the susceptor assembly was preheated for a total of 20 hours above 3073 K (2800°C) before the test.

(2) The Test Chamber

The furnace is located on a platform, 15 ft. by 20 ft. and 15 ft. high; the top 2/3 of the furnace extends above the platform,

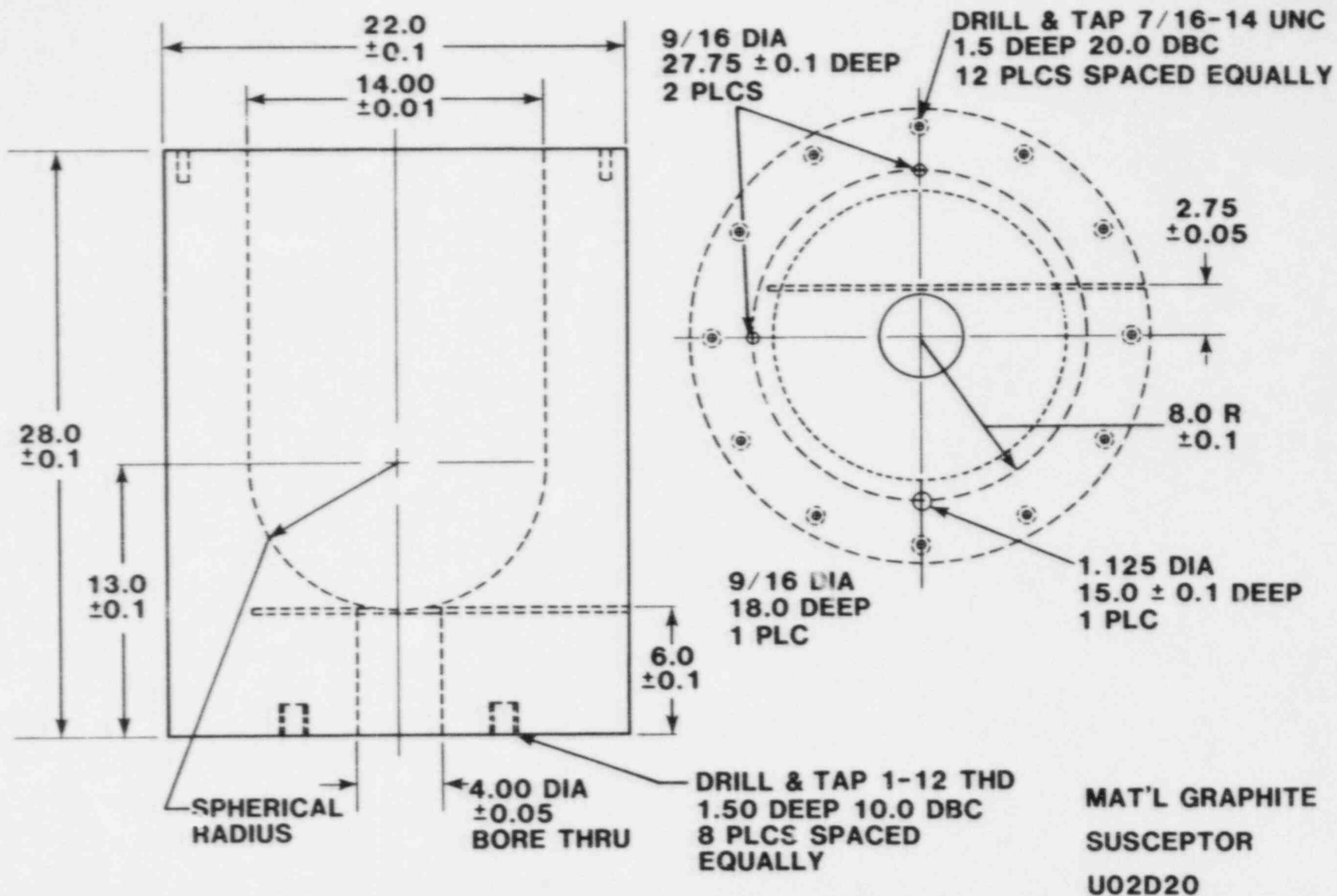


Figure II.1 Schematic of the Graphite Susceptor

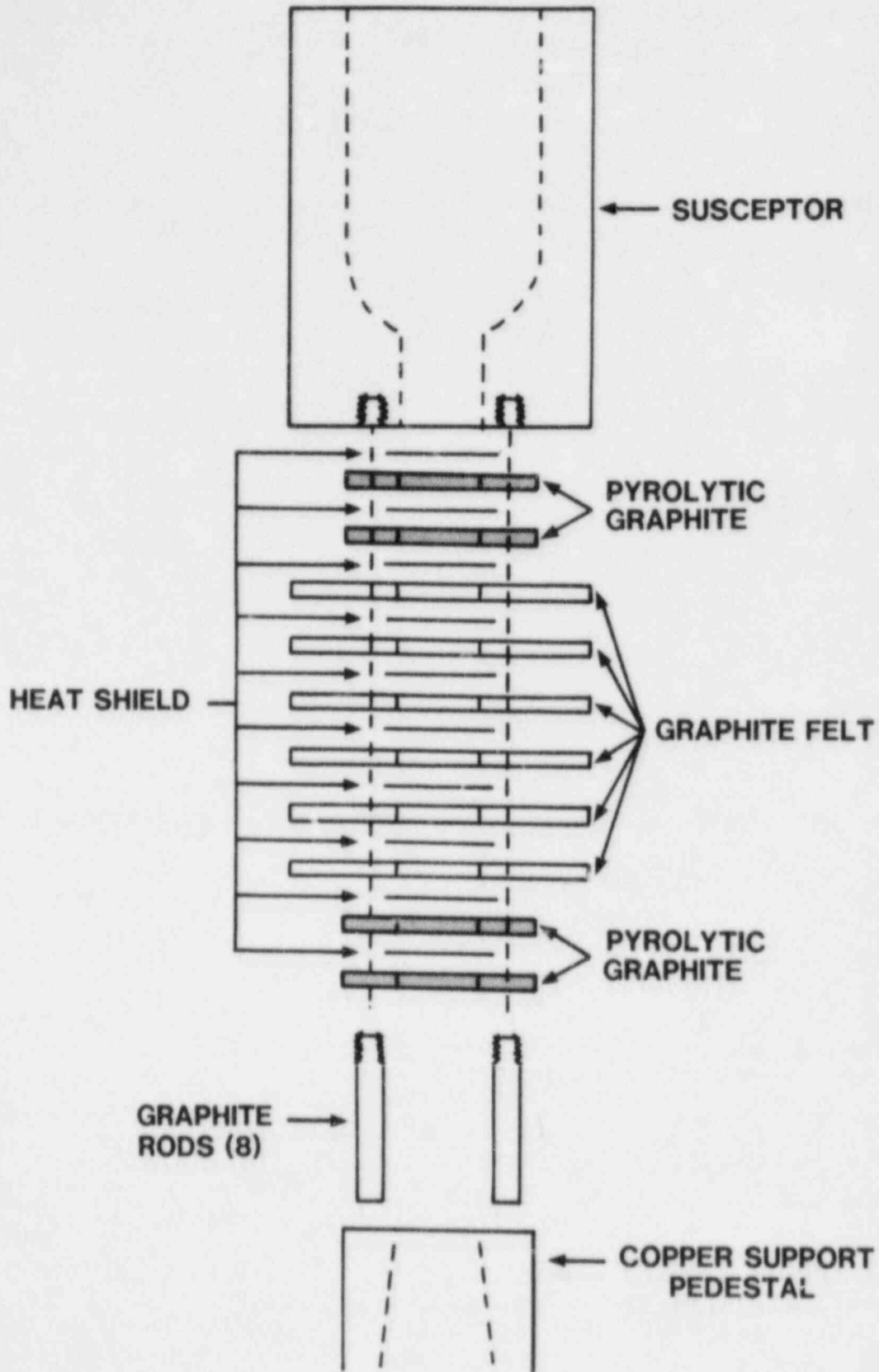


Figure II.2 Furnace Susceptor Bottom Support and Radiation Shield Assembly

Figure II.3. A concrete test pad is located directly under the platform, it extends an additional 20 ft. eastward beyond the platform. An interaction chamber rides on a pair of tracks running east and west on the test pad. The chamber can be moved east beyond the platform so that the furnace and the test chamber can be worked on independently. During the test, the chamber is placed directly under the furnace. The interaction chamber is 9 ft. in diameter and 8 ft. high, made of 1/4 in. mild steel, with external girdling beams; it can withstand an internal pressure of 30 psig. The chamber has a relief port of the same design as the furnace. There are four observation ports, one on top and three on the side of the chamber to provide for television and motion picture coverage of the test. There are also various instrumentation ports through the chamber wall for gas and aerosol measurements; the details of which will be discussed in later sections. For the present test the chamber is provided with a 2 in. exhaust tube. The end of the tube has an expanded section filled with glass wool as a particle trap.

(3) Tapping

The melt crucible is tapped from the bottom using a 12-gauge double barrel shotgun. The shotgun is mounted on a pivoting arm, Figure II.4; within 0.2 seconds after firing an air cylinder pushes the gun assembly out of the path of the melt stream. Aiming is accomplished by placing two bore sight plugs in each end of a barrel and shining a laser beam through the barrel. The gun is then positioned with adjustment bolts until the laser spot is in the center of the crucible hemisphere.

The shotgun is remotely armed and fired using air cylinders. The tapping sequence is controlled by the data acquisition computer, but if a malfunction occurs, the shotgun and associated components can be controlled with manual overrides. If the projectiles do not penetrate the crucible, the shotgun can be reloaded from outside of the test chamber using access ports.

b. Charge

(1) Fabrication Technique

The charge material is a mixture of urania, 70% by weight and the balance zirconia (stabilized by 12% yttria). The raw materials for the charge are in powder form with typical packing density of about 30%. To increase the amount of charge and more importantly, to improve the thermal properties of the melt charge, the powders were hot pressed to approximately 80% of theoretical density.

The pressings were manufactured at Los Alamos National Laboratory in a 400 ton press. The graphite die was inductively heated with a 175 kW, 960 Hz power supply. Cylindrical pressings approximately 12 in. in diameter and 3 to 5 in. high were made. The maximum pressing temperature and pressure were approximately 1623 K (1350°C) and 2000 psi, respectively. A typical pressure-temperature curve is shown in Figure II.5. After the die was loaded, an initial pressure of 1000

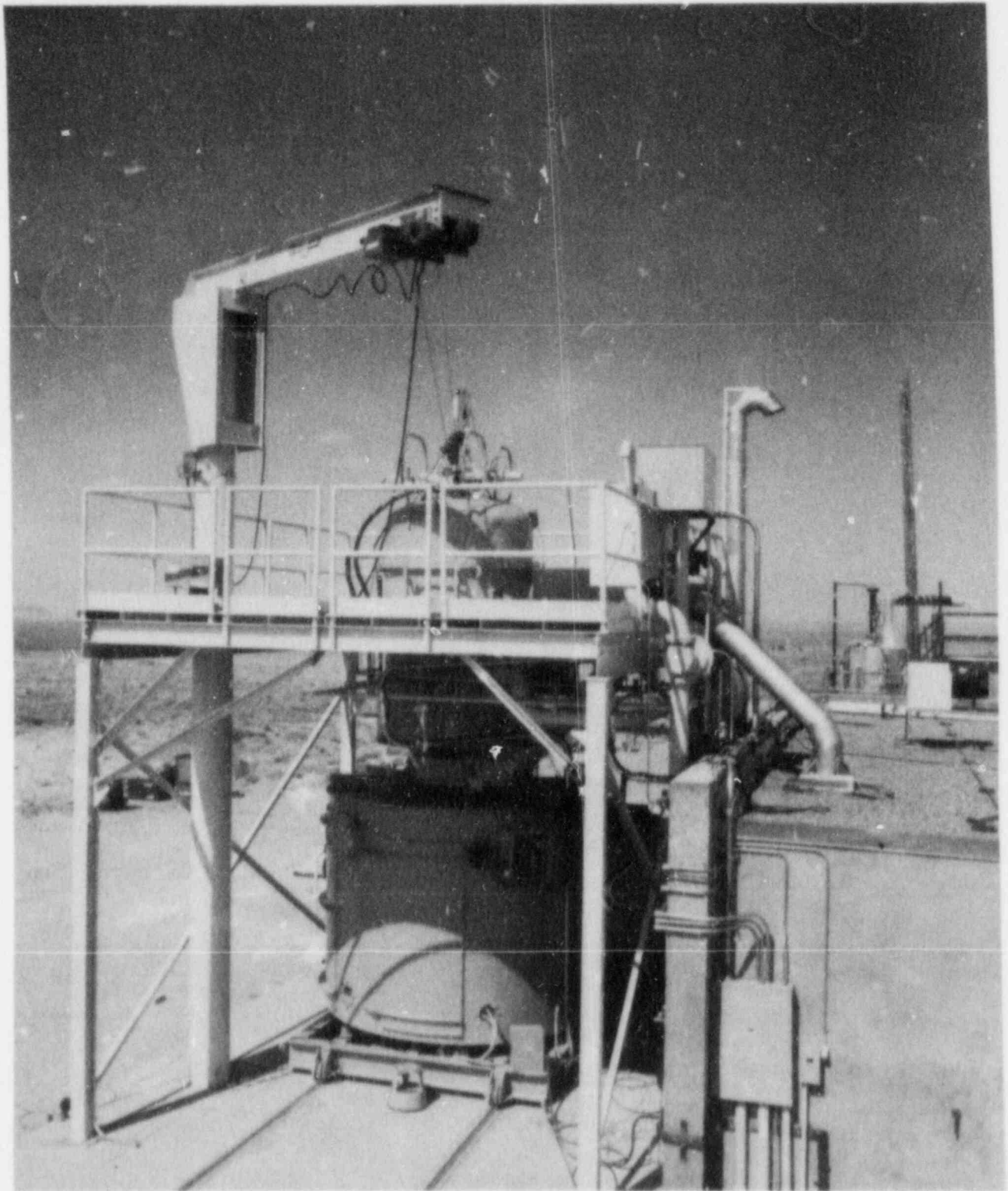


Figure II.3 LMF Furnace and Test Chamber

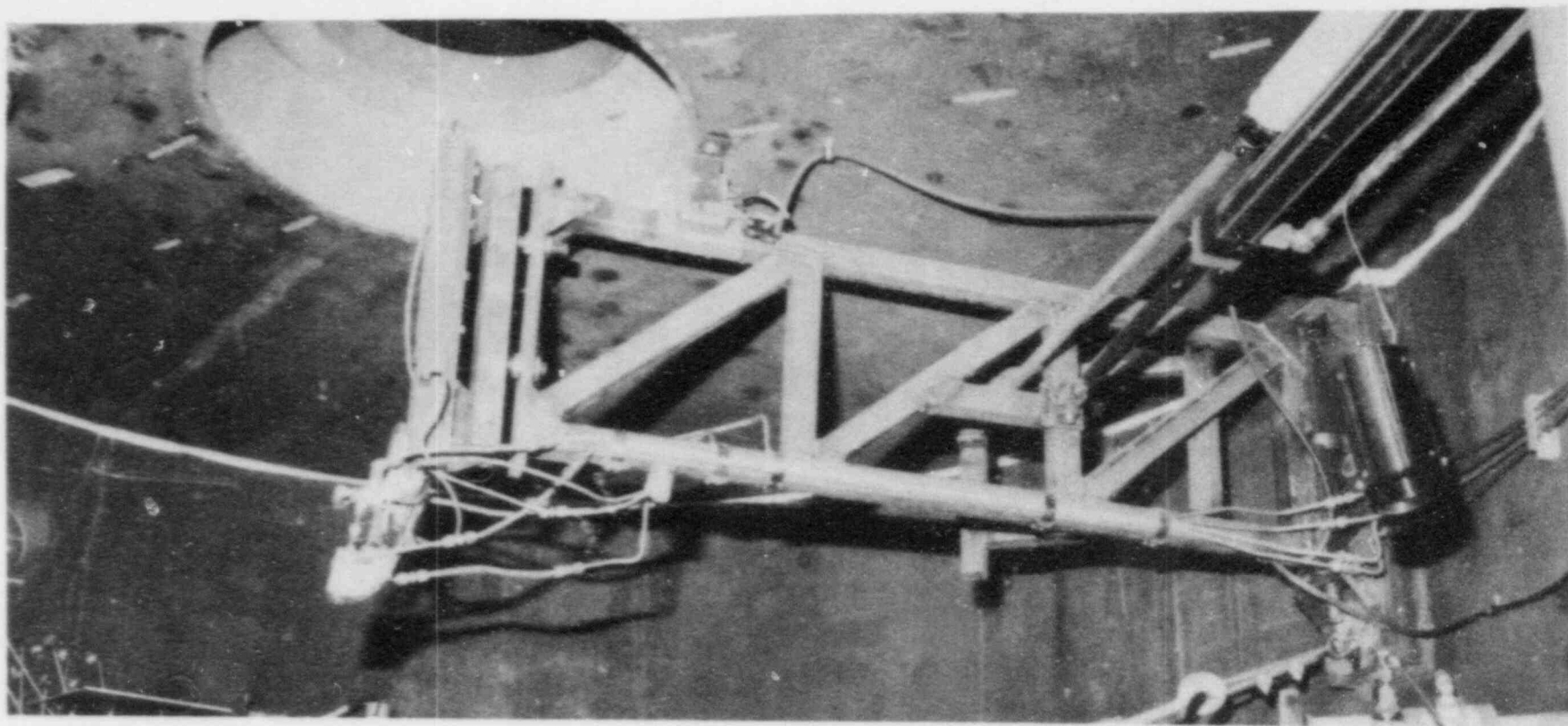


Figure II.4 Shotgun Tapping Assembly

TEMP/PRESS. FOR UO2/ZR02

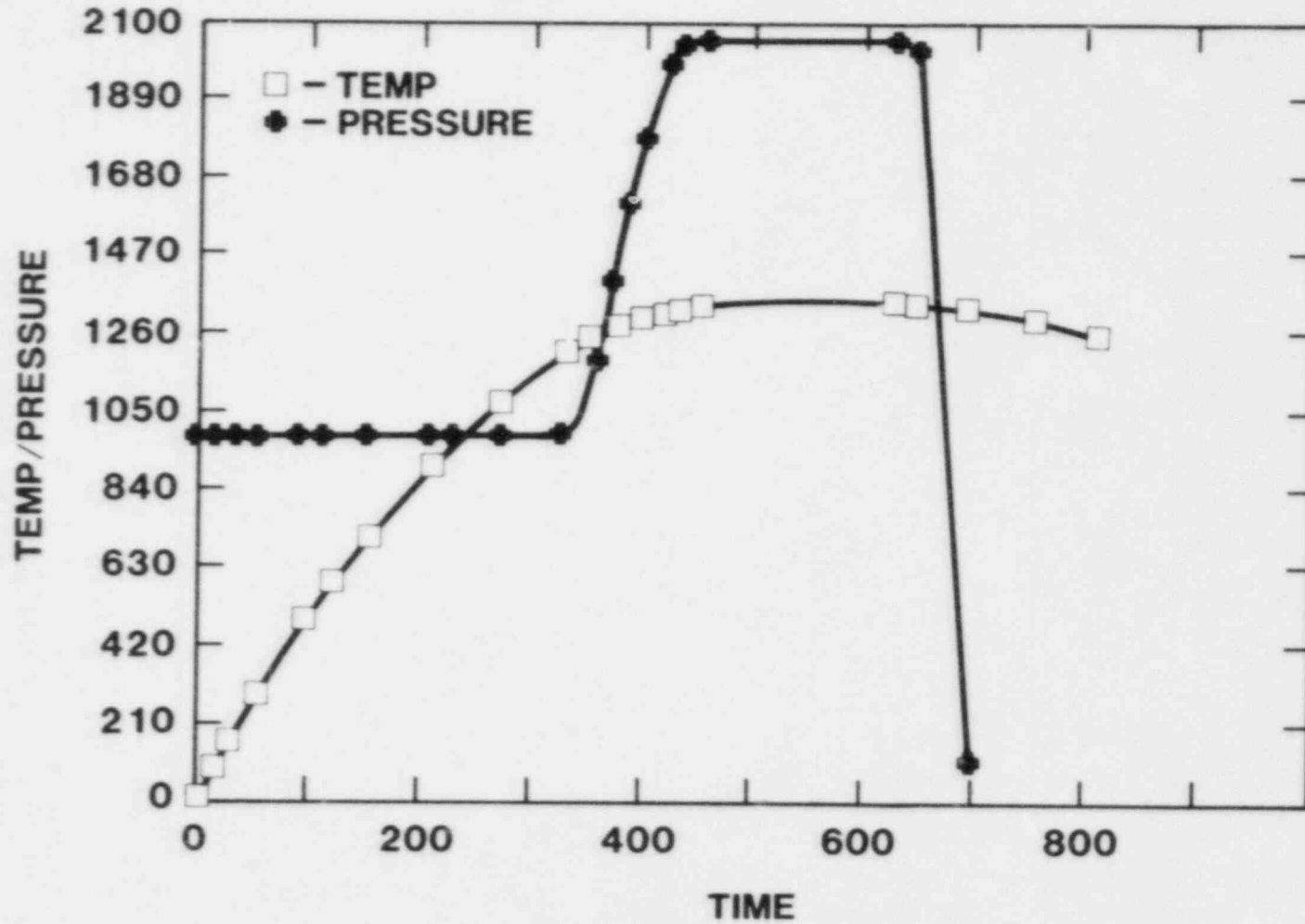


Figure II.5 Typical Pressure and Temperature Histories for Manufacturing the Charge

psi was applied. At 5.5 hr. the die reached a temperature of 1273 K (1000°C) and the pressure was gradually increased toward 2050 psi. At 6.5 hr. the maximum pressure of 2050 psi and maximum temperature of 1623 K (1350°C) were reached. This condition was held for 3 hr., after which the pressure was released and the power to the die was reduced to maintain a cooling rate of 25°C/hr. until a temperature of 1023 K (850°C). Beyond 1023 K the die was allowed to cool naturally. The entire pressing process took six days. The final product is typically 80% of theoretical density. The hot press process produced a thin (~0.01 in.) carbide layer on the surface of the pressing which had to be removed by machining.

(2) Charge Properties

To model the heating of the charge, the thermal properties of the charge must be accurately known. Values calculated from standard mixture rules were found to be inadequate in reproducing the thermal histories of previous LMF tests. While no experimental data is available for the present charge mixture, experimental data does exist for a $\text{UO}_2/\text{Y}_2\text{O}_3$ (UO_2 70% by weight) charge manufactured exactly the same way as the UO_2/ZrO_2 charge using the same batch of UO_2 powder. A comparison of the values of thermal diffusivity of the $\text{UO}_2/\text{Y}_2\text{O}_3$ charge determined experimentally by TRPL [4] and estimated by M. Pilch [5] showed the estimated values, based on mixture rules, to be too high. The ratio of the two sets of values varies from 0.36 near room temperature to 0.95 beyond 2500 K. Because density and specific heat can be estimated with much better accuracy, the discrepancy comes mainly from thermal conductivity. This set of ratios was applied to the estimated thermal conductivity of UO_2/ZrO_2 charge to obtain a "corrected" set of thermal conductivity for use in the final calculation, Figure II.6. The packed powder was assumed to be 30% dense and its thermal conductivity was calculated from the "corrected" values using the Godbee and Zeigler [6] formula. With the corrected set of properties, the thermal histories of the previous LMF test were reproduced within 100°C up to 2673 K (2400°C) [3].

The liquidus temperature of the melt charge, 70% UO_2 and 30% ZrO_2 (stabilized by 12% Y_2O_3), was established in two independent sets of experiments at Sandia, by X-ray diffraction analysis of various heated samples in one case and by direct posttest metallurgical examination in the other case. The two sets of experiments were within 25°C of each other. The melting range for the mixture was found to be between 2798 K and 2848 K (2525°C and 2575°C).

(3) Physical assembly of the charge

Diamond tools were used to machine the charge pieces to size from pressings. Freon was used as a lubricant during machining. The final charge assembly consisted of five pieces, Figure II.7, four upright cylinders and one with a hemispherical bottom. The bottom and the top pieces were cracked. To keep the bottom piece in place, a counter sink was machined in the piece above it. A center hole of 1.25 in. diameter was machined in the charge assembly to accept a pyrometer well. In addition there were two holes at the 2 in. radius and two

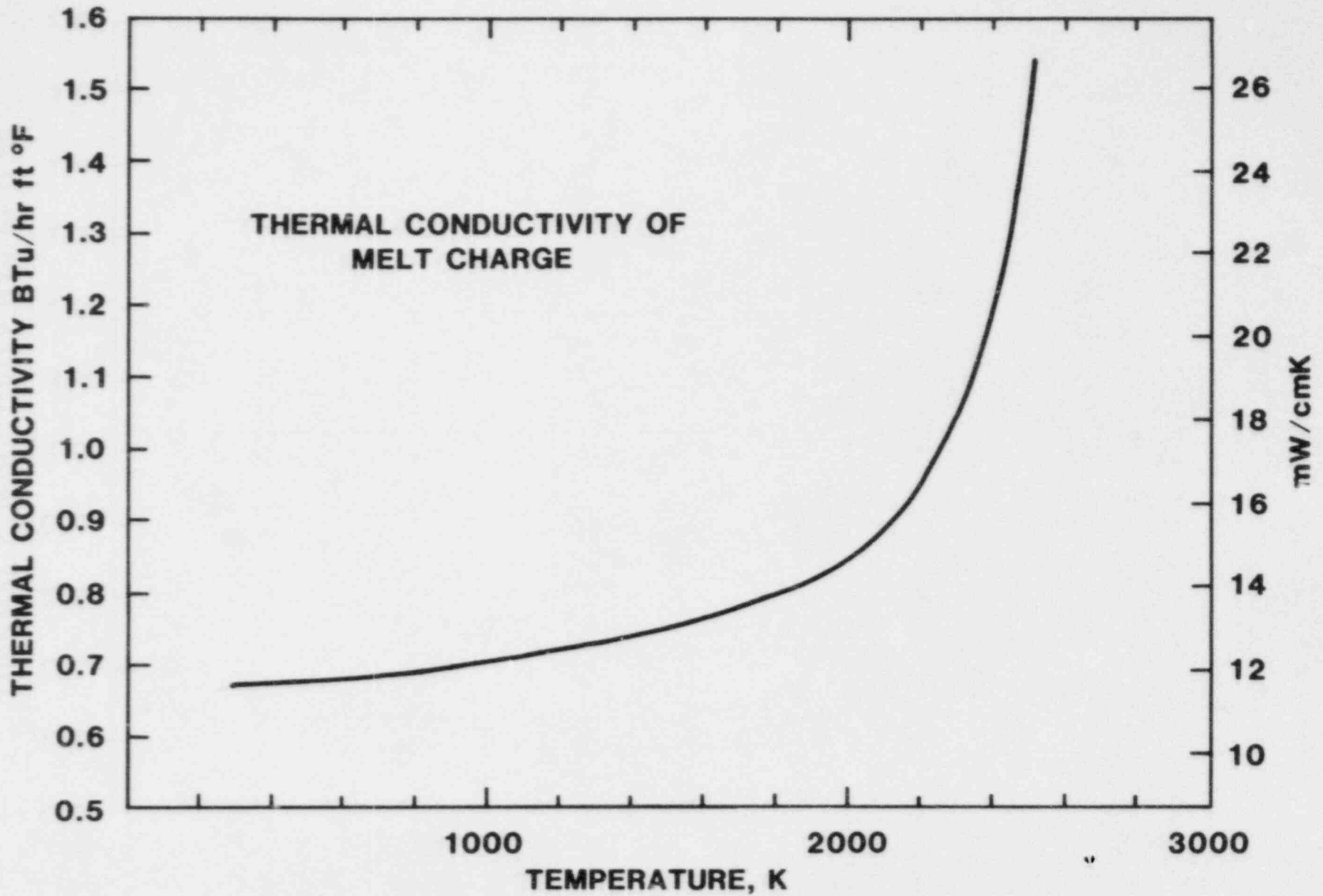
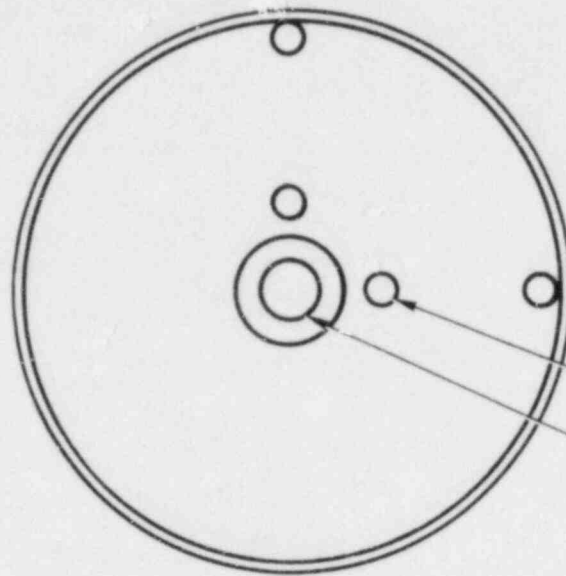


Figure II.6 Thermal Conductivity of the Charge,
"Corrected" Value

CHARGE STACK



0.75 DIAMETER
4 PLCS

1.25 DIAMETER

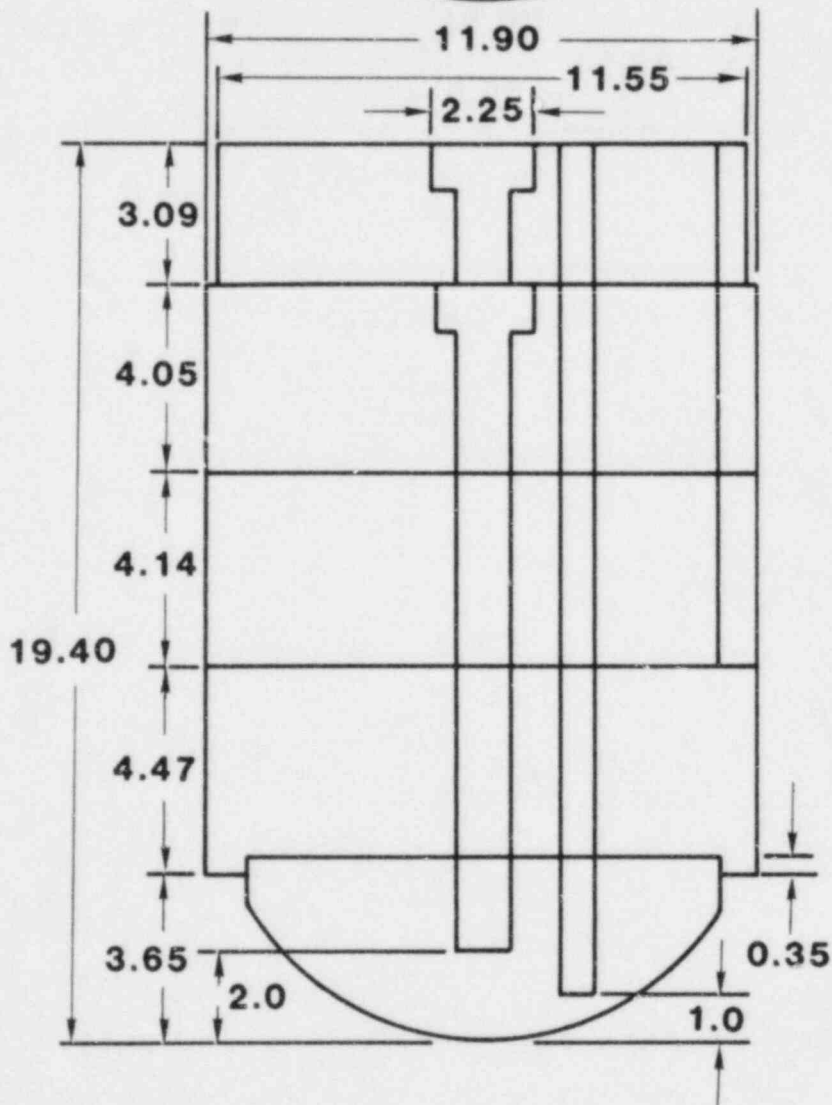


Figure II.7 The Melt Charge Assembly

holes at the 5.5 in. radius all 0.75-in.-diameter to accept ultrasonic thermometers and thermocouples.

A nominally 0.2 in. thick layer of powder was packed between the charge assembly and the melt crucible to provide an even distribution of load. UO_2 instead of UO_2/ZrO_2 mixture was used to pack the charge. The UO_2 powder surrounding the charge was expected to sinter during the test and act as a crucible at least in the initial stages of melting, thus providing an additional barrier against melt/crucible interaction.

c. Crucible for Melting

The crucible assembly consists of a Ta-10W outer crucible with a tungsten plasma spray coating inside and a free-standing tungsten liner, see Figure II.8. Tungsten powder is packed between the liner and the Ta-10W crucible to provide both an even support for the liner and an additional barrier as the tungsten powder sinters at high temperature.

(1) Laboratory Material Studies

Ta-10W was chosen as the material for the outer crucible because of its resistance to carbon diffusion, [7]. Carbon diffusion into Ta-10W is about $\frac{1}{3}$ of that for pure tantalum at 2700°C, at lower temperature the difference is even greater. Tungsten likewise is less resistant to carbon diffusion than Ta-10W. Furthermore, tungsten and carbon form low melting point eutectics.

However, compatibility tests at Sandia [8] showed that Ta-10W is very susceptible to attack by the molten charge. In these tests, tungsten and Ta-10W were exposed to the molten charge at temperature varying from 2873 K to 3013 K (2600°C to 2740°C) for up to 3 hr. In all of the experiments, the attack of the various oxides on the tungsten crucible was minimal. The only evidence of interaction is a surface layer of 50-65 μm in depth which polishes differently from the rest of the crucible wall, see Figure II.9. On the other hand, the attack of the oxide on the Ta-10W was quite severe in all cases. Figure II.10 shows the structures of a Ta-10W strip exposed to the oxide melt and illustrates the general character of the oxide attack on the alloy. The Ta-10W strip is attacked throughout its thickness (1 mm) leaving a skeletal structure of nearly the same dimensions as the original; the white material is the remaining metal and the grey is the oxide. Metallographic examinations and electron beam microprobe analysis of the samples showed the "erosion" mechanism to be the dissolution of Ta in the oxides. Ta is more soluble in the oxide melt than W and is selectively leached from the Ta-10W alloy.

The multi-walled crucible design is a direct consequence of the compatibility studies. The Ta-10W outer crucible is used for structure support and to resist carbon attack from the susceptor. The tungsten barriers (from inside out, the tungsten liner, the tungsten powder and the plasma sprayed tungsten on the inside of the Ta-10W crucible) are used to contain the melt. The maximum operating temperature of the crucible is 2830°C since beyond this temperature the Ta-W-C ternary system has a liquid phase [10].

**TANTALUM
10% TUNGSTEN
CRUCIBLE AND
TUNGSTEN LINER**

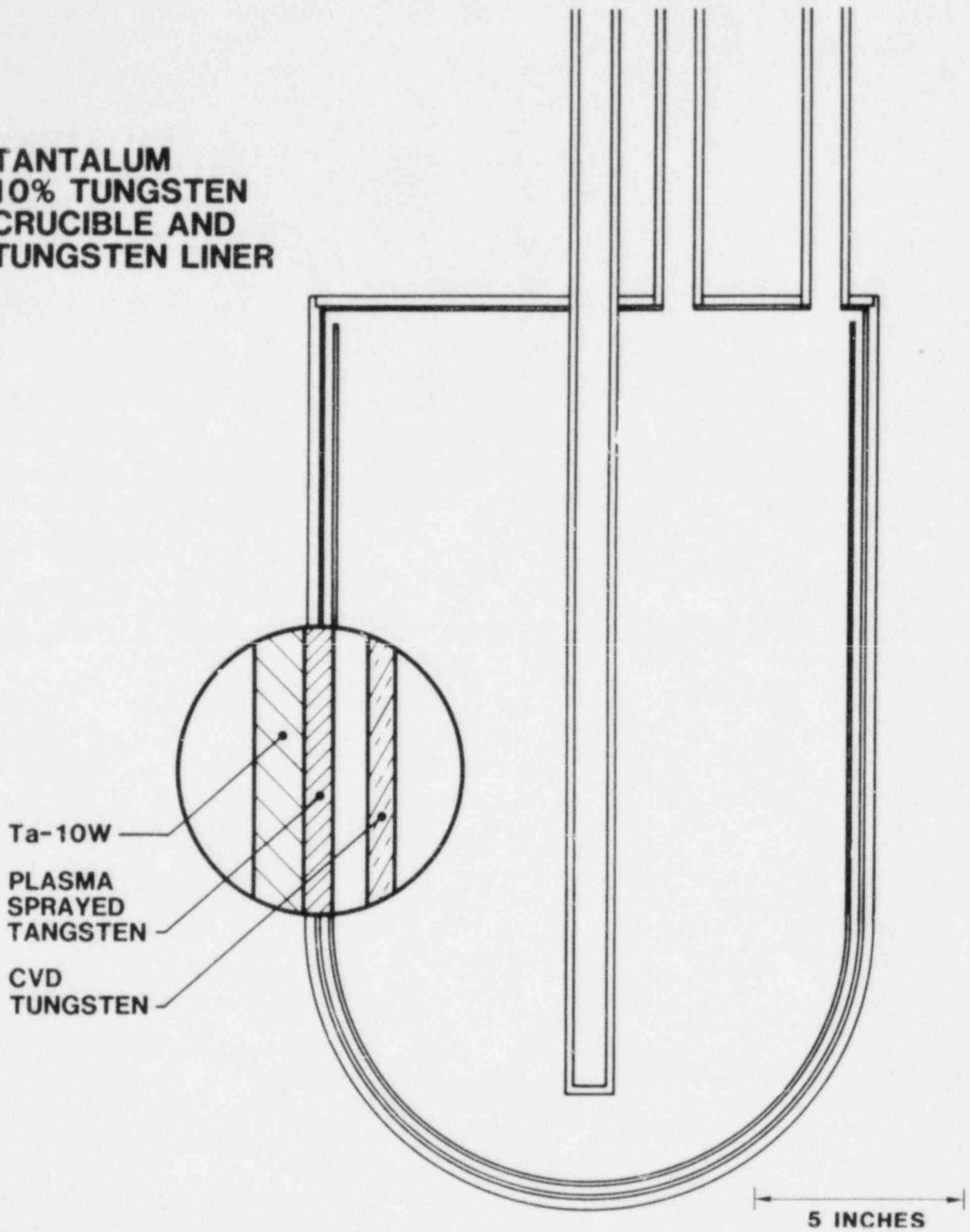
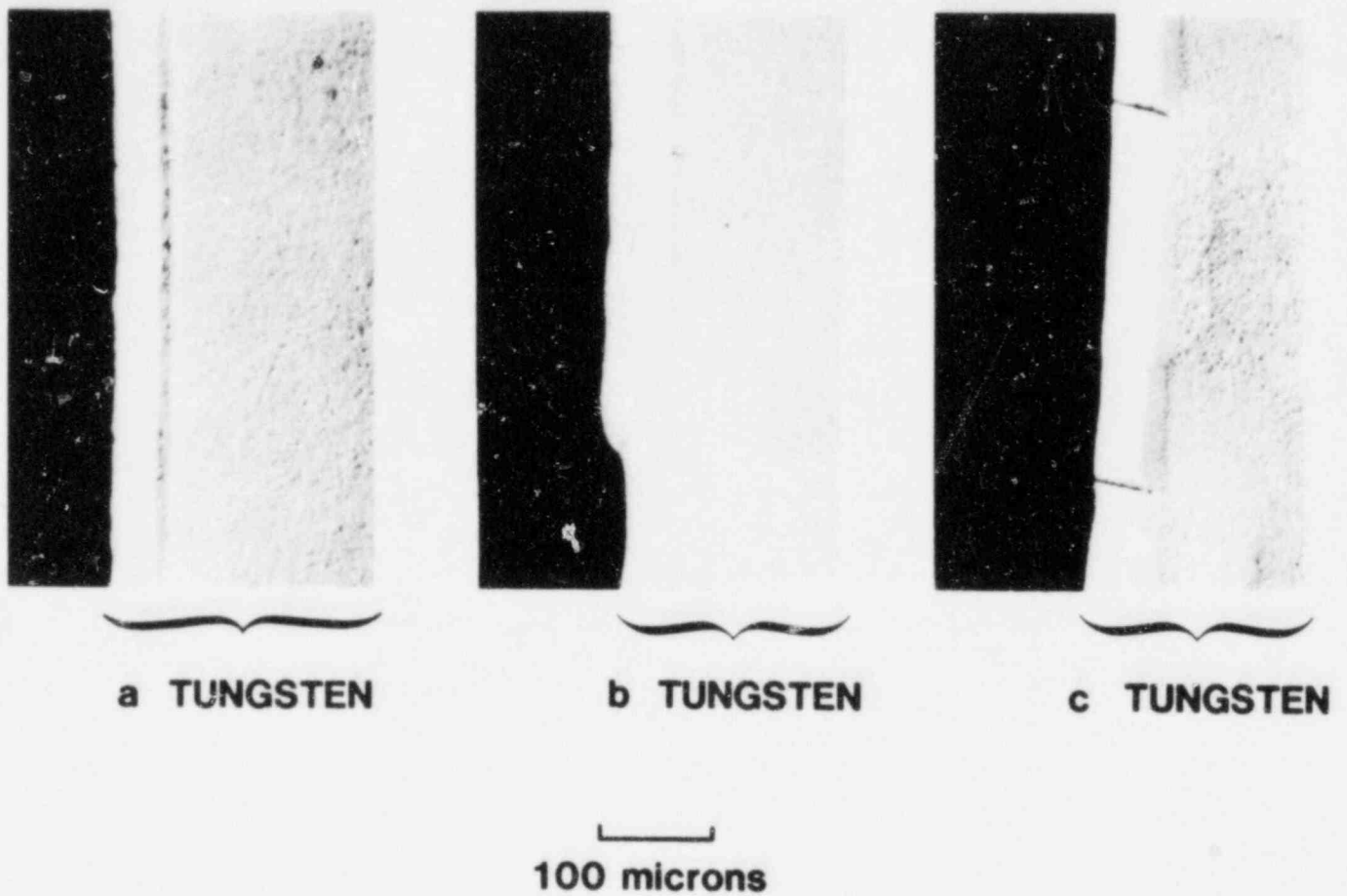


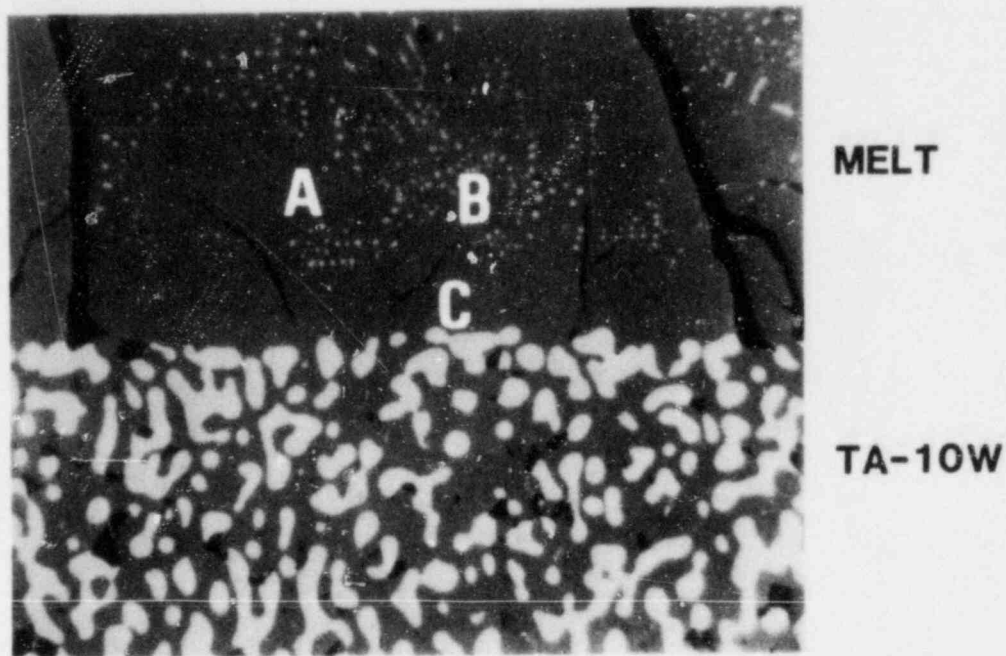
Figure II.8 Schematic of the Multi-Walled Crucible Assembly



**OPTICAL 160X OF METALLOGRAPHIC SECTIONS
SHOWING TUNGSTEN CRUCIBLE WALLS.**

- a. RUN 1, 2740°C, 1 HOUR, $\text{UO}_2 + (\text{ZrO}_2 + \text{Y}_2\text{O}_3)$
- b. RUN 6, 2700°C, 3 HOURS, $\text{UO}_2 + \text{La}_2\text{O}_3$
- c. RUN 5, 2700°C, 3 HOURS, UO_2

Figure II.9 Melt Interaction Zone in Tungsten



OPTICAL 400X MICROGRAPH OF SAMPLE 3B SHOWING PRE-EUTECTIC OXIDE (A), THE TA-OXIDE EUTECTIC (B) AND A TA DEPLETION ZONE CLOSE TO THE SURFACE OF THE METAL STRIP (C).

Figure II.10 Melt Interaction Zone in Ta-10W

(2) Fabrication

(a) Ta-10W Crucible

A schematic of the crucible assembly is shown in Figure II.8. The overall height of the Ta-10W crucible was 21.715 inches. The inside diameter varied from 12.944 in. to 13.030 in. and the wall thickness varied from 0.266 to 0.308 in., Figure II.11. The crucible was formed in three parts. The lid and the upright cylinder were both made from sheet stock of the material. The bottom hemispherical section was formed by cold drawing through a ring die with annealing between drawings because of work hardening of the material. Following the drawing operations, the bottom was machined to the exact shape desired. The lid was basically a flat disk with instrumentation pass-throughs welded on it. The body of the crucible was formed by first closing the upright cylinder with a vertical weld then joining the cylinder and the hemisphere with a girth weld. All the welds were electron beam welds.

A plasma-sprayed layer of tungsten of nominal dimension of 0.120 in. was applied to the inside of the crucible. Analysis at Sandia showed that the oxygen content of the spray was 2000 ppm.

(b) Tungsten Liner

The liner was made by chemical vapor deposition (CVD) of tungsten onto a male molybdenum mandrel. The mandrel was fabricated to the shape of the liner inside configuration. The cylindrical portion of the mandrel was rolled from sheet stock and the bottom hemisphere was deep drawn and machined into final shape. All the joints were riveted butt joints. A schematic of the mandrel is shown in Figure II.12. There were six lines of rivets and three joints, two vertical and one girth.

The liner was formed by deposition of tungsten through decomposition of WF_6 onto the heated (1123 K, 900°C) molybdenum mandrel. Deposition occurred in a quartz vacuum furnace jar approximately six inches larger (linear dimensions) than the liner and similar in shape, Figure II.13. WF_6 was introduced into the quartz jar through several equally spaced nozzles perpendicular to the liner surface. The liner was inductively heated and rotated in a vacuum during the deposition process. Tungsten buildup was inspected every 0.020 in. of thickness so that abnormal nodular growths could be ground flush before proceeding. After the required thickness was achieved, the tungsten was cut to length by grinding and the mandrel was etched away using nitric acid.

The liner had a matted surface finish. It was slightly out of round. The inside diameter varied from 12.68 to 12.74 in. and the inside depth was 20.503 in. The wall thickness was 0.065 in. on the side and 0.089 in. at the tip of the hemisphere. Corresponding to the butt joint locations on the mandrel, the liner had two vertical ridges and one girth ridge in the inside surface. The ridges had typical dimensions of 5-10 mils or less.

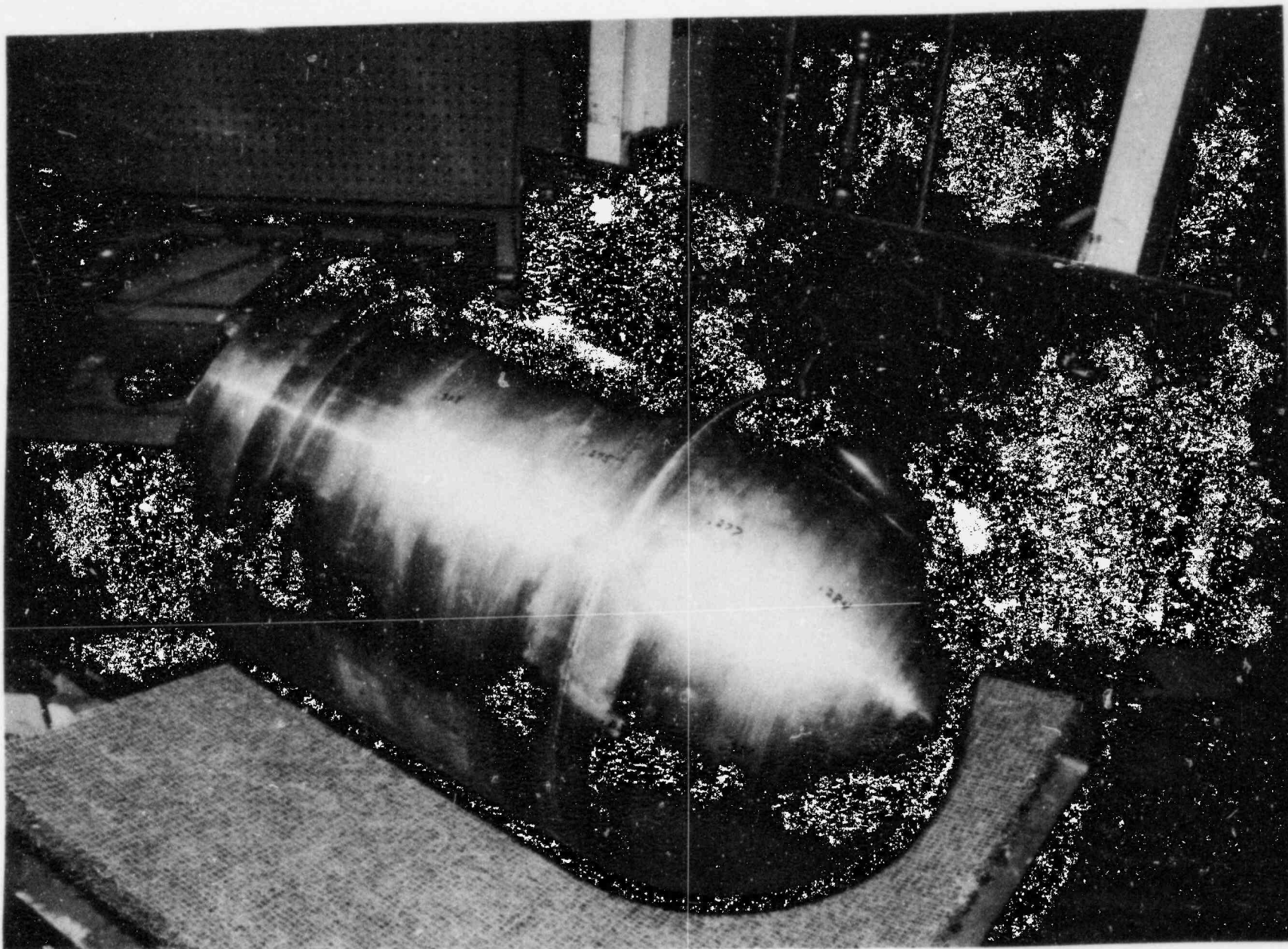


Figure II.11 Photograph of Ta-10W Crucible with Thickness Measurement Marked

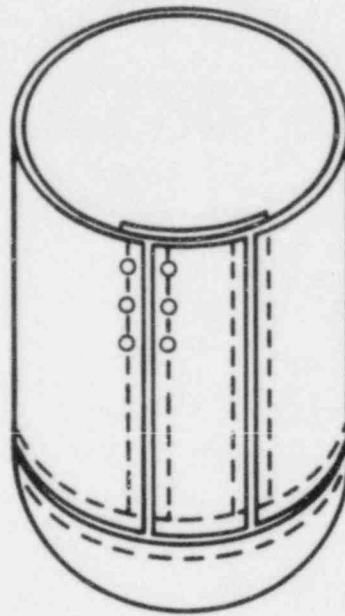


Figure II.12 Schematic of CVD Liner Mandrel

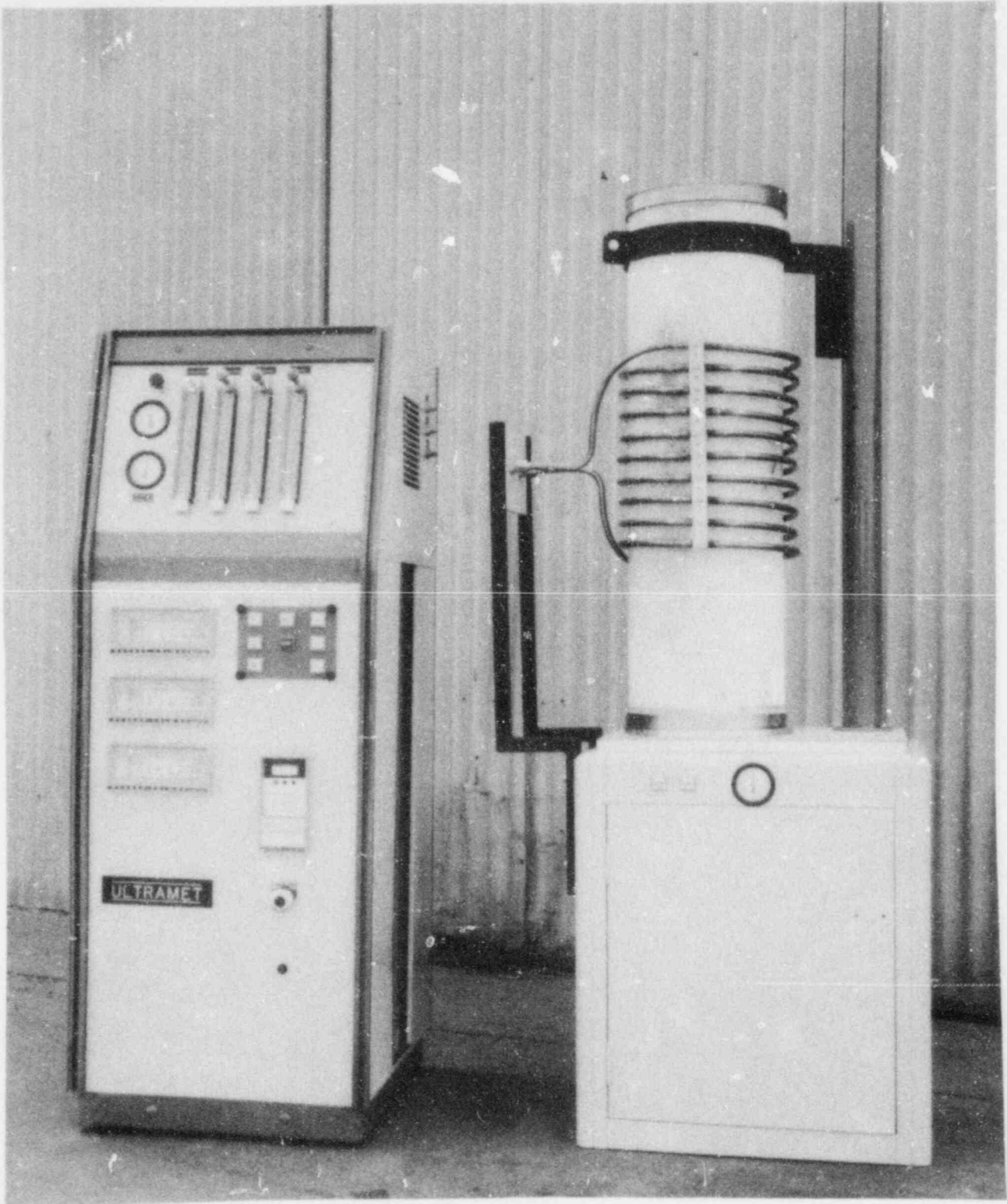


Figure II.13 A Typical CVD Processing Furnace

The liner was flawed. There were a number of (~10) small cracks at the top rim typically no longer than 60 mils and a long crack at one of the vertical ridges extending approximately 10 in. from the top with the first 4-6 in. cracked through.

3) Loading

A schematic of the overall assembly of the charge in the crucible is shown in Figure II.14. The space between the liner and the Ta-10W crucible was packed with tungsten powder and the space between the charge pieces and the liner was packed with UO₂ powder. In both cases, powder packing was used to achieve an even distribution of load.

The procedure for loading the liner into the crucible assembly was as follows:

1. Fill the bottom of the Ta-10W crucible with a thin layer of tungsten powder,
2. Lower the liner into the Ta-10W crucible,
3. Vibrate tungsten powder into the gap between the liner and the crucible. The liner is centered in the crucible by the use of several nylon strip spacers in the side gap. Because the liner floats in the tungsten powder, the bottom gap is maintained simply by holding the liner down at a specific location from the top.

With the multi-walled crucible assembled, the charge pieces were loaded. The procedure for loading the charge pieces was similar to the one for the liner:

1. Fill the bottom of the liner with a layer of UO₂,
2. Lower the hemispherical piece into the liner to the desired position,
3. While the hemispherical piece is held in position UO₂ powder is vibrated into the gap around it.
4. Other pieces are loaded from the top sequentially one by one and powder packing vibrated around it.

To carry out the above procedure, a special loading fixture, Figure II.15, and several vacuum chucks for holding the loads, Figure II.16, were built. During loading the fixture was placed on a vibrating table. The fixture consisted of a heavy base with two vertical shafts on the side. A horizontal loading bar with roller bearings fitting the shafts was used to carry the vacuum chucks and lower them into the crucible with precision. Fastened to the base was a brass block with a machined cavity fitting the bottom outside contour of the crucible; the cavity together with four locating bars secured the crucible on the base of the loading fixture. Adjusting screws were used to align the crucible with the vertical travel of the loading bar. During assembly, the loading bar with the load secured by vacuum chuck, was lowered until the load reached the desired position into the crucible. The loading bar was then locked in place by two stopper rings on the shaft. The vacuum chuck continued to hold the load in position until powder packing was accomplished.

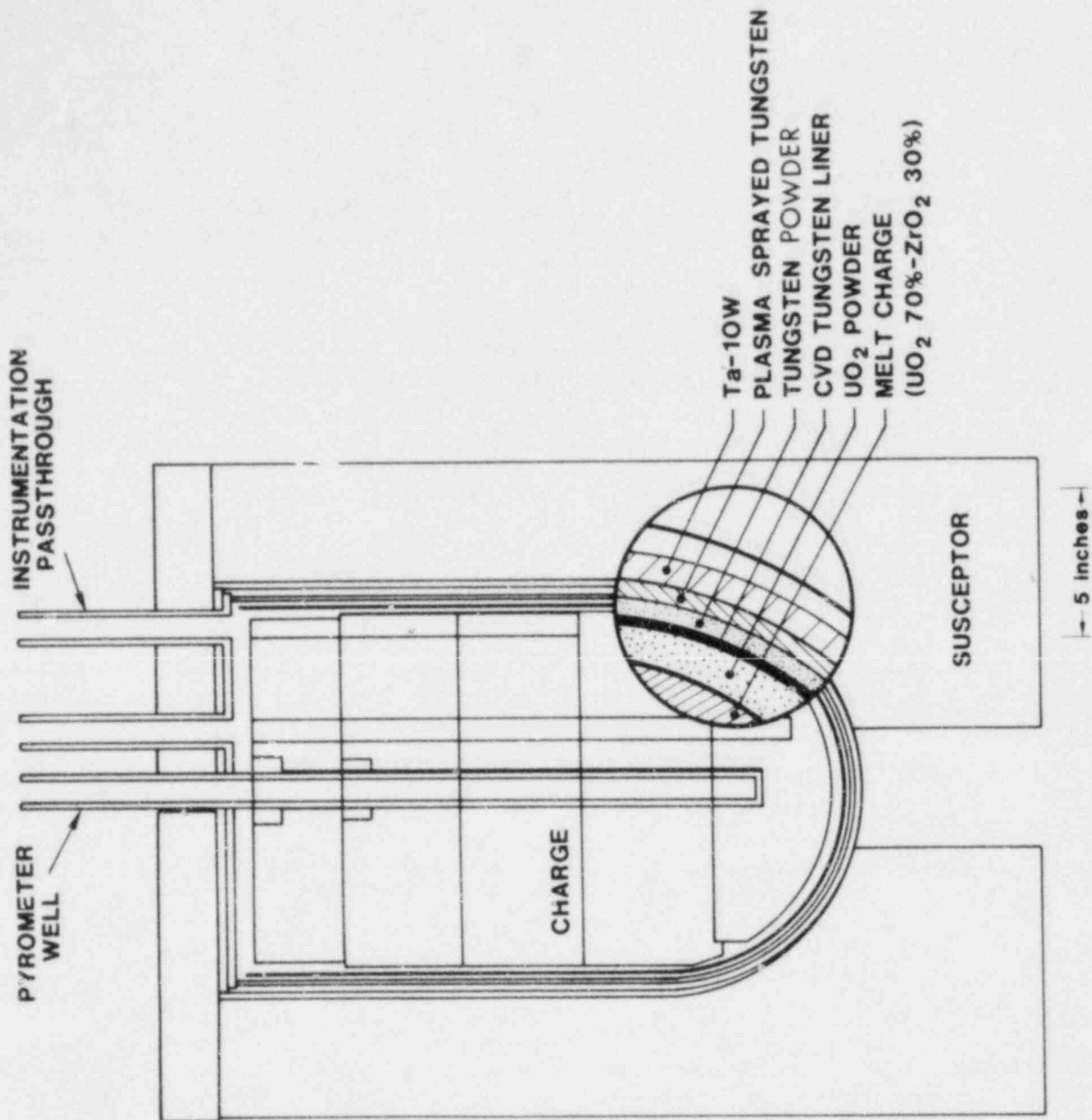
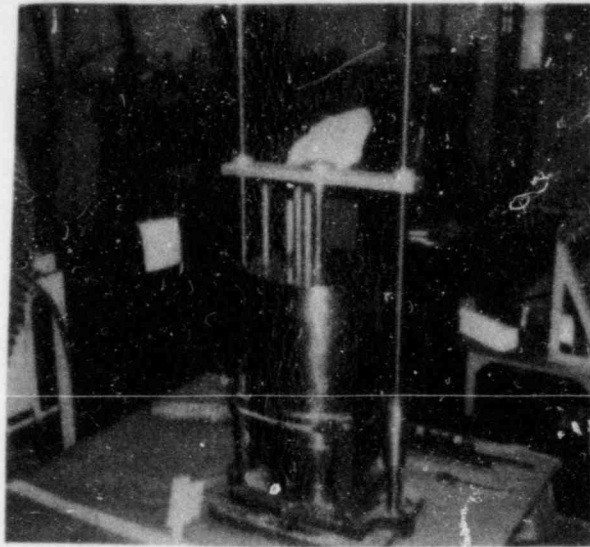


Figure II.1.1' Charge/Crucible/Susceptor Assembly

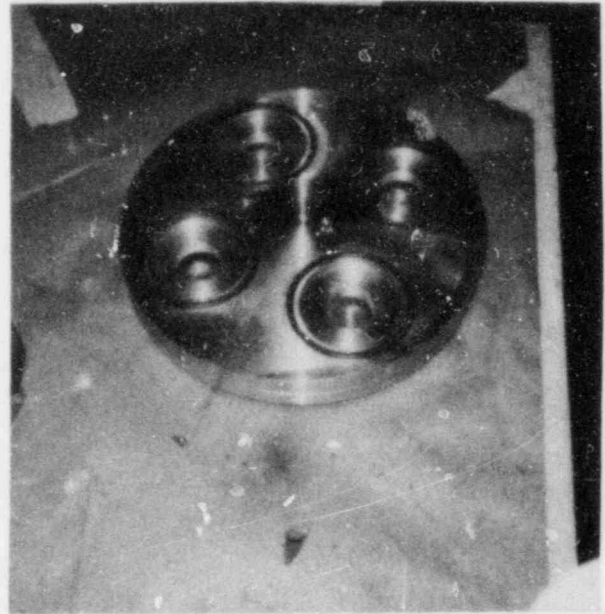


Crucible with top on being aligned with center of loading bar. The center of the bar has to match the center pyrometer tube on the lid.

Figure II.15 Crucible and Charge Loading Fixture



Liner being lifted out
of the shipping box
using vacuum chuck



Vacuum chuck for lifting
charge pieces

Figure II.16 Vacuum chucks for holding the charge and liner

The vacuum chucks for loading the charge pieces had interchangeable alignment pins fitting the instrumentation holes in the charge to keep all the charge pieces aligned during loading. When all the charge pieces were loaded, a set of alignment rods placed in the instrumentation holes in the charge were used to keep all the pieces aligned while the entire assembly was being vibrated. The alignment rods were also used during subsequent transportation of the loaded crucible. As mentioned before, holes in the charge were 1 1/4 and 3/4 in. in diameter; corresponding alignment rods were 1 1/8 and 11/16 in. diameter. When all the pieces were loaded the crucible lid was installed and electron beam-welded in place.

d. Magnesia Brick Crucible

The magnesia crucible was made of Harklase MgO bricks. The bottom was made of three layers of 9 x 4 1/2 x 2 1/2 in. flats with a total thickness of 7 1/2 in. The long dimensions of the bricks were 90° apart in each layer. The bricks were off-set in each layer such that no crack extended beyond one layer. The sidewalls were made of two layers of arch bricks with a total thickness of 9 in. The inner sidewall of the cavity was two bricks high and each stack was made of four #4 arches (13 1/3 x 4 1/2 x 3-1 in.) and 20 #3 arches (13 1/2 x 4 1/2 x 3-2 in.) The resulting cavity was approximately circular with a maximum "diameter" of 14 1/2 in., a minimum "diameter" of 14 in. and a depth of 26 in. deep, Figure II.17a. With this cavity the maximum melt level was expected to be 11.2 in. The inner edges of the top cavity bricks were bevelled, Figure II.17b, to redirect the flow of a misdirected melt stream.

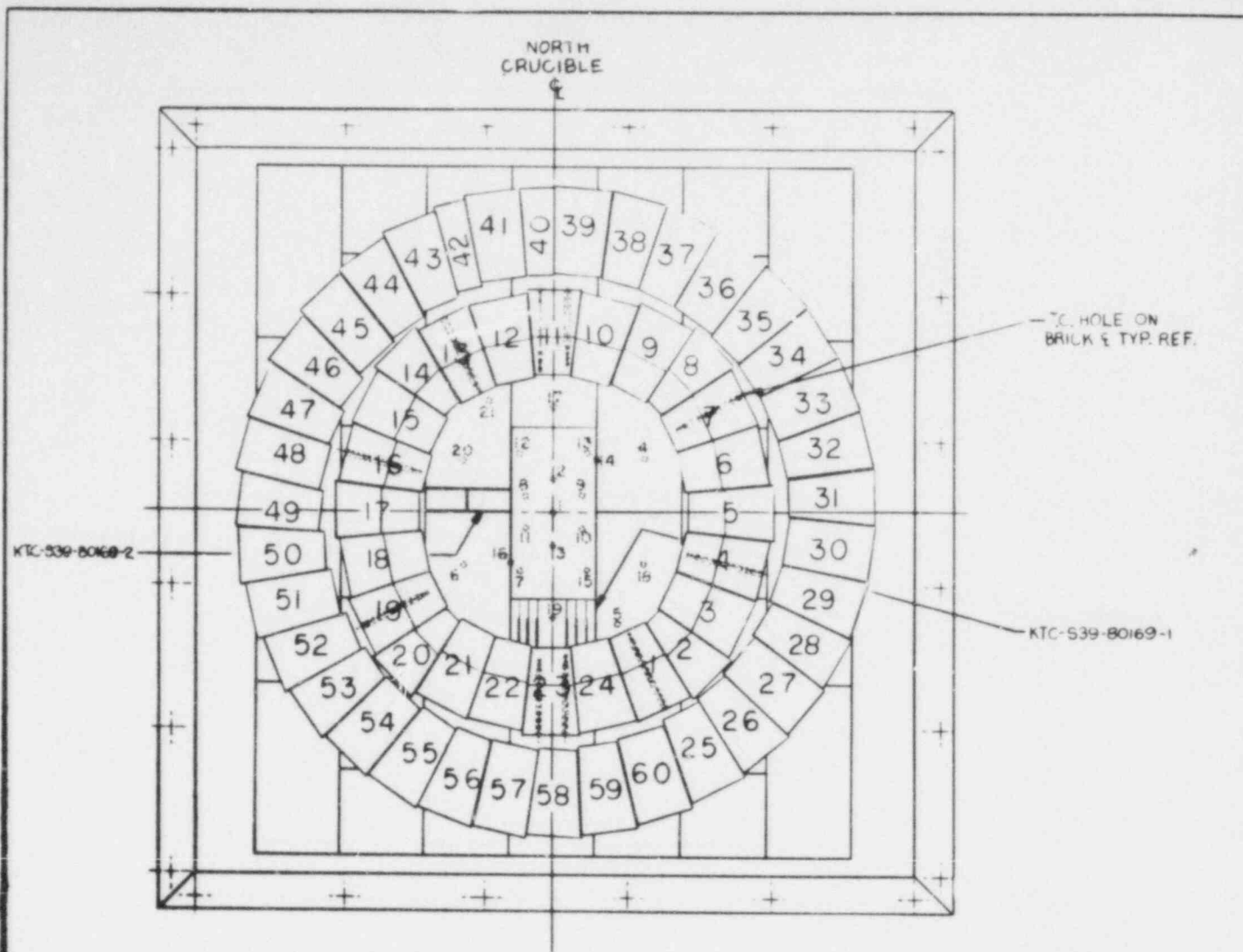
The bricks were supported below by a 3/4 in. steel plate. The entire brick assembly was contained inside of a 42 in. x 42 in. square steel box 37.5 in. high. The space between the brick assembly and the box was filled with MgO powder.

e. Instrumentation

1) In Furnace

(a) Thermocouples

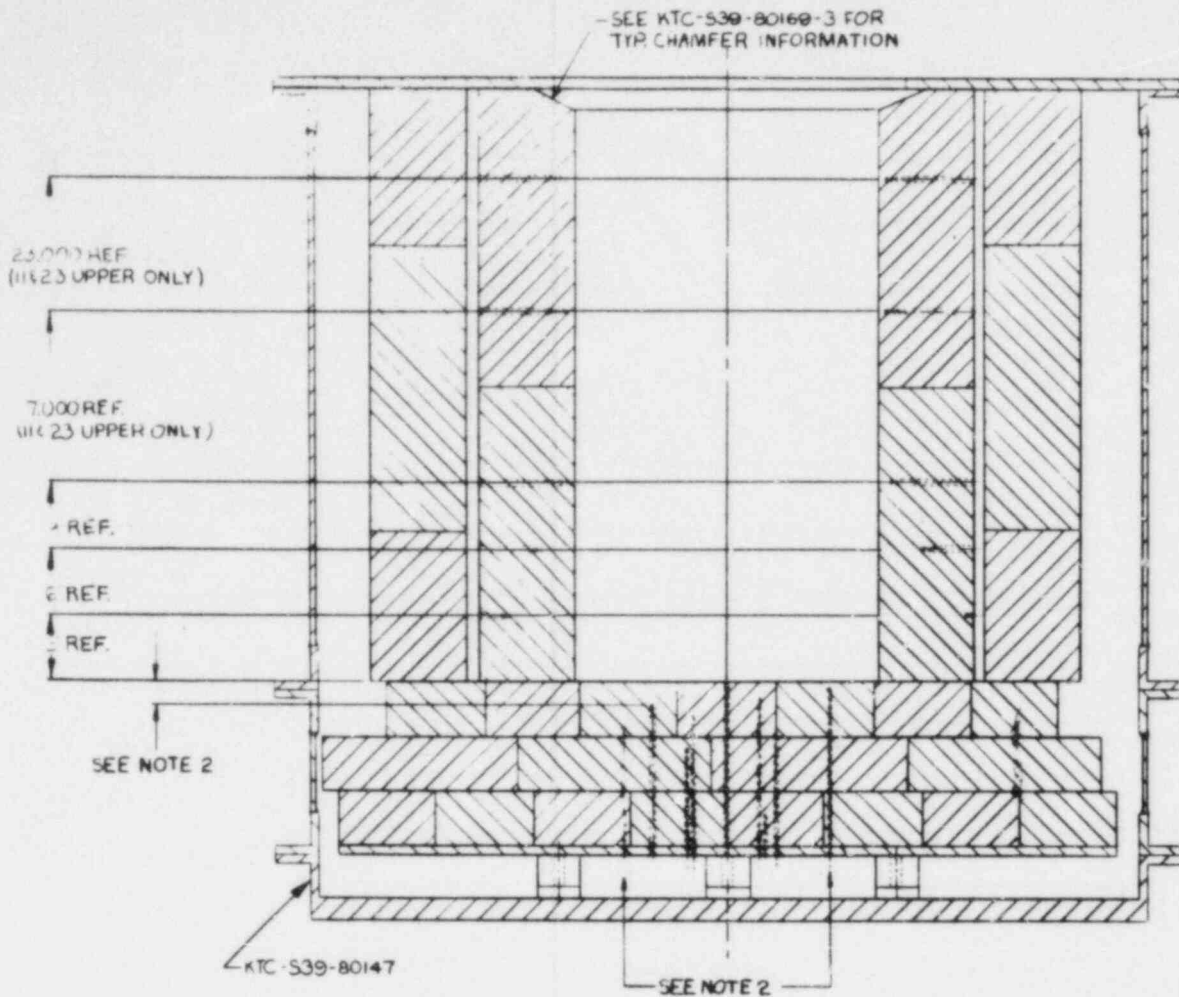
In all, twenty-one W-5 thermocouples (Tungsten 5%-Rhenium vs Tungsten 26%-Rhenium) were installed in the furnace. They were 1/16 in. diameter, tantalum sheath thermocouples with Beryllia insulation. There were eight in the graphite susceptor and thirteen in the charge. Figure II.18 shows, graphically, the thermocouple locations. Of the eight in the susceptor, three pairs were in the walls of the susceptor and one pair was in the bottom next to the tapping hole in the graphite under the crucible. Thermocouples in the susceptor were installed radially and protected by two concentric closed-ended tantalum tubes (3/16 O.D. inside of 1/4 O.D.) with a total wall thickness of 35 mils. The thermocouples in the charge were protected by tungsten wells, 0.53 to 0.54-in. I.D. with 30-40 mil thick wall. They were installed at the 2 in. radius and 5.5 in. radius at depth from 3 in. to 15 in. below the crucible lid. There were also two thermocouples in the



THERMOCOUPLE NUMBER	BRICK NUMBER	SURFACE DEPTH	HEIGHT	THERMOCOUPLE TYPE	COMMENT
1		1/8"		W-5	SEE NOTE 2
2		1/4"		W-5	
3		1/2"		W-5	
4		1/4"		W-5	
5		1/8"		W-5	
6		1/2"		W-5	
7		1/8"		W-5	
8		1 1/2"		K	
9		3/4"		K	
10		2"		K	
11		1"		K	
12		3"		K	
13		6"		K	SEE NOTE 2
14		2 1/2"		K	TC BETWEEN BRICKS
15		4"		K	SEE NOTE 2
16		1"		K	TC BETWEEN BRICKS
17		3/4"		K	SEE NOTE 2
18		1 1/2"		K	
19		1"		K	
20		2"		K	
21		1"		K	SEE NOTE 2
	1	2 1/2"	3"	K	SEE NOTE 4
	1	1"	6"	K	
	1	1 1/8"	9"	W-5	
	4	3"	3"	K	
	4	1 1/2"	6"	K	
	4	1 1/4"	9"	W-5	
	7	4"	3"	K	
	7	2"	6"	K	
	7	1/2"	9"	W-5	SEE NOTE 4

BRICK NUMBER	SURFACE DEPTH	HEIGHT	THERMO TY
13	2 1/2"	3"	K
13	1"	6"	K
13	1 1/8"	9"	W-
16	3"	3"	K
16	1 1/2"	6"	K
16	1 1/4"	9"	W-
19	4"	3"	K
19	2"	6"	K
19	1/2"	9"	W-
11 U			K
23 U			K

Figure II.17a MgO Crucible Cavity Brick Pattern



- NOTES: 1. SURFACE DEPTH ON CRUCIBLE WALL IS THE DISTANCE FROM WHERE THE T.C. HOLE ENDS TO THE CAVITY.
 2. LOCATE POSITION OF T.C. HOLES 1 TO 21 FROM DR. NO. KTC-539-80148, & DEPTH FROM CHART.
 3. SEE DR. NO. KTC-539-80169-3 FOR DETAILS.
 4. SEE DR. NO. KTC-539-80169-4 FOR DETAILS.

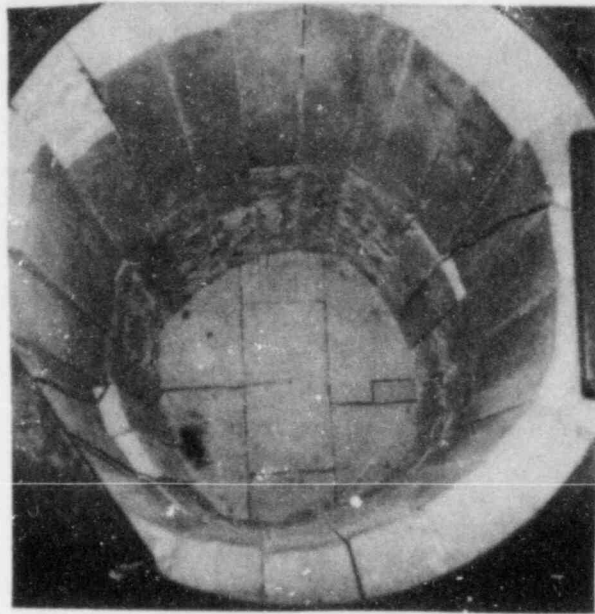
DUPLICATE	COMMENT
	SEE NOTE 4
	SEE NOTE 4
	SEE NOTE 3
	SEE NOTE 3

8411290150-01

29-30

TI
 APERTURE
 CARD

KTECH CORPORATION			
901 PENNSYLVANIA AVE N.E. ALBUQUERQUE, NEW MEXICO 87110			
PROJECT	S33-C	TITLE	T.C. INFO. BRICK CON-
CONTRACT NO.			TAINMENT CAN. HIGH
PROJECT ENGINEER	DATE		TEMP MELT FACILITY
KTECH ENGINEER	W. W. TARBELL		
BY	JOE RICE	6/17/80	
DRAWN			
MATERIAL		DWG NO.	D KTC-533-80168
SCALE	1/4	SHEET	29



↓
S

Figure II.17b MgO Crucible Cavity

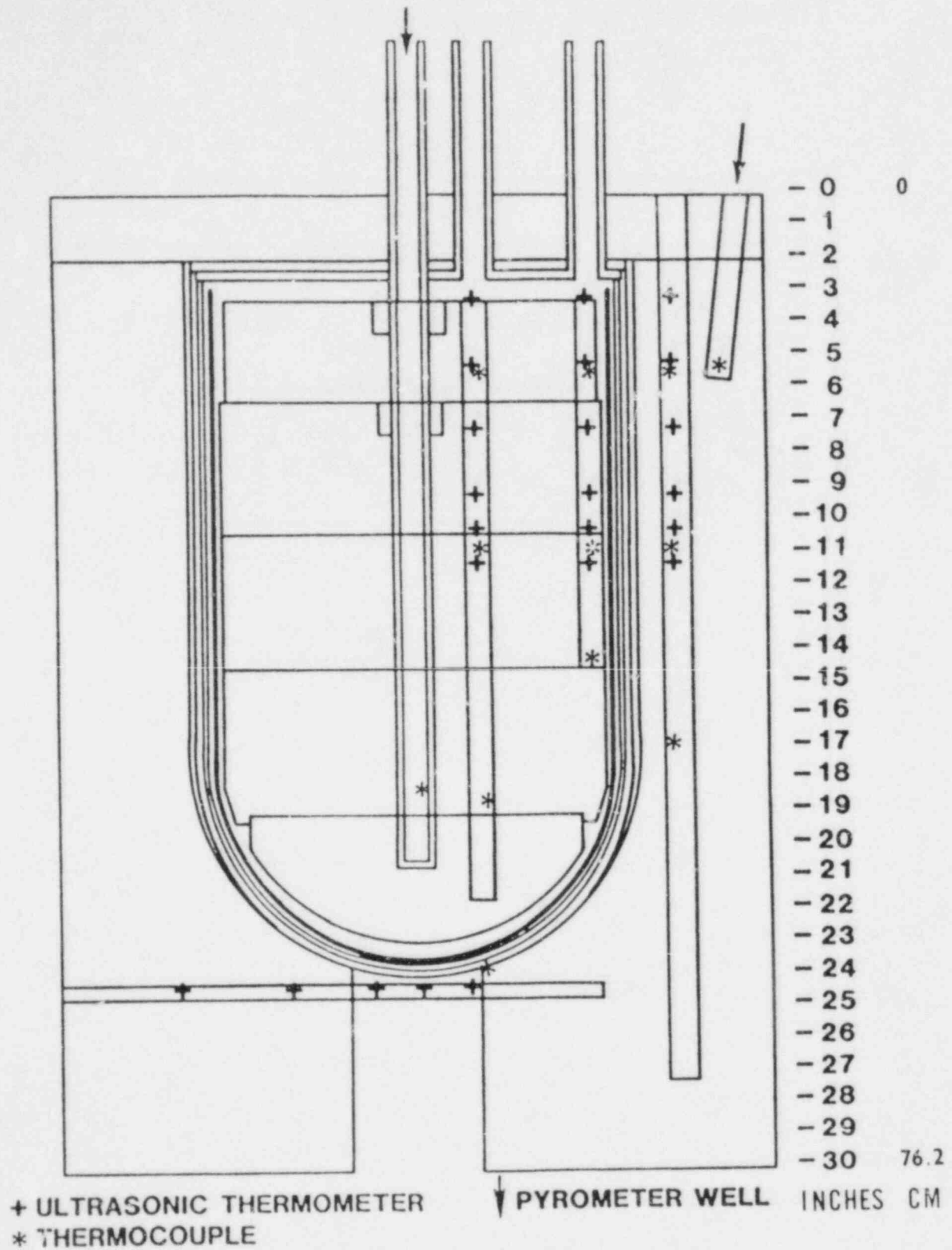


Figure II.18 Schematic of Instrumentation Placement in the Charge and the Susceptor

center pyrometer well in the charge, 16 in. below the lid of the crucible.

(b) Pyrometers

Two pyrometers were used in this experiment; One to monitor the susceptor temperature and one to measure the charge temperature. The susceptor pyrometer was a Pyro Automatic Pyrometer; sighted into a graphite tube of 9/16 in. I.D., 5.5 in. into the susceptor from the top at an angle of 6° off vertical with the bottom of the tube 1.5 in. from the outer surface of the susceptor wall, Figure II.18. Two W-5 thermocouples at the same radius as the bottom of the tube and about 0.5 in. away were used to compare with readings from the pyrometer. The charge pyrometer was an Ircan Modline 2000 pyrometer. It looked into a well in the center of the charge. The well was made of 0.89-in. I.D. 1.06-in. O.D. Ta-10W tube, it extended 17.9 in. below the crucible lid to within 2.9 in. of the bottom of the charge. In addition, the well had a CVD tungsten outer sheath with 1.15-in. I.D., 55-mil thick wall. The sheath was attached to the well by two tungsten pins near the lid. Two W-5 thermocouples in a 0.25 in. tube along the inside wall of the well were used to compare with the readings of the center pyrometer. The tip of the thermocouples reached within 2.5 in. of the bottom of the well.

(c) Ultrasonic Thermometers

The ultrasonic thermometer (UT) instrumentation for this experiment consisted of one horizontally placed sensor in the graphite susceptor and five vertically placed sensors, two in the melt charge and three in the graphite susceptor, Figure II.18. All sensors were made of 20-mil-diameter thoriated tungsten rod and placed in 1/8-in.-diameter tantalum sheaths with continuous thoria spacers. The available thoria dictated that the continuous spacers be made up of several pieces, the longest of which was about eight inches. In addition, the thoria was obtained from three different manufacturing batches. This was certainly not desirable, but the thoria quality severely limited the choices. Each tantalum sheath was placed in a thick walled Ta-10W protection tube 0.25-in. I.D. and 0.50-in. O.D. The sensors located in the melt charge had an additional tungsten protection tube (same as those used for thermocouples) to prevent chemical attack of the Ta-10W.

The horizontal UT had five measurement zones. This sensor was arranged to give two symmetric zones about a central zone which was offset about 2.75 in. from the susceptor cylinder axis. These three zones were 1.5 in. long. This sensor was placed near the bottom of the susceptor next to the passage through which the melted charge would pass, see Figure II.18. In addition, a zone of length 2.5 in. was centered at a radius of eight inches, corresponding to the radius at which the vertical sensors were placed.

The five vertical UTs were identical and of similar construction to the horizontal UT. Three sensors were placed at a radius of eight inches in the graphite susceptor at different angular locations to

provide redundant data. Two sensors were placed in the melt charge at radii of 2 in. and 5.5 in. respectively.

Each vertical UT had six measurement zones, Figure II.18. The sensor wires extended approximately 12 in. into the furnace hot zone, charge, or susceptor, as appropriate. The length of the UT was limited by the signal attenuation at the highest temperatures. The UT's were less than half the axial length of the susceptor in the present test. One measurement zone was designed to correspond to the bottom of the side pyrometer tube, Figure II.18, 5 in. deep. As many zones as possible of length 1.25 in. were placed near the end of the sensor.

Each vertical UT had two thermocouples placed at the corresponding radius at depths of 5 in. and 11 in. as indicated in Figure II.18. This allowed two points for comparison at temperatures up to about 2673 K (2400°C). Since the thermal mass of the UT assembly was so large, because of the heavy protection tubes, the thermal response could be different than the thermocouples.

(2) In Chamber

(a) Gas Samples

Gas samples taken during the test will provide information on the possible chemical interactions between the melt charge and magnesia. Furthermore, gas composition is required to calculate particle impaction criteria for aerosol samplers.

Two sampling lines were placed adjacent to the crucible cavity for maximum gas resolution and identification. The lines were connected outside the test chamber to a "tee fixture" for sampling into a remotely switched array of gas bottles. A pressure transducer was placed in the valve-switching system and served the two-fold purpose of:

1. measurement of the pressure near the cavity during interaction and;
2. sample duration of the gas samples.

(b) Aerosol Samplers

A key phenomenon associated with high-temperature melt interactions is the generation of aerosols. In this experiment the melt interaction was contained in the test chamber. Aerosol production adds mass to the chamber volume. Mass is removed from the chamber volume by venting and by deposition on the interior surfaces. Based on mass balance considerations the mass source term, S , can be written as:

$$S = V \, dC/dT + (Q + \sum_1 k_i A_i) C \quad (\text{II.1})$$

where

- S = Mass Source Term (g/s)
- C = Mass Concentration (g/m³)
- t = Time (s)
- V = Chamber Volume (m³)
- Q = Vent Gas Flow Rate (m³/s)
- k_i = ith Deposition Coefficient (m/s)
- A_i = Area of ith Deposition Surface (m²).

The summation is over all surfaces that have aerosol deposition. The instrumentation for measuring aerosols is listed below together with the quantities from Equation (II.1) that are measured or calculated.

- Filter Samples C, dC/dt
- Cascade Impactors size dist., k_i
- Cascade Cyclone samples for analysis
- Coupons k_i
- Vent Flowmeter Q
- Gas Samples gas composition and properties

Other measurements such as gas evolution rates and gas composition are used in data evaluation. Elemental analysis of the cyclone sample is used to determine size-dependent aerosol composition.

(i) Filter Samplers

The filter samples are the most important data taken. They are used to determine concentration and time rate of change of concentration. For small losses (by venting and deposition), the filter samples (along with gas composition so that flows are known) give the source term. Average concentration over a sampling interval is simply the ratio of the mass collected and the volume of gas flowing through the filter.

Millipore filter holders were used. They contain a single filter (teflon, type-5 μm) which yields mass concentration data. Each filter was dried in a desiccator for approximately two days before weighing.

Six type-275 psi Millipore filter holders were installed on the outside wall of the chamber. They were heated to 373 K (100°C) with a heating tube and the temperature controlled by Omega 920 temperature controllers to prevent vapor condensation.

Three vacuum type Millipore filter holders were installed on the inside wall of the chamber. The filters were located in anticipation of possible overpressurization of the chamber. These filter samples were not heated.

(ii) Cascade Impactors

The cascade impactors give a mass distribution with respect to aerodynamic diameter. This size distribution is used in calculating the gravitational deposition coefficient for settling. Particle settling is expected to account for at least 80 to 90 % of the deposition. Diffusional deposition for spheres of 1 μm unit density is less than one percent of gravitational deposition for the same spheres in the test chamber. Because the size distribution is time dependent, the integral settling rates also change over time. Four impactor samples are taken during the test.

Four Anderson MKIII Cascade Impactors were used sequentially to obtain mass concentration and particle size information as a function of time during the test. The impactor contains eight stages and a backup filter. On each stage a glass fiber type filter was installed. The filters were dried and weighed similarly to the Millipore filters. These samplers were installed on the outside wall of the test chamber. They were heated to 373 K (100°C) and controlled like the filter samplers.

(iii) Cascade Cyclone

A Sierra Cyclade cyclone installed on the inside of the test chamber operating through the duration of the test, was used to collect material for chemical analysis. The cascade cyclone gives an aerosol mass distribution as a function of aerodynamic particle diameter as does the cascade impactor but it is capable of collecting greater amounts of material than the impactor without overloading. Any distribution information from the cyclone will be skewed by size dependent particle deposition in the chamber during its long sample time. However, composition in each size class is not expected to change over the test period. The long sampling time allows enough material to be collected in each size class to be analyzed to give a size dependent elemental composition.

Critical orifices were used to regulate gas flow in all the aforementioned devices. All Millipore filters were sampled through the same nominally five liters per minute (LPM) orifice. Each impactor and the cyclone had its own nominally 14 LPM orifice. The orifices were calibrated in air at Sandia's calibration standards lab division. Since there was a difference in gas composition a correction in flow conditions was required and could be derived from the gas composition data.

(iv) Deposition Surfaces and Time Resolved Deposition Sampler

Coupon deposition surfaces on the walls, ceiling, and floors

provide an indication of the total aerosol deposition. They provide a method to calculate the average deposition coefficients for all the surfaces and total mass released. Two coupons are located on the ceiling, three on the walls, four on the floor, and four on the top of the MgO crucible. The collected materials are weighed and a surface loading calculated. The surface loading is used to estimate the total mass of material deposited on the interior surfaces of the chamber and thus the total mass aerosolized.

The deposition surfaces on the walls and ceiling are glass slides (25 mm x 75 mm) held in place by retaining clips. The deposition surfaces on the floor are weigh dishes (100 mm ϕ x 10 mm).

Time resolved deposition rates were obtained by a rotary deposition sampler. Coupons were attached to a turntable which exposes each one sequentially to gravitational deposition. Average deposition rates over each sample time for all of the samples gave an indication of how deposition changes with time. This sampler was located on the floor of the chamber and can take five sequential samples.

(v) An aerosol photometer was included in the instrumentation. It measured the extinction of light across a stream of flowing aerosol. The photometer was calibrated in-situ by correlation of the photometer output with filter samples. The calibrated photometer data was expected to provide a continuous measure of aerosol mass concentration.

Figure II.19 shows the sampler locations in the test chamber. Figure II.20 is a schematic of the samplers and plumbing.

Mixing of the aerosol in the chamber was necessary to ensure that samples were reflective of conditions inside the chamber. It also ensured that the assumption of stirred settling was valid. Three fans were used for mixing and move three times the chamber volume per minute. A minimum sampling time of 30 s was adequate to obtain accurate measurements reflecting the chamber conditions.

c) Upward Heat Flux

A shield of 32 in. diameter located 7 in. above the top edge of the cavity was instrumented to measure the upward heat flux from the melt pool in the magnesia crucible. The shield was a sandwich structure with top and bottom made of 1/4 steel plates and the middle stuffed with alumina felt insulation. The lower plate was actually made of three parts; a 14-in. O.D. disk surrounded by a 14 1/8-in. I.D., 22-in. O.D. ring and an outer ring of 22 1/8-in. I.D. and 32-in. O.D. The 14-in. center shield was plasma-sprayed with a layer of alumina for high temperature protection. Each part was instrumented with two or three pairs of thermocouples. Of each pair of thermocouples, one was at 1/8 in. from the pool facing surface and one on the back surface. Cutting the lower part into three sections reduced the conduction between them and made data reduction more convenient.

Two heat flux gauges were installed through the 14 in. disk. One at the center, one 4 1/2 in. from the center to monitor the local

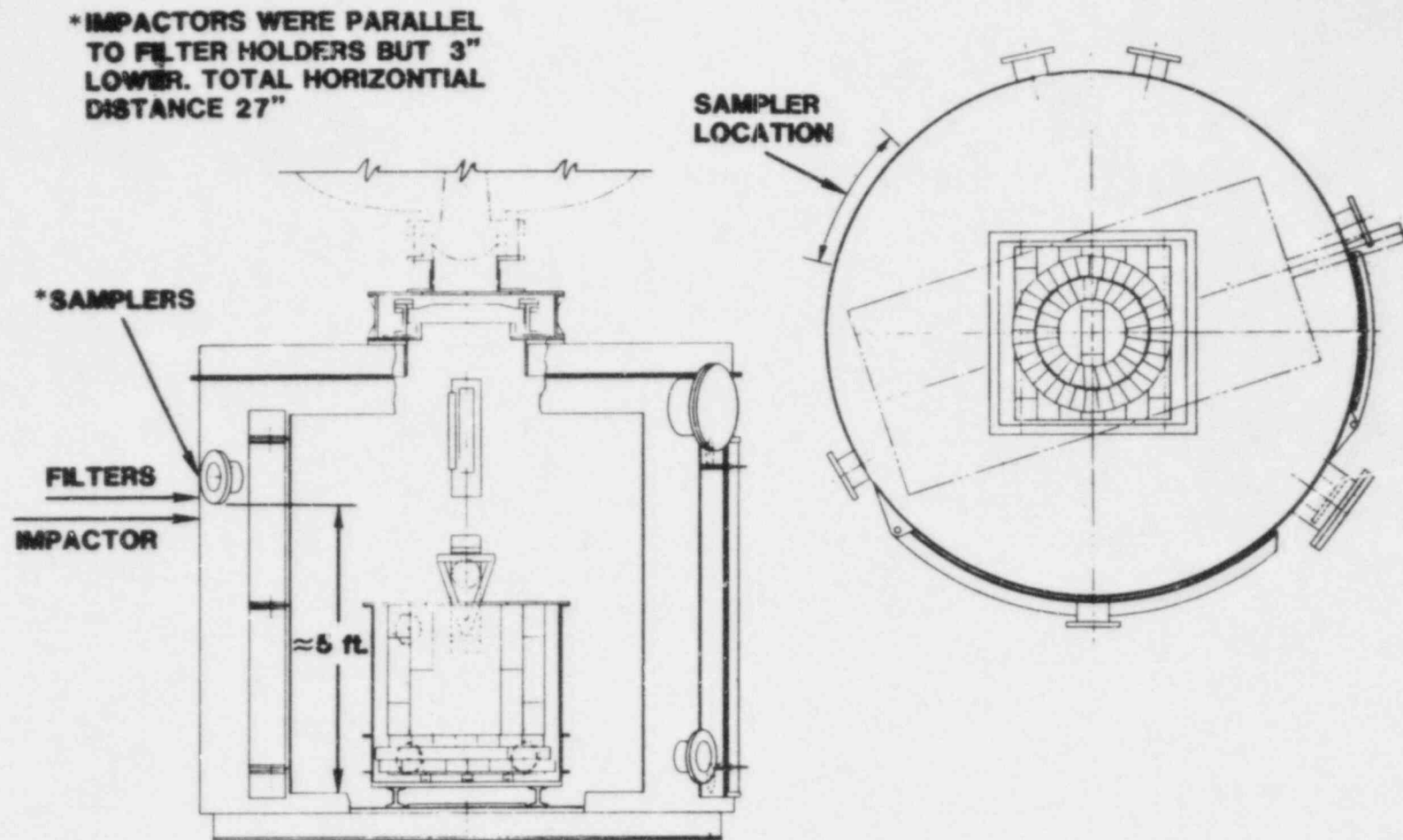
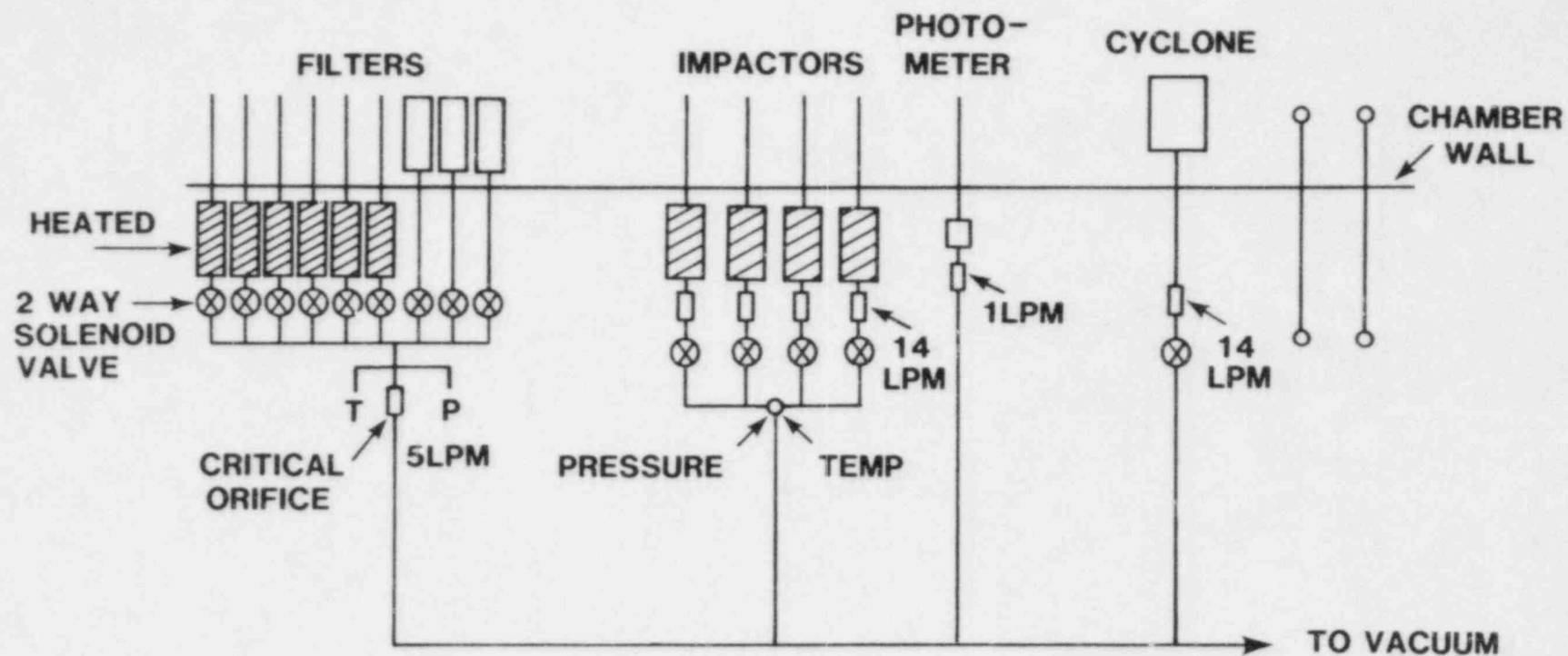


Figure II.19 Placement of Aerosol Instrumentations

CHAMBER SAMPLING SYSTEM



LOG 5 TEMP.
 4 PRESS
 17 VALVE OPENING & CLOSING
 1 PHOTODETECTOR OUTPUT

CONTROL 17 VALVES
MONITOR HEATERS

Figure II.20 Chamber Aerosol Sampling System

variation of the upward heat flux. The heat flux gauge at the center was a circular foil gauge with a mirrored ellipsoidal cavity in front. The cavity was water cooled and gas purged. The aperture of the gauge and the foil gauge were at corresponding foci of the ellipsoidal; therefore, in principle the gauge was protected from the harsh environment yet saw all the incoming radiant flux. The gauge at 4 1/2 in. from the center was a slug type gauge with a nickle slug. The shield was fastened to an instrumentation boom; it could be moved into position within one second after the completion of the melt pour, Figure II.21.

(3) Instrumentation in Magnesia Brick Crucible

(a) Temperature Measurements

The cavity bottom was instrumented with 21, 1/16-in-diameter stainless steel sheathed thermocouples at depths below the surface ranging from 1/8 in. to 6 in. The thermocouples near the surface were W-5 type and the rest were K type. Two of the thermocouples were installed in the cracks between the bricks one at 1 in. and one at 2 1/2 in. Details of the bottom thermocouple patterns are shown in Figure II.22a, II.22b.

In all, 18 thermocouples were installed in the wall of the pool region (region below the expected pool level) of the cavity at depths below the surface ranging from 1/8 in. to 4 in. The portion of the cavity wall above the pool was instrumented with eight thermocouples at depths of 1/4 in. and 1/2 in. Details of these thermocouple placements are shown in Figure II.23a, II.23b.

(b) Detection of Gap Penetration and Brick Floatation

Other than thermal measurements, the cavity bottom was provided with a 1/4 scale loose brick to study the possibility of the floating of bricks due to density differences. A set of calibrated cracks ranging from 10 mils to 125 mil wide were located on the cavity bottom to study the penetration of melt into cracks, (see Figure II.24).

(c) Crack Detection

Small-scale (10-kg) experiments using molten thermite teemed into a cavity constructed of magnesia bricks have shown that cracking of the bricks can occur. Gross damage to bricks may be an important concern in the survivability of core retention devices using refractory brick shapes. The damage is attributed to differential stress induced by the temperature gradient caused by exposing only one surface to a heat flux. Observations have only been made posttest, so that the actual time of occurrence relative to deposition of the melt is unclear. In order to determine the mechanism of crack origination, the location of a crack and the time when it occurs must be known.

The technique used in the LMF magnesia crucible consists of placing the crack diagnostics on two of the inner, lower sidewall bricks. Each brick is instrumented with several arrays of elements created from a thick-film conductive paste. Each array is connected to a

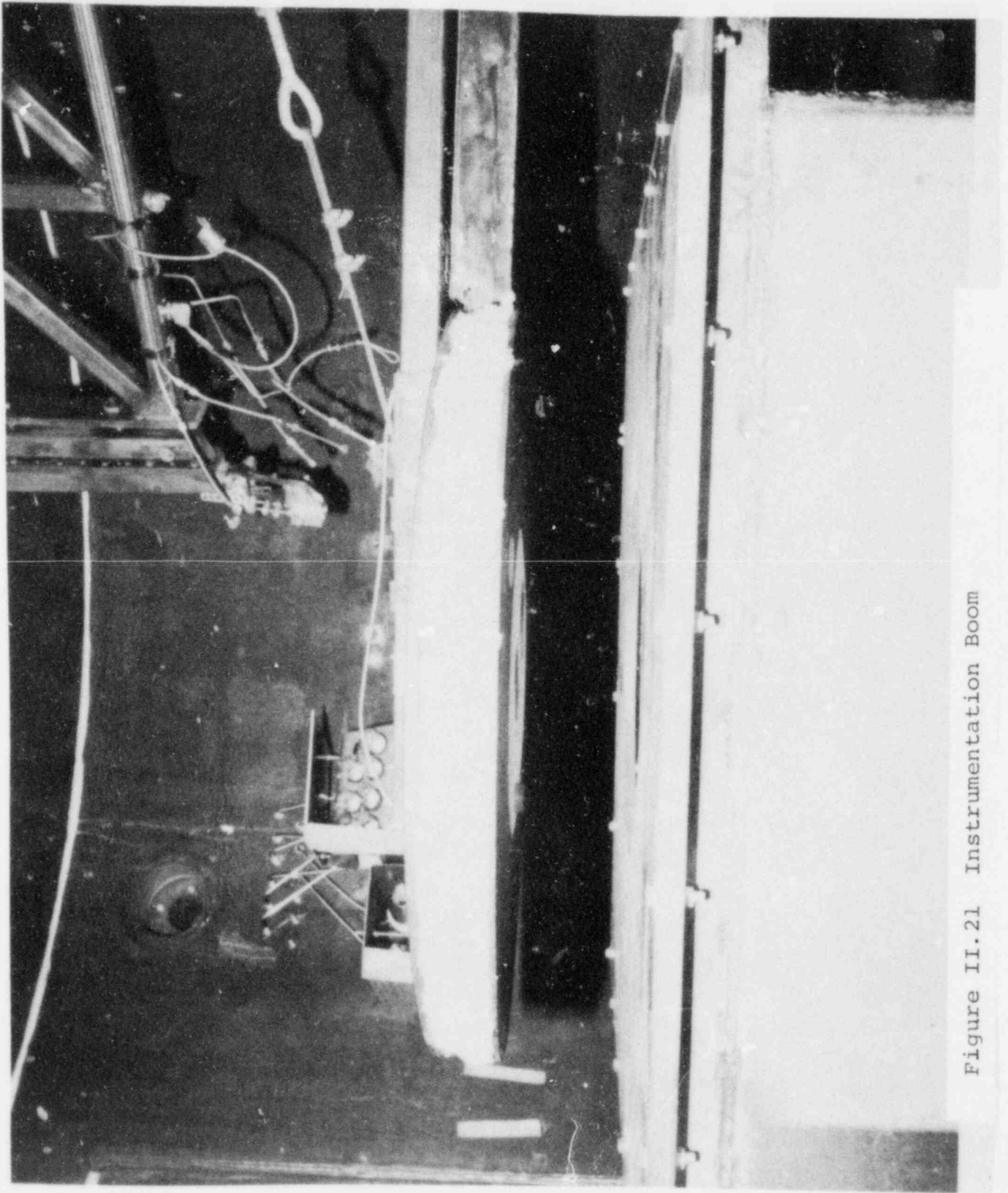


Figure II.21 Instrumentation Boom

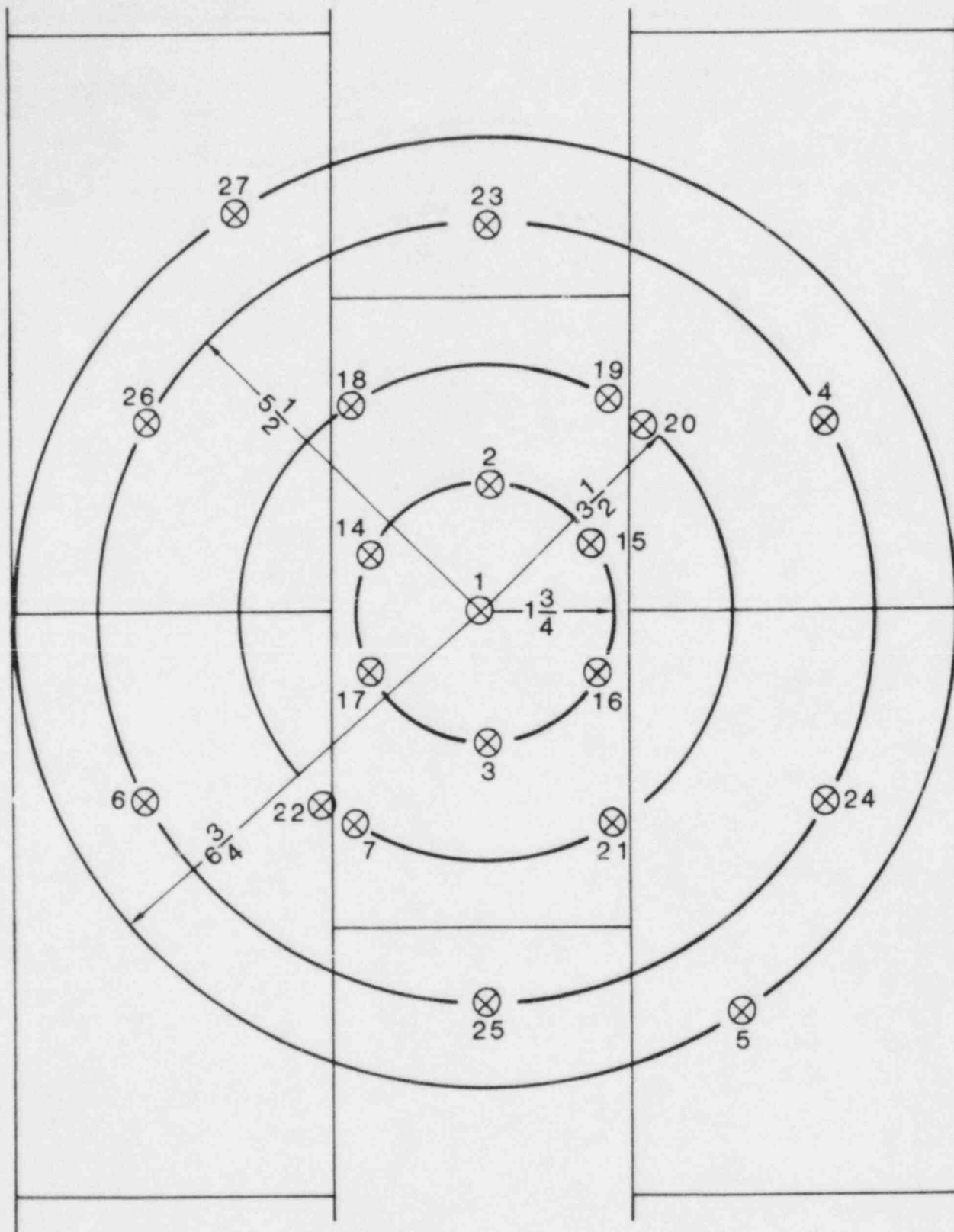
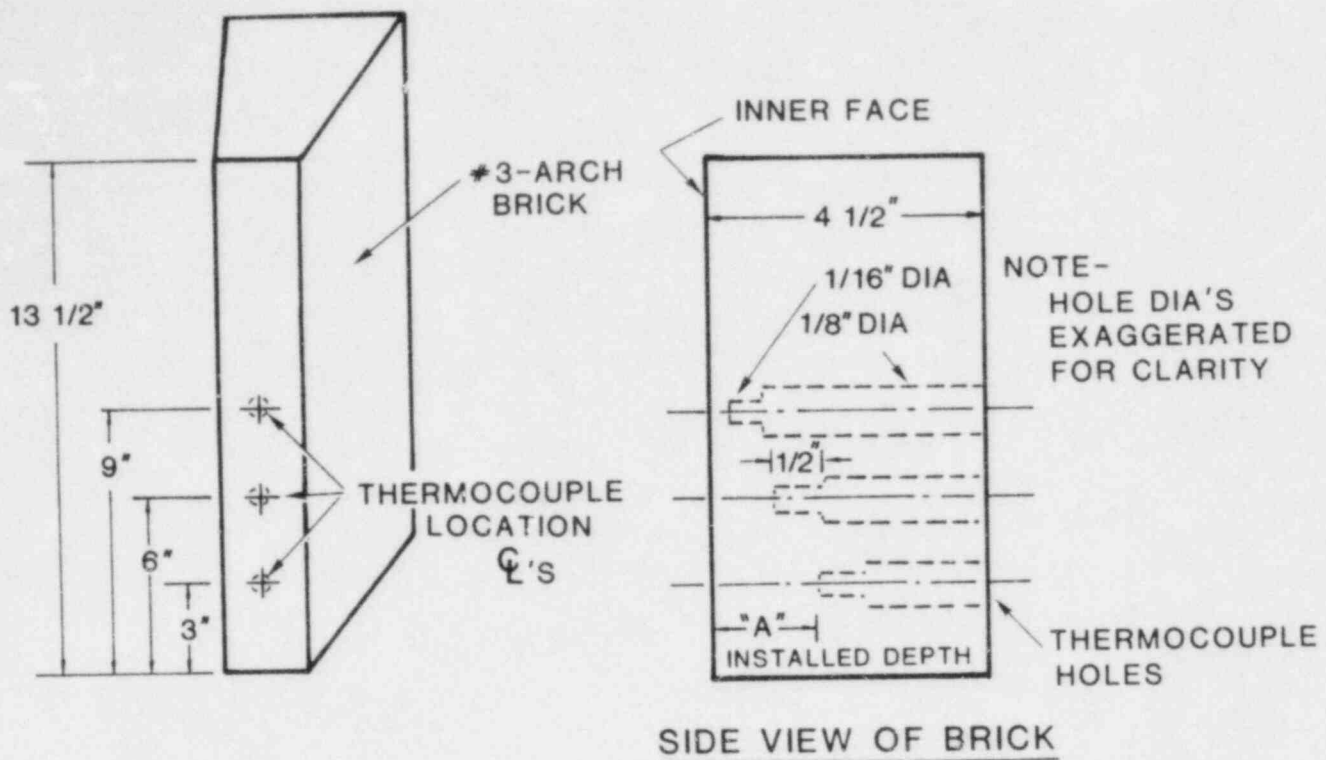


Figure II.22a Bottom Thermocouple Locations

T.C. #	DEPTH BELOW SURFACE	THERMOCOUPLE TYPE	COMMENT
1	1/8"	W-5	
2	1/4"	W-5	
3	1/2"	W-5	
4	1/4"	W-5	
5	1/8"	W-5	
6	1/2"	W-5	
7	1/8"	W-5	
8	THRU 13-CAVITY SIDEWALL T.C.'S (TYPE W-5)		
14	1 1/2"	K	
15	3/4"	K	
16	2"	K	
17	1"	K	
18	3"	K	
19	6"	K	
20	2 1/2"	K	IN CRACK BETWEEN BRICKS
21	4"	K	
22	1"	K	IN CRACK BETWEEN BRICKS
23	3/4"	K	
24	1 1/2"	K	
25	1"	K	
26	2"	K	
27	1"	K	

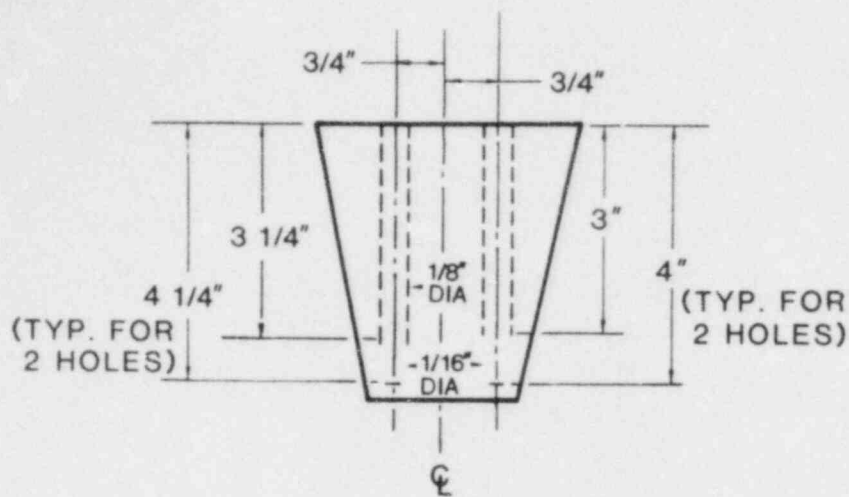
Figure II.22b Bottom Thermocouple Depths



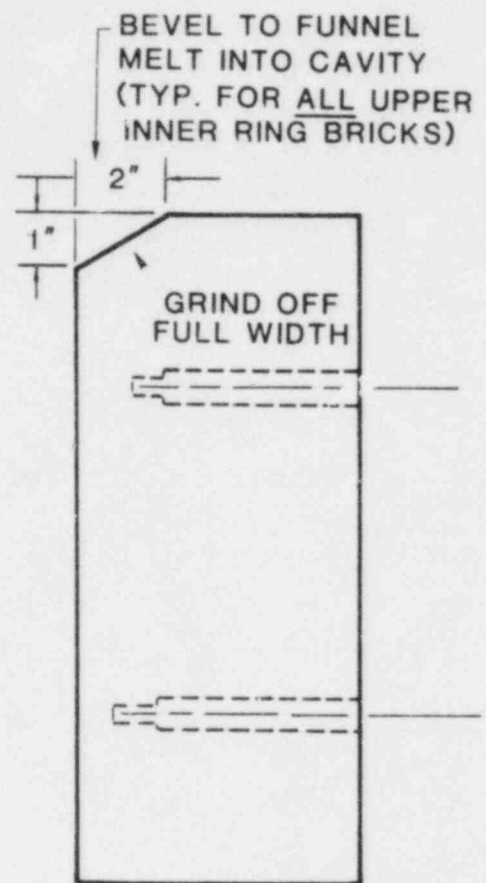
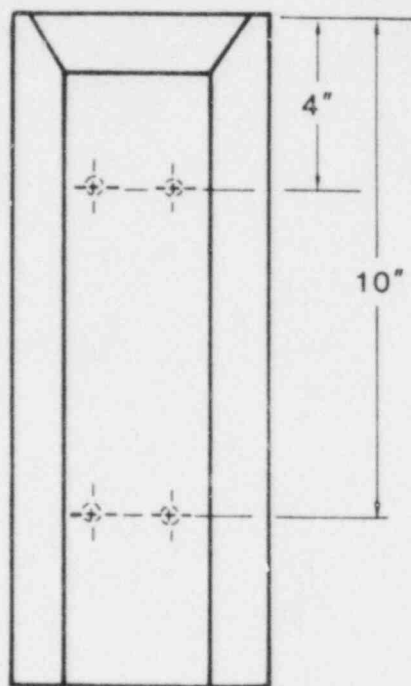
"A"-INSTALLED DEPTHS-CRUCIBLE WALL T.C.'S

	UPPER HOLE	MIDDLE HOLE	LOWER HOLE
BRICKS #1&13	1/8" TYPE W-5	1" TYPE K	2 1/2" TYPE K
BRICKS #4&16	1/4" TYPE W-5	1 1/2" TYPE K	3" TYPE K
BRICKS #7&19	1/2" TYPE W-5	2" TYPE K	4" TYPE K

Figure II.23a Sidewall Thermocouple Locations (Pool Region)
(see Figure II.17a for Brick Locations)



DRILLING FOR
HEAT TRANSFER
RATE THERMOCOUPLES



- * USE #3-ARCH BRICK
- * 2 REQ'D-SERIAL #11

Figure II.23b Sidewall Thermocouple Locations (Upper Region) (See Figure II.17a for Brick Locations).

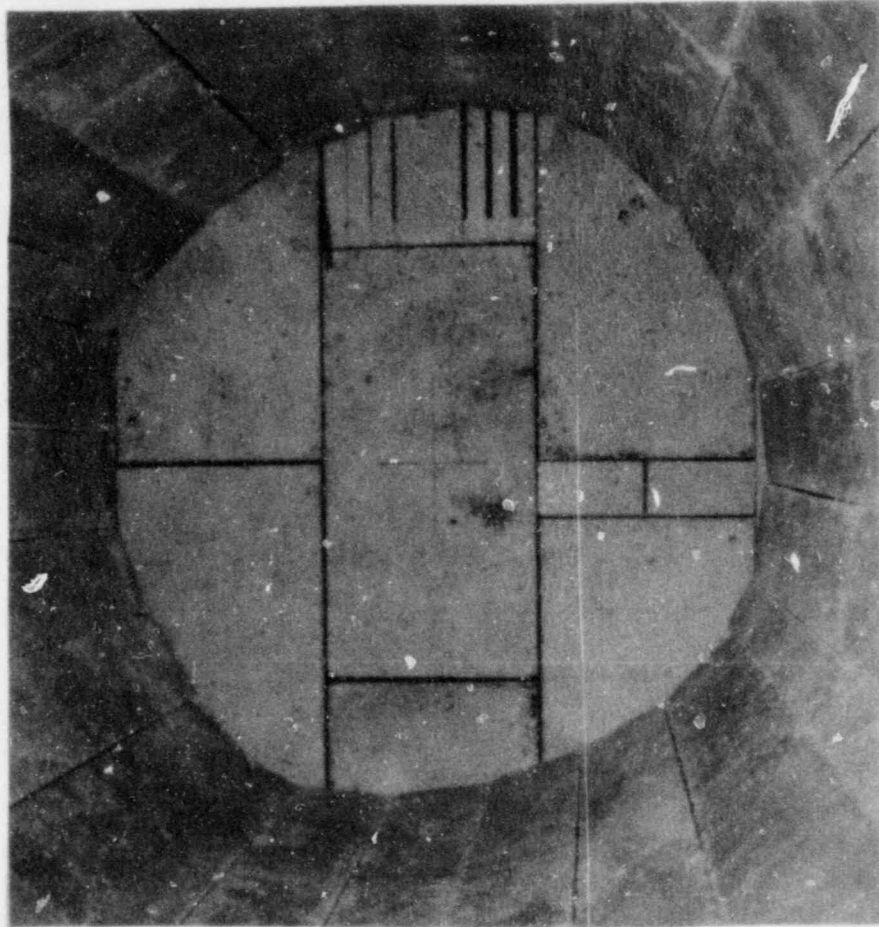


Figure II.24 View of Cavity Bottom

common voltage source through a series of fixed resistances, as shown in the electric circuit of Figure II.25. Each conductive element is used to shunt a resistor so that failure of the conductive element because of a crack causes current to flow through the respective resistance. The change in the current causes a corresponding increase in the output voltage according to the expression:

$$V_{out} = V_{in} \frac{\sum R_i}{R_5 + \sum R_i} \quad (II.2)$$

where:

- R_5 = current-limiting resistance value
- $\sum R_i$ = series sum of resistances corresponding to failed conductive element.

For example, if element 1 fails, the above equation reduces to:

$$V_{out} = V_{in} \frac{R_4}{R_5 + R_4} \quad (II.3)$$

Likewise, if element 2 also fails, the equation becomes:

$$V_{out} = V_{in} \frac{R_4 + R_3}{R_5 + R_4 + R_3} \quad (II.4)$$

Some ambiguity may occur if the elements do not fail in numerical order. For instance, if element 2 failed first and followed by 1, then equation II.2 could reduce to the form II.3 or II.4, depending on the location of the failure relative to the junction of elements 2 and 3.

The relative size and position of the elements are shown in Figure II.26. The numbered termination represents the point where small insulated wire leads are connected to the conductive elements. The brick is positioned so that the face opposite the terminations is exposed to the heat flux provided by the molten pool. Figure II.27 shows one of the bricks in place during the assembly of the test. Flat ribbon cable is used to connect the individual elements to the resistive network located outside the interaction chamber.

The conductive elements are applied to the bricks in paste form using a mask. The paste is then stabilized by firing at 873 K (600°C) to drive off the volatile species. Cables are attached to the conductive elements using a high-temperature solder. Five networks are used on each of two bricks. A common 10-Vdc power supply is used to power each electrical circuit. The outputs are connected to two transient digitizing recorders to retain the data on floppy disk storage.

III. Events of the Test

a. Heating and Melting

(1) Pretest Calculations

A heating schedule was designed before the test using the SINDA thermal model of the susceptor/crucible/charge assembly [3]. See

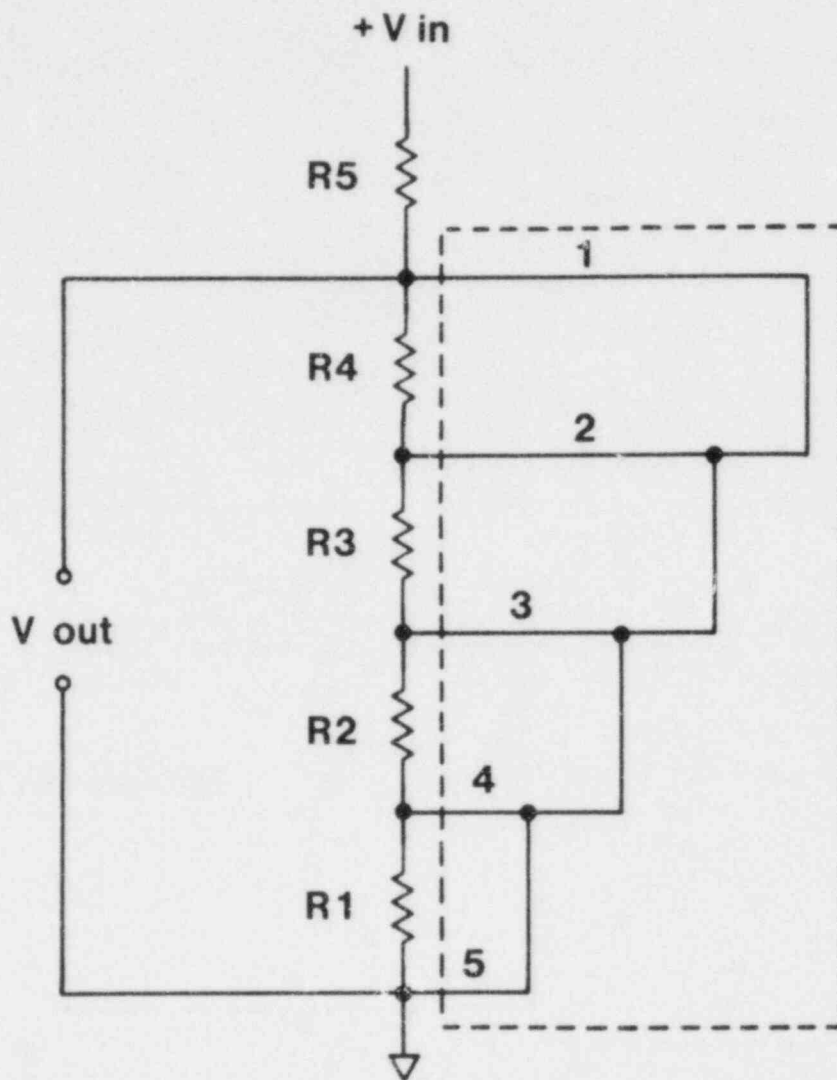


Figure II.25 Electrical Schematic for Conductive Element Array of the Thick Film Crack Detector

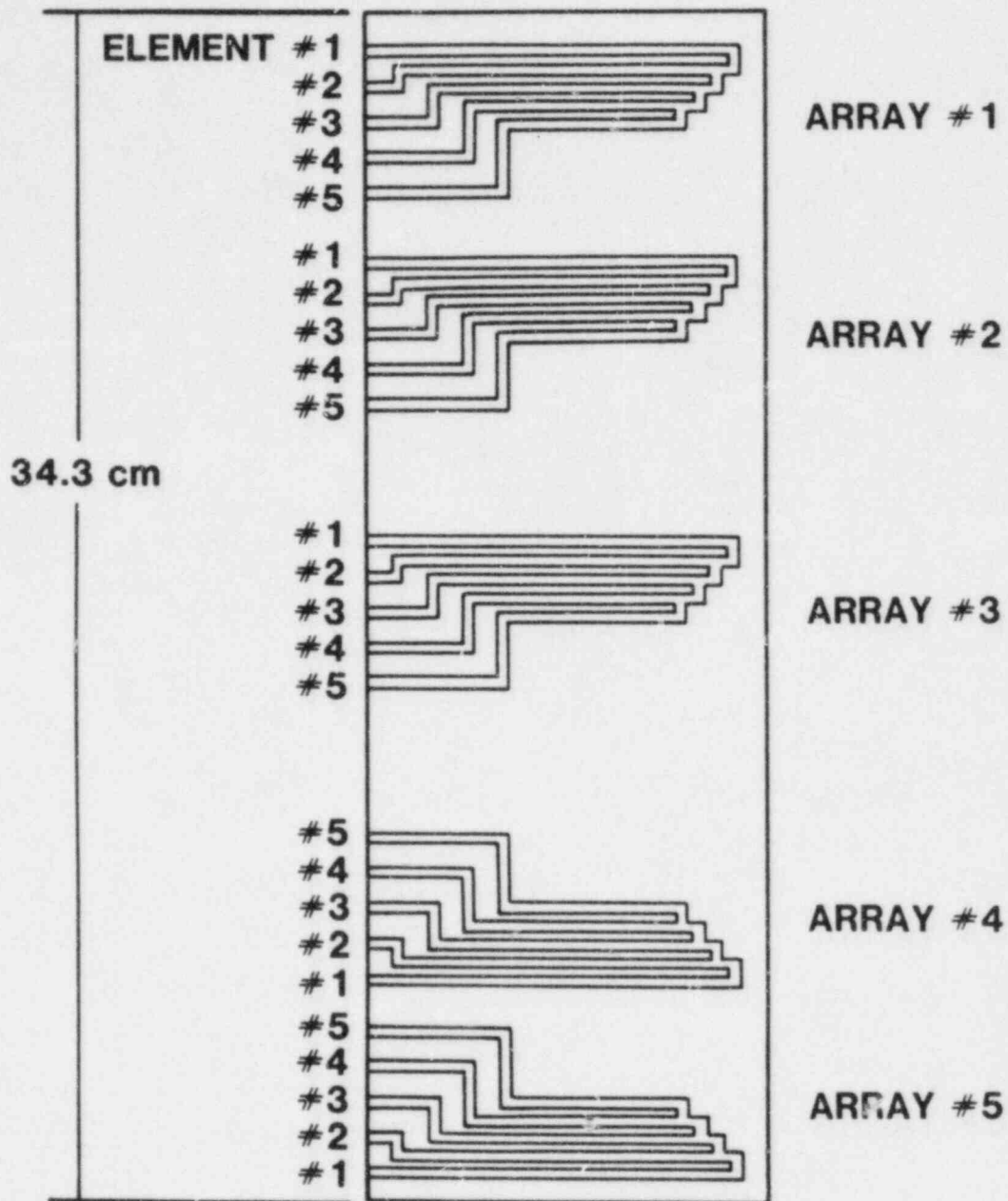


Figure II.26 Schematic of Brick with Crack Detection Elements

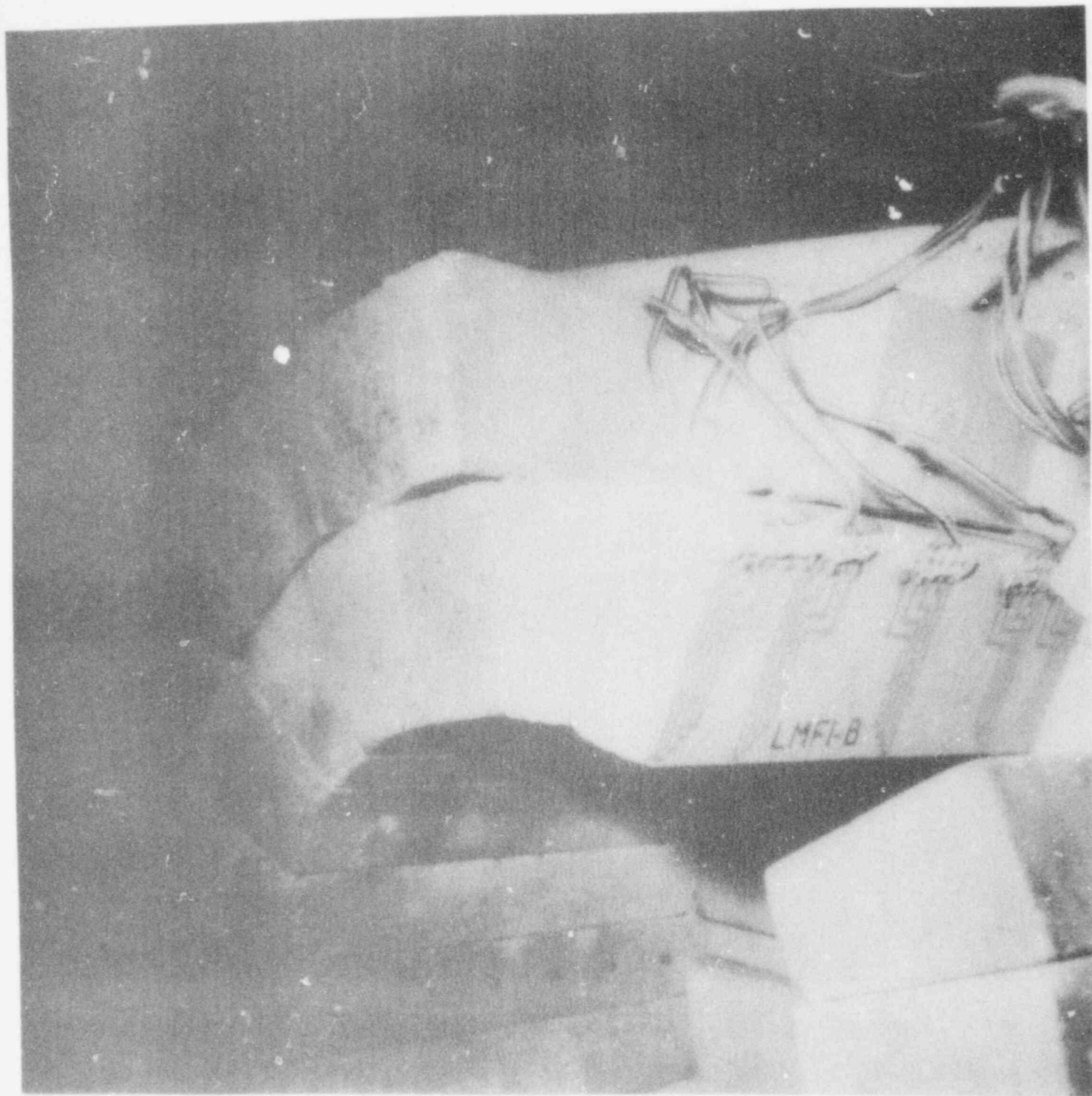


Figure II.27 Instrumented Brick in Partially-Assembled Crucible

Table III.1. The resulting temperature histories in the susceptor and two locations in the charge are shown in Figure III.1. The susceptor was to be ramped at a rate of 300°C/hr below 1473 K (1200°C) and at 500°C/hr between 1473 K (1200°C) and 2673 K (2400°C). The lower rate below 1473 K was to avoid thermal stress problems with the crucible assembly especially the tungsten liner. Several temperature plateaus were programmed, 473 K (200°C), 1473 K (1200°C), 2273 K (2000°C), and 2673 K (2400°C) for instrument checks. In addition, the plateau at 2675 K was also designed to soak the charge before the susceptor temperature was increased to above the melting range of the charge. At the end of the 2675 K soak (12 hrs into the test), the susceptor was to be brought to 2923 K within three hours. Total melt was estimated to occur between 18 and 20 hrs into the test, depending on the assumed degree of convective enhancement of heat transfer within the melt. The calculation presented in Figure III.1 was for an effective melt thermal conductivity of 2.07 Btu/hr-in-°F (42.9 W/mK). This represented a convective enhancement of a factor of 8.6 over pure conduction*.








(2) Actual Temperature History

During the first eight hours of testing, the heating schedule and the temperature and power history followed essentially the pretest prediction, Figure III.2. The coupling efficiency was found to be slightly lower than the previously determined value of 0.55**; as a result the temperature history of the susceptor and the charge showed a lag of about one-half hour or 100°C at 10 hrs. At this time, it was decided to change the soaking plateau to 2573 K (2300°C). One of the reasons was to make sure that the thermocouples would still give good readings and could be used as a standard of comparison with the other temperature instrumentations. During the 2573 K soak, readings from the pyrometers, thermocouples, and ultrasonic thermometers were compared. The readings from the ultrasonic thermometer showed variations over 100°C; it appeared that as the susceptor temperature was increased to beyond 2673 K, the pyrometer would be the only temperature instrumentation available to guide the experiment. The heating schedule was therefore modified. A more conservative approach was taken. Instead of ramping directly to 2923 K (2650°C), a series of intermediate ramps was taken: 2773 K (2500°C), 2873 K (2600°C), and 2923 K (2650°C), Figure III.3a. Shown in Figure III.3b is the corresponding power history. At 16.3 hrs, with the susceptor at 2923 K (2650°C) the charge center temperature as indicated by the Ircon pyrometer began to rise sharply and beginning at 16.7 hrs the charge center displayed a melting plateau at 2798 K (2525°C). The melting plateau lasted 0.6 hrs beyond which the charge center temperature again started to rise rapidly. At 18 hrs into the test the charge

*Current best estimate of the thermal conductivity of molten UO₂ is 5 W/mK (Private Communication, J.K. Fink, ANL)

** (It is also possible that the carbon felt insulation might have been graphitized (graphite is more conductive than carbon) due to the unusually long preheat before the test, see Section II.a(1), p 5.)

TABLE III.1 Heating Schedule for the Susceptor

Time		Susceptor Temp °C		Power (η=0.55) (Dial Reading)
0	0:40	Rm - 200		36
0:40	1:10	200 -		5
1:10	2:00	200 - 450	300°C/hr	56
2:00	3:00	450 - 750		73
3:00	4:00	750 - 1050		87
4:00	4:30	1050 - 1200		95
4:30	5:30	1200		31
5:30	6:00	1200 - 1450		135
6:00	6:30	1450 - 1700		155
6:30	7:06	1700 - 2000		175
7:06	8:00	2000		60
8:00	8:30	2000	500°C/hr	55
8:30	9:00	2000 - 2250		184
9:00	9:30	2250 - 2400		207
9:30	10:00	2400		84
10:00	10:30	2400		80
10:30	11:00	2400		78
11:00	12:00	2400		76
12:00	13:00	2400		131
13:00	14:00	2589 - 2679		145
14:00	15:00	2679 - 2711		144
15:00	16:00	2715		129
16:00	17:00	2715		113
17:00	18:00	2715		105
				116
18:00	19:00	2715		116

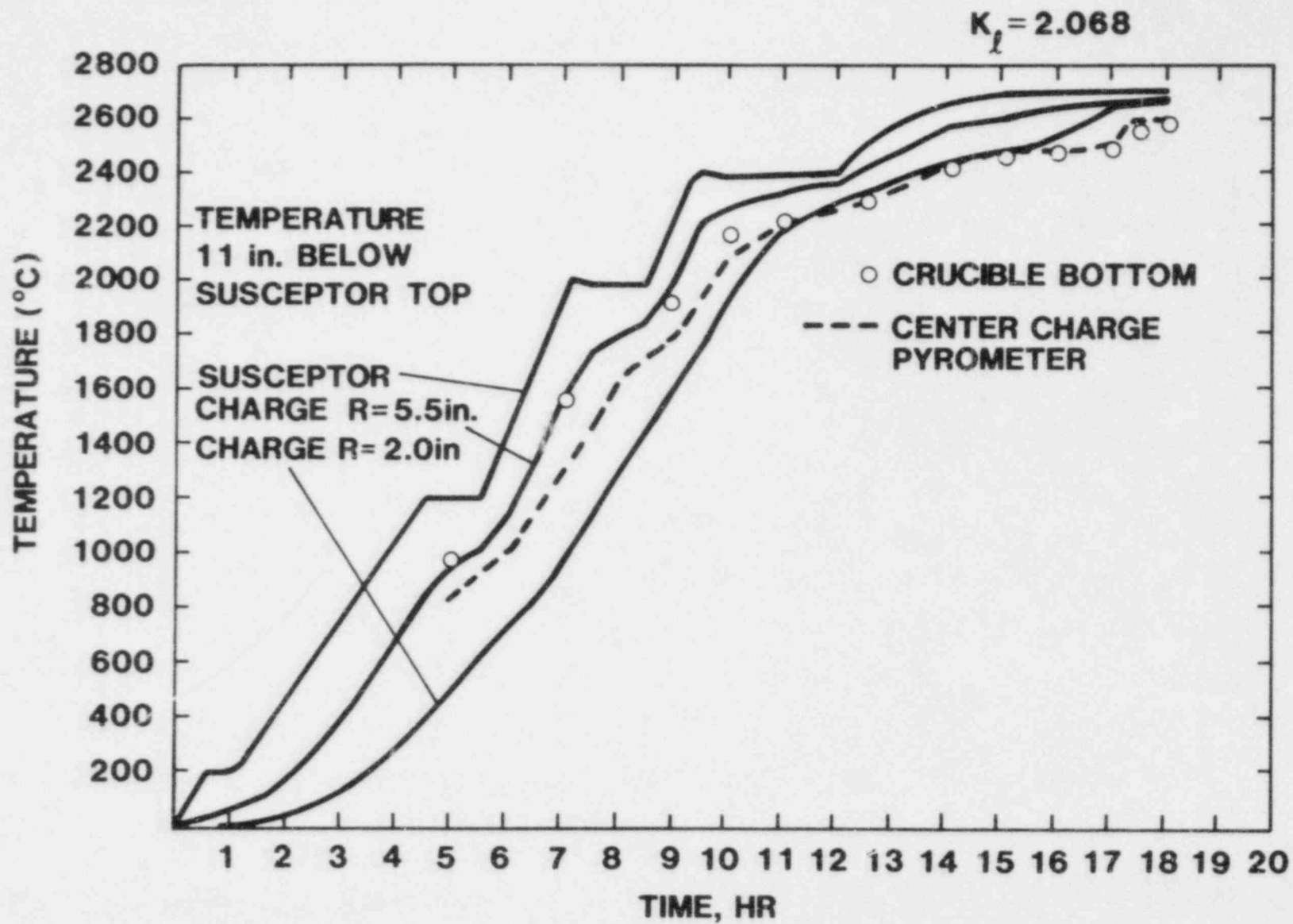


Figure III.1 Pre-Test Thermal Calculation (Melt Thermal Conductivity 2.068 Btu/hr-in-°F, 42.9 W/mK)

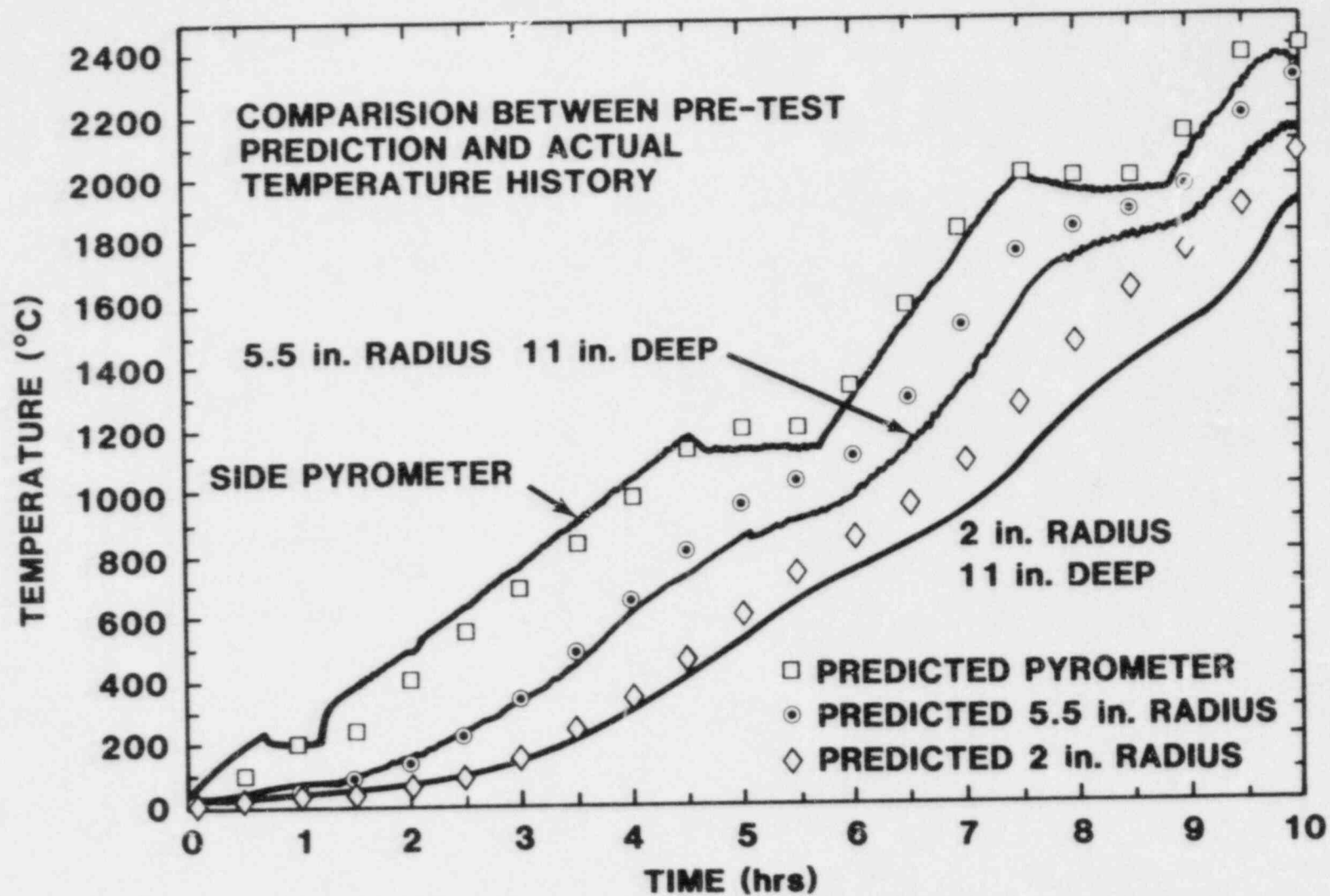


Figure III.2 Comparison Between Pre-test Prediction and Actual Temperature History

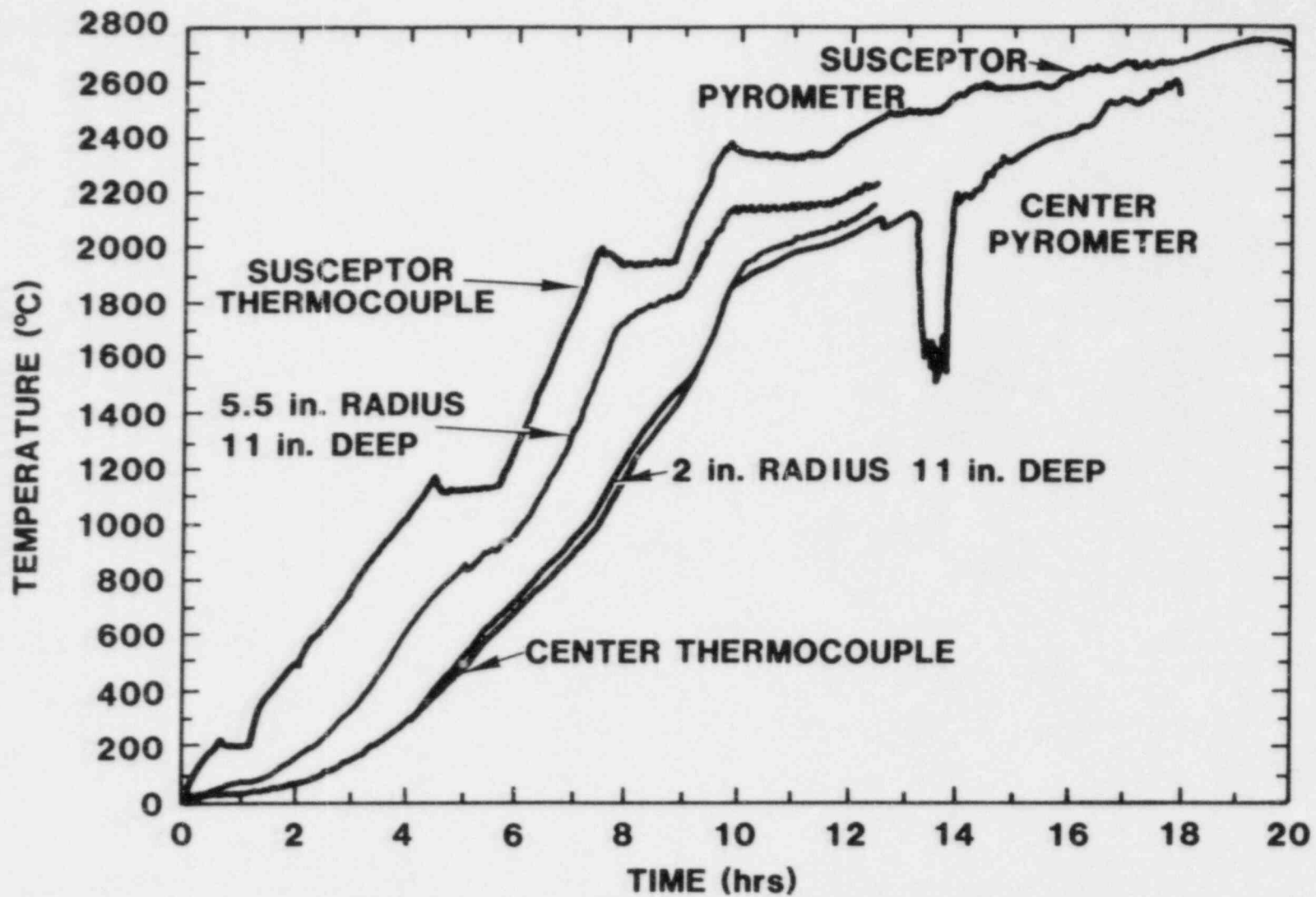


Figure III.3a Susceptor and Charge Temperature During Test

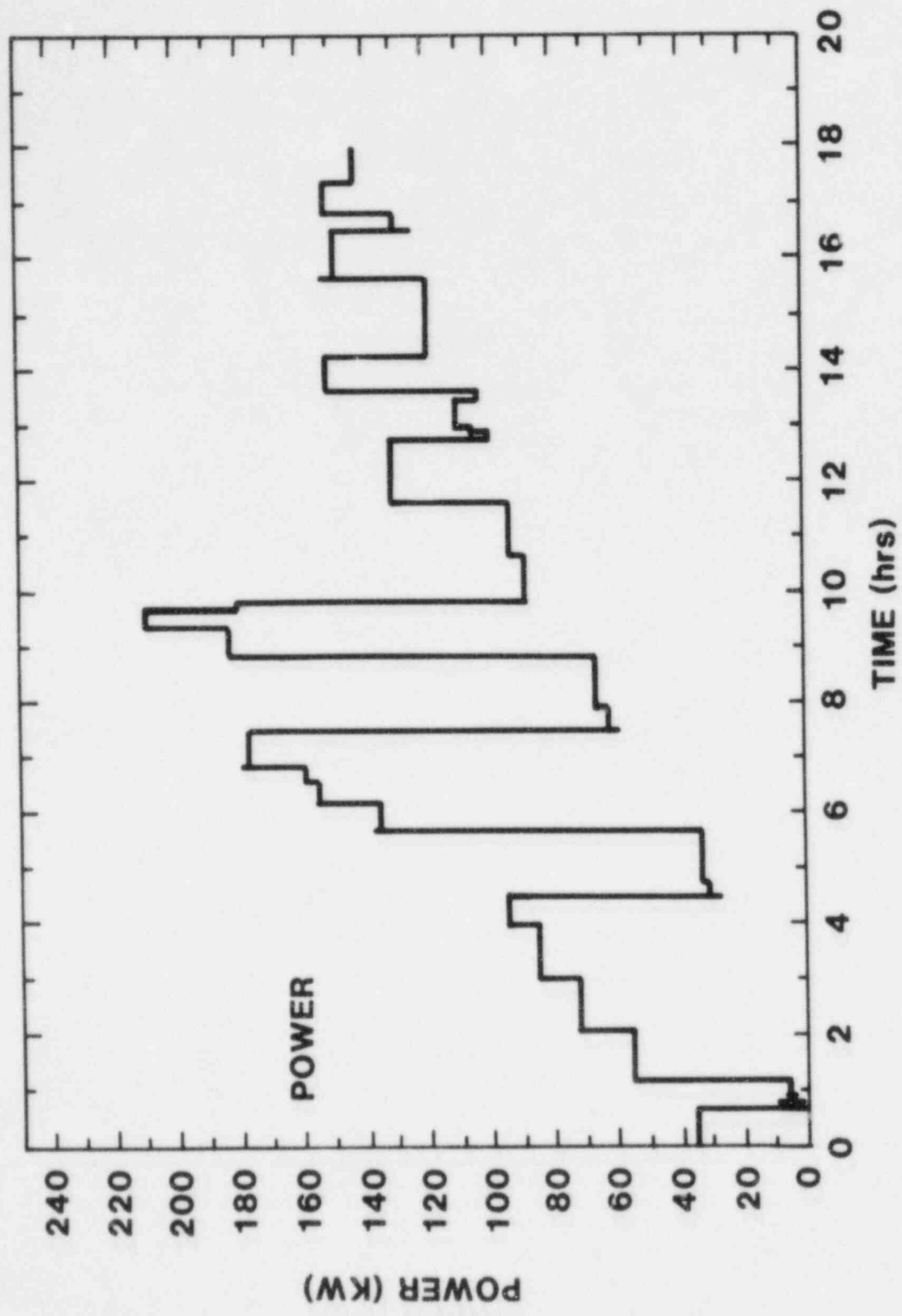


Figure III.3b Power (Applied) History

center reached 2873 K (2600°C) and a decision was made to tap. After the first attempt, which failed, the bottom of the crucible was no longer insulated by the radiation shields. To compensate for the heat loss, the susceptor temperature was increased to approximately 3023 K (2750°C). Four attempts were required before the crucible was successfully tapped at 19:56:29 hr. The power was kept on until 55 seconds after the successful tapping of the crucible. Details of tapping will be discussed in later sections.

(3) Comparison of Temperature Sensors

(a) Thermocouple and Pyrometer

The reading of the center Ircon pyrometer cannot be easily compared with thermocouples because during the early part of the experiment while thermocouples were still operational, sufficient gradient existed along the pyrometer wall that there was no direct correspondence between thermocouple and pyrometer readings.

A direct comparison can be made with the thermocouple readings and the pyrometer readings for the susceptor. The comparison is excellent, see Figure III.4. Over the range of 1573 K (1300°C) to 2673 K (2400°C), the difference between the two was no more than 25°C. The largest difference occurred during rapid ramping.

(b) Ultrasonic Thermometer and Other Temperature Instrumentation

At this time only data from the susceptor ultrasonic thermometers (UT's) are fully reduced, therefore, comparisons will mainly be made with corresponding instrumentation in the susceptor.

(i) Consistency of UT Data

Figure III.5 shows a comparison of the five inch deep zone of the three graphite susceptor UTs (UT1, UT4, UT6) and comparisons between UT4 and the corresponding thermocouple and pyrometer data. Throughout the test, UT1 generally read higher than the other susceptor UTs. The reason is unknown at this time, but it should be noted that UT1 was placed in a larger diameter hole in the susceptor, otherwise it was similar to the others. UT6 showed problems with extraneous signals as early as 1473 K (1200°C). The gradual degradation resulted in it being useless above 2273 K (2000°C). The fact that this degradation occurred at such a low temperature is unusual, and the mechanism is unknown at this time. Generally the readings of the susceptor UTs agreed to within 50°C, although in some temperature regimes UT1 was reading high by over 100°C. However, during the last few hours of the test only UT4 gave useful results (>2500°C).

(ii) Comparison between UT and Thermocouples

UT and thermocouple can be compared up to 2673 K (2400°C) beyond which shunting effect makes the thermocouples useless. Generally, in

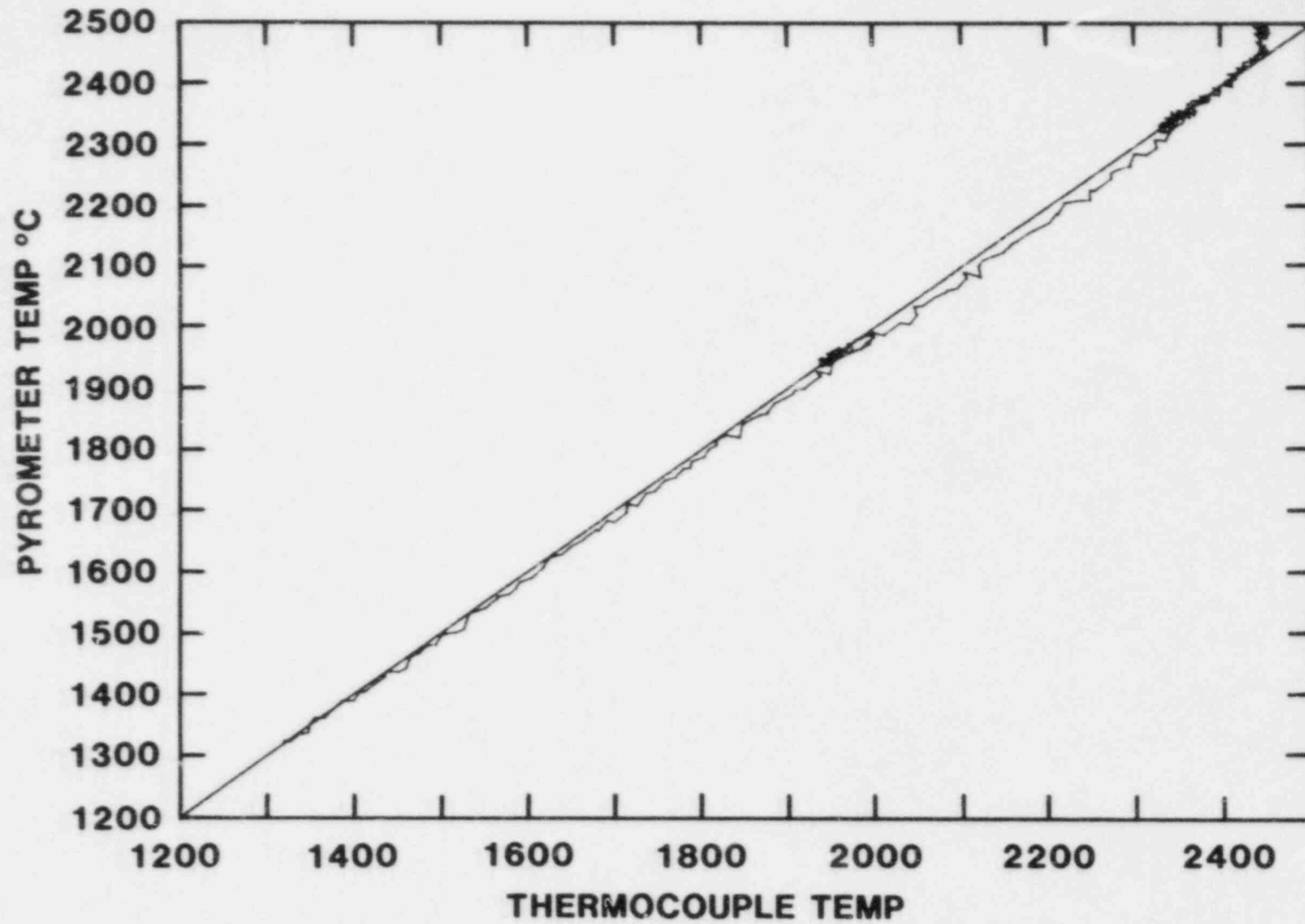


Figure III.4 Comparison Between Pyrometer and Thermocouple Measurements of the Susceptor Temperature

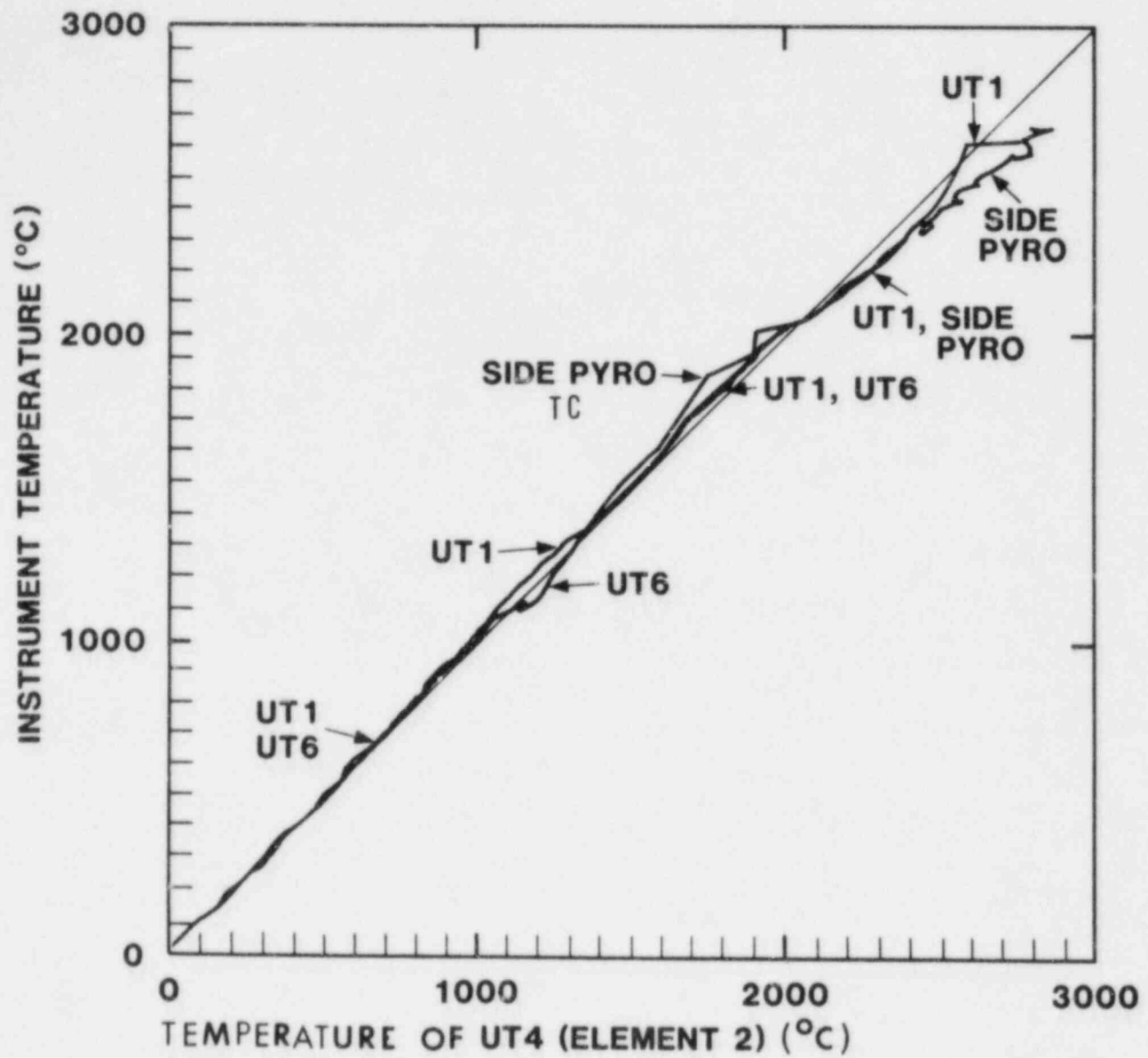


Figure III.5 Comparisons of Susceptor UTs and Corresponding Thermocouples and Pyrometers

the susceptor the agreement is within 50°C almost everywhere, except at about 2173 K to 2273 K (1900°C-2000°C) where the UT reads up to 75°C lower than the thermocouple, Figure III.5. This may result partly from the accuracy of the calibration curve fit for the UT's in this regime.

Preliminary analysis of UT's in the charge showed that the signal qualities of these UT's were better than the susceptor UT's. Below 2073 K (1800°C) the agreement with thermocouples is better than $\pm 60^\circ\text{C}$.

(iii) Comparison between UT and Pyrometer

Below 2673 K (2400°C) comparison between UT and pyrometer readings is similar to that of UT and thermocouple. Beyond 2673 K (2400°C) the discrepancy gets progressively larger, Figure III.5. The UT calibration curve has a linear extrapolation above 2673 K (2400°C) which is known to result in the UT readings being slightly high, but the effect is expected to be only a few tens of degrees at most. However, the UT readings were sometimes as much as 150°C higher than the pyrometer readings. At the time of the first attempt to tap, the UT reading was approximately 100°C higher than the side pyrometer readings. The readings at that time were about 3053 K (2780°C) and 2943 K (2670°C) respectively.

b. CO Data

The carbon monoxide concentration in the furnace atmosphere was continuously monitored during the test. The main purpose was to use it as a possible indicator of melt/graphite interaction as a result of crucible failure. Oxygen released from the melt charge due to heating was also a possible source of CO.

The CO concentration during the test is plotted as a function of test time, Figure III.6. Also plotted is the susceptor temperature. Apparently below 2773 K (2500°C) the CO concentration usually increased during heating. When the temperature was kept constant the CO concentration fell. Above 2773 K (2500°C) the CO concentration seemed to follow the level of temperature (rather than the rate). This trend above 2773 K was probably related to the release of oxygen as melting took place. Another source is the reaction of BeO (vaporized) from the thermocouple with the graphite susceptor or carbon felt insulation.

c. Displacement Gauge Data

A linear variable differential transformer (LVDT) was used to measure the vertical axial movement of the Ta-10W crucible and the furnace. The LVDT had one inch displacement and was mounted in a water-cooled block 16 in. above the crucible top. The top of one of the instrumentation pass-through welded to the crucible lid at 2 in. from the crucible center was the measuring point of the LVDT. A tantalum tube using a ball and socket arrangement was connected to the top of the protection tube. A 0.75 in. aluminum oxide coupler was placed between the tantalum tube and the LVDT push rod for temperature

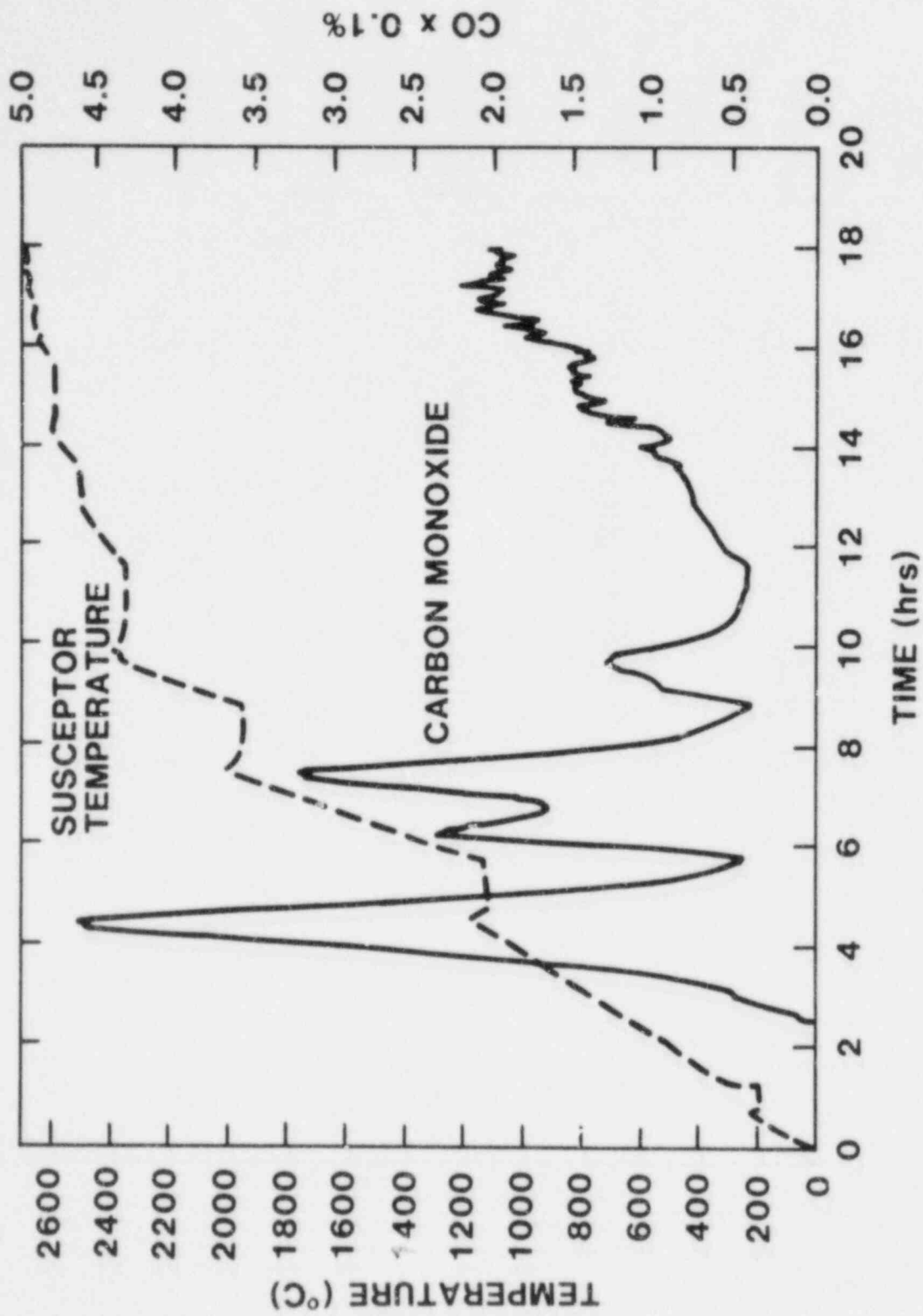


Figure III.6 CO Concentration in the Furnace

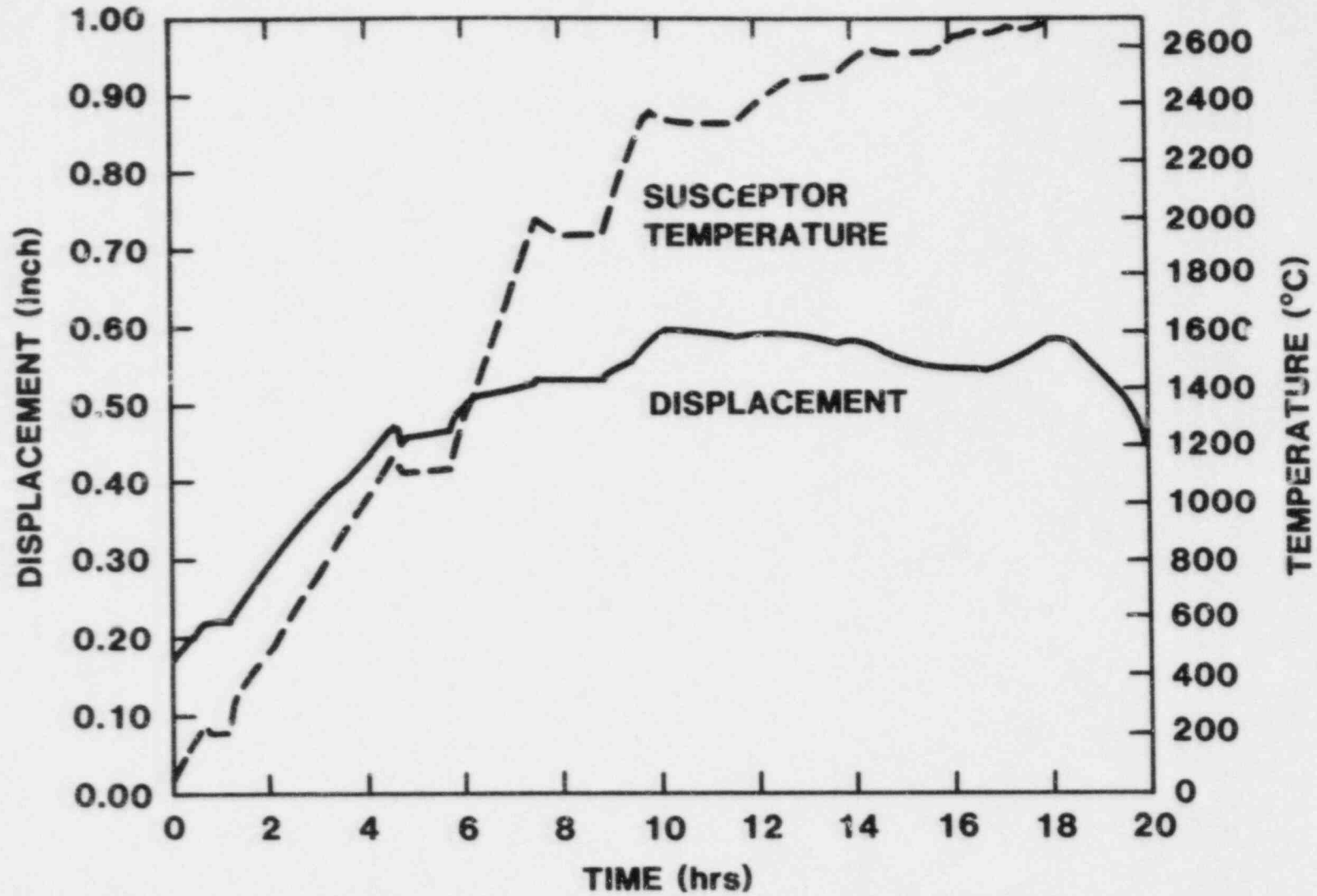


Figure III.7 Displacement Gauge Data

isolation. Spring tension in the LVDT provided the necessary pressure to hold the assembly together.

The output of the LVDT and the susceptor temperature are plotted in Figure III.7. Below 1473 K (1200°C) the crucible displacement followed exactly the temperature of the crucible. The total movement of the LVDT was 0.25 in. Whereas the total expansion due to the graphite and the Ta-10W crucible calculated from published expansion data was 0.26 in. Between 1400°C and 1900° the crucible movement was smaller than expected from thermal expansion but for the ramp between 2173 K (1900°C) and 2573 K (2300°C) the crucible movement again could be totally attributed to thermal expansion. Beyond 2573 K (2300°C) the crucible lid appeared to be sagging until about 17 hrs in to the test. Between 17 and 18 hrs the crucible moved up slightly and beyond 18 hrs the crucible again sagged. The sagging between 18 and 20 hrs is probably related to deformation caused by increasing susceptor temperature.

d. Tapping

(1) Slugs Fired and Drain Time

The first attempt to tap was made at 18:03:23, unsuccessfully. Following that, three more attempts were made. The crucible was successfully tapped on the fourth attempt. Two kinds of slugs were used steel ball and lead slug. The slugs fired for the four attempts were: 1) two steel balls, 2) one lead slug, 3) one lead slug, 4) one steel ball. In the fourth attempt the gun was fired at 19:56:29 hr into the test. It took the melt four minutes and 15 seconds to be totally drained. The furnace power was maintained until 55 seconds after the crucible was successfully tapped.

(2) Description of the Teem

The teem was recorded on television. The camera looked into the chamber through a port on the south side. A complete recording of the teem together with a description of the LMF and the assembly of the experiment have been made into an eight minute video film entitled, "Large-Scale Core Melt Interaction Experiment". Only a brief description of the teem will be given here.

After the gun was fired, it took slightly under one second for the melt to arrive at the opening of the crucible. Rather than a single consistent stream, the melt flow is best described as a shower of streams. Very little time was required for the melt to develop into a steady shower lasting approximately one minute. The individual streams continued to move back and forth in the field of view but almost all the melt ended up in the MgO crucible. During this time the pour was accompanied by active aerosol generation; at times the streams of shower appeared to be engulfed in a white billowing fog. The pour rate slowed down after a minute. At two minutes into the pour, the melt stream came to an almost complete stop for about one second, then it started to build up again. The shower moved to the east (right of screen) and part of the stream hit the steel top

plate of the MgO crucible. After about 15 seconds the melt shower turned into several, more or less, consistent streams continuing to move right and left. The streams reverted back to showers after about 30 seconds. More than a quarter of the shower streams landed west of the crucible opening on the steel top plate. Twenty-five seconds later (three and one-half minutes into the pour) the melt shower shifted toward the south (toward the camera) and the melt at this time appeared to have very little superheat. Crusts were forming on the streams. As a melt stream hit a surface, the crust split and separated from the stream. The team stopped 4 minutes and 15 seconds after tapping. Twenty-three seconds later a few frozen chunks fell on the steel top plate of the MgO crucible.

IV. Data From Test

a. Aerosol Data

(1) Sampling Scheme

A sampling scheme to yield the greatest amount of information on the source term was determined, based on model calculations. Qualitatively speaking, it is desirable to have higher resolution in samples where concentration is changing most rapidly. This occurs during the first few minutes of the test.

The source term is a rapidly falling function of time producing a concentration which rises very quickly and then decays. The losses from venting and settling are small compared to the source during this initial period as well. The first few minutes of the test provide the best information and this is where the sampling was concentrated.

The sampling scheme shown in Table IV.1 was formulated based upon the above considerations. Figure IV.1 graphically illustrates the timing of the sampling scheme. Sample flow rates were adjusted so that adequate filter loading was achieved.

(2) Size Distribution

Size-distribution plots obtained from the Anderson Impactors are given in Figures IV.2a-d and IV.3a-d. The aerosol appears to be trimodal in the early stages with the subsequent loss of the two larger modes later in the test. The larger modes are assumed to be caused by the splashing of the melt on the crucible lip and top. They are assumed to be generated by some mechanical break-up mechanism. Electron micrographs will provide more information.

(3) Aerosol Concentration

Shown in Figure IV.4 is a plot of the mass concentration calculated from the filter samples and impactor samples. The concentrations are based on in-chamber conditions. Discrepancies appear between mass concentration measured by impactors and measured by filters. This may have been caused by differences in inlet sampling efficiency, transport efficiency, internal losses in the impactor,

TABLE IV.1

Sampling Scheme for Aerosol

Filter Sample Sample Time (min)

1	0.0 to 0.5
2	0.5 to 1.0
3	1.0 to 1.5
4	1.5 to 2.0
5	2.0 to 3.0
6	3.0 to 5.0
7	10.0 to 15.0
8	15.0 to 30.0
9	40.0 to 50.0

Impactor Sample Time (min)

1	0.0 to 1.0
2	2.0 to 5.0
3	10.0 to 15.0
4	15.0 to 30.0

Time Resolved Sample Time (min)
Deposition Sampled

1	0.0 to 1.0
2	1.0 to 2.0
3	2.0 to 5.0
4	5.0 to 30.0
5	30.0 to end

TIMING SCHEME

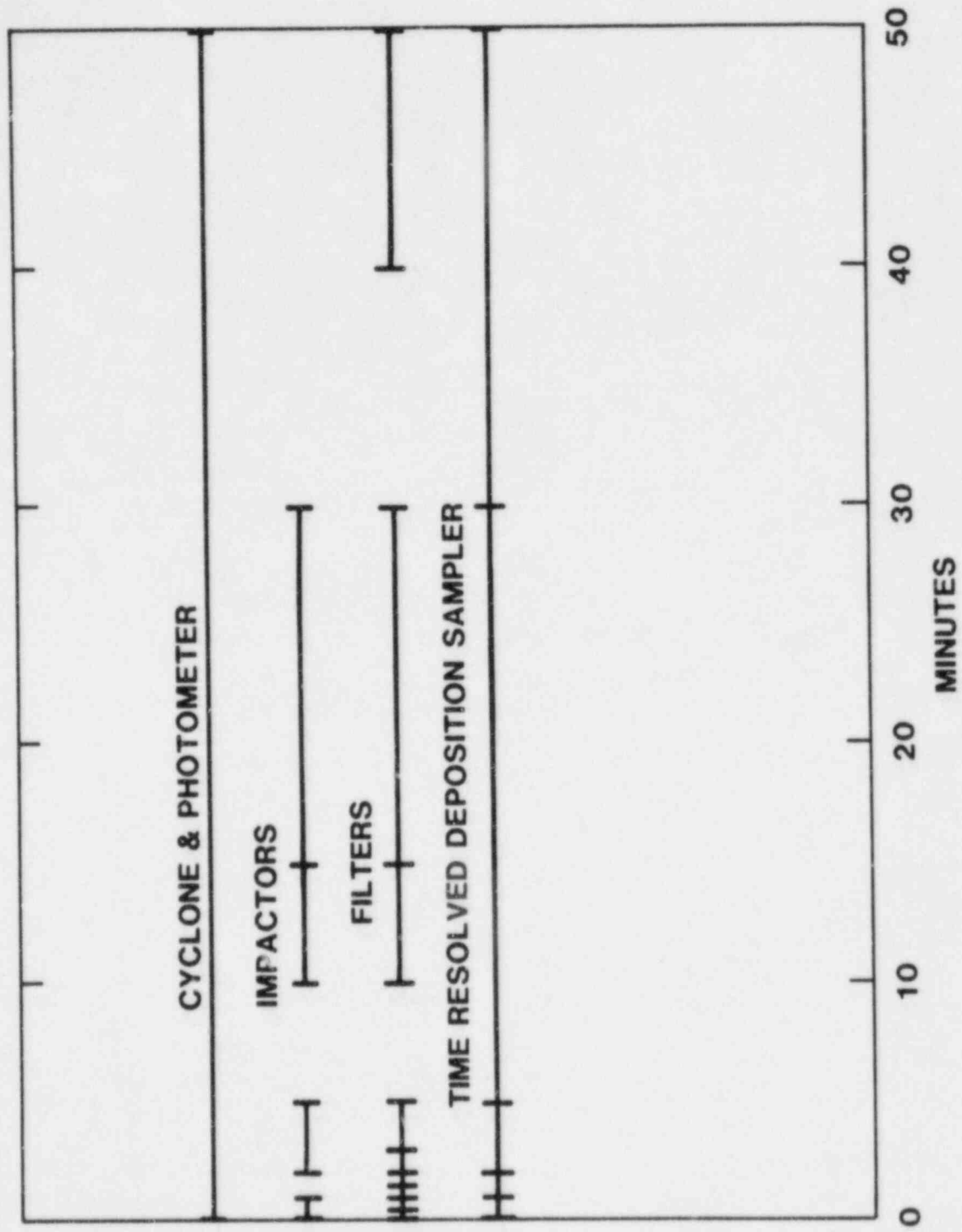


Figure IV.1 Aerosol Sampling Scheme

ANDERSON #1

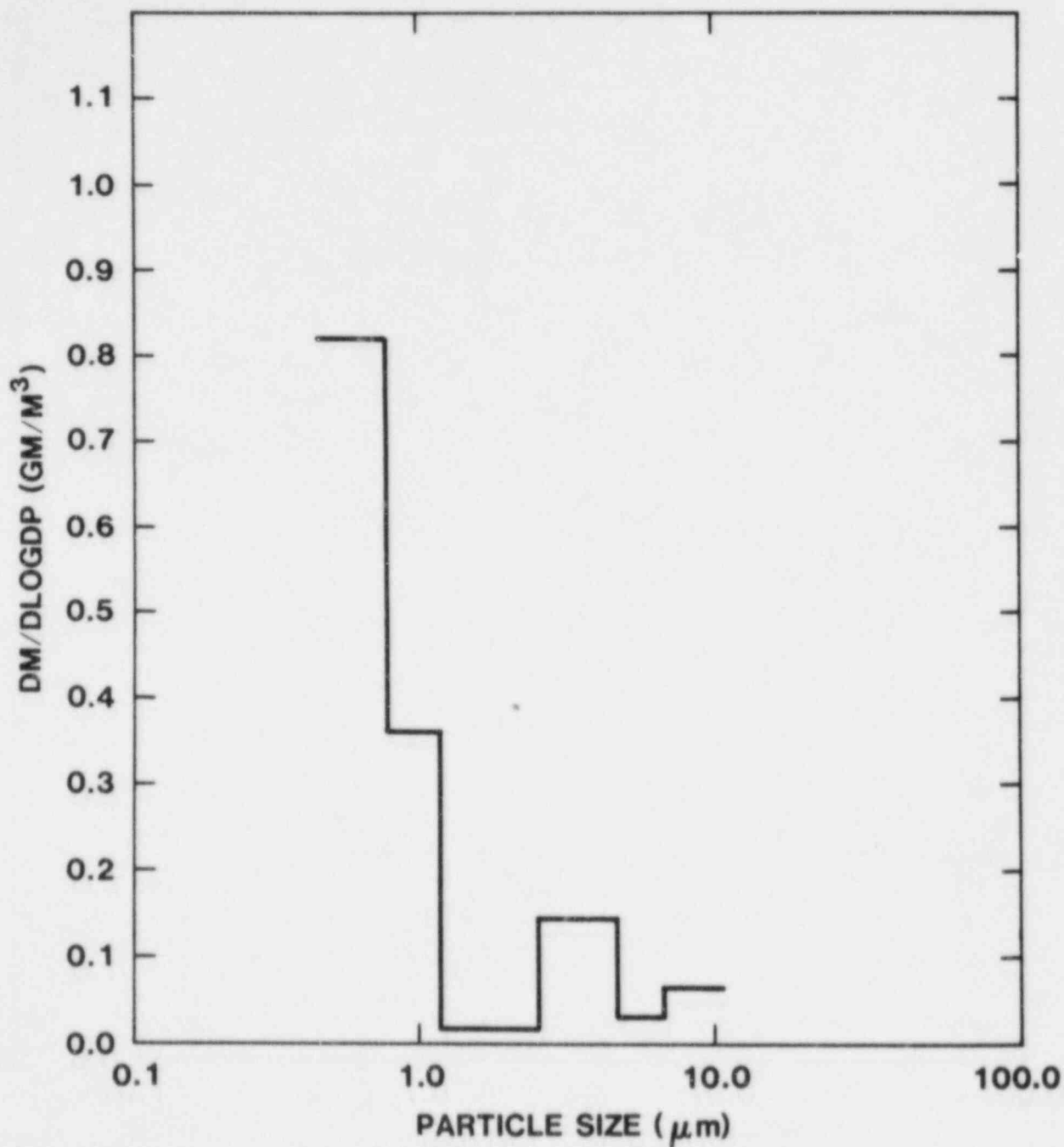


Figure IV.2a Sample Size Distribution
0.0 - 1.0 Min.

ANDERSON #2

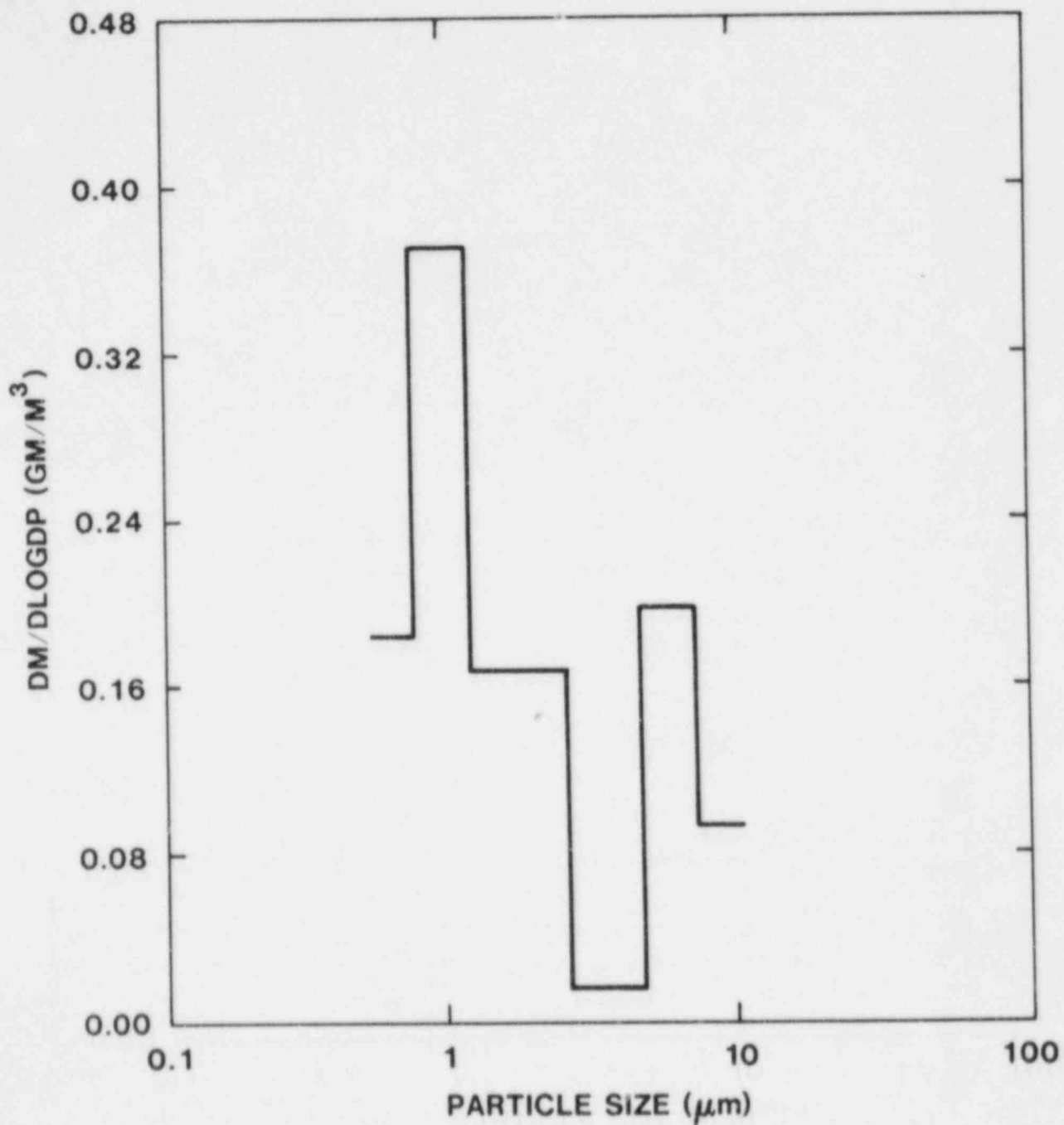


Figure IV.2b Sample Size Distribution
2.0 - 5.0 Min.

ANDERSON #3

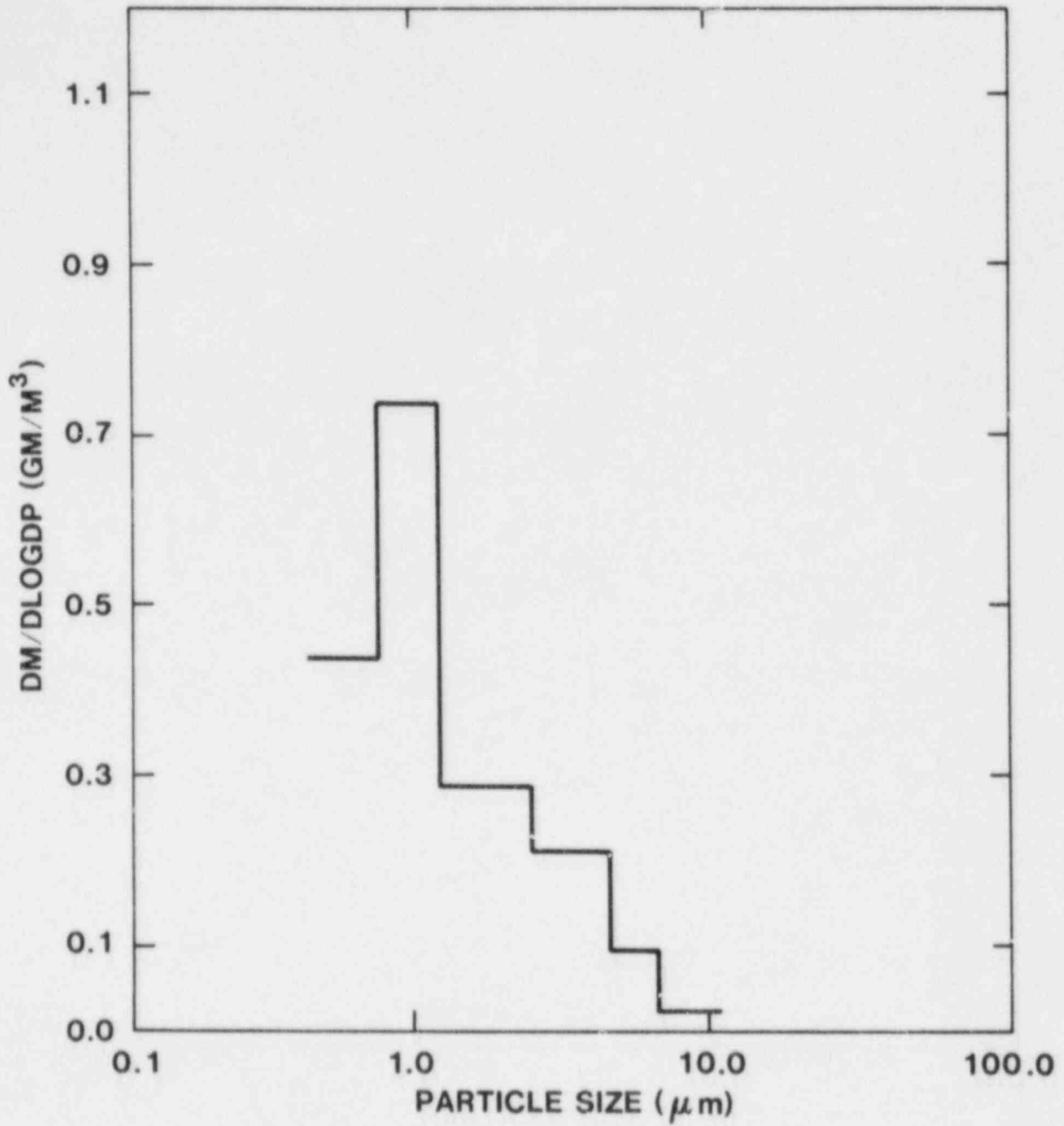


Figure IV.2c Sample Size Distribution
10.0 - 15.0 Min.

ANDERSON #4

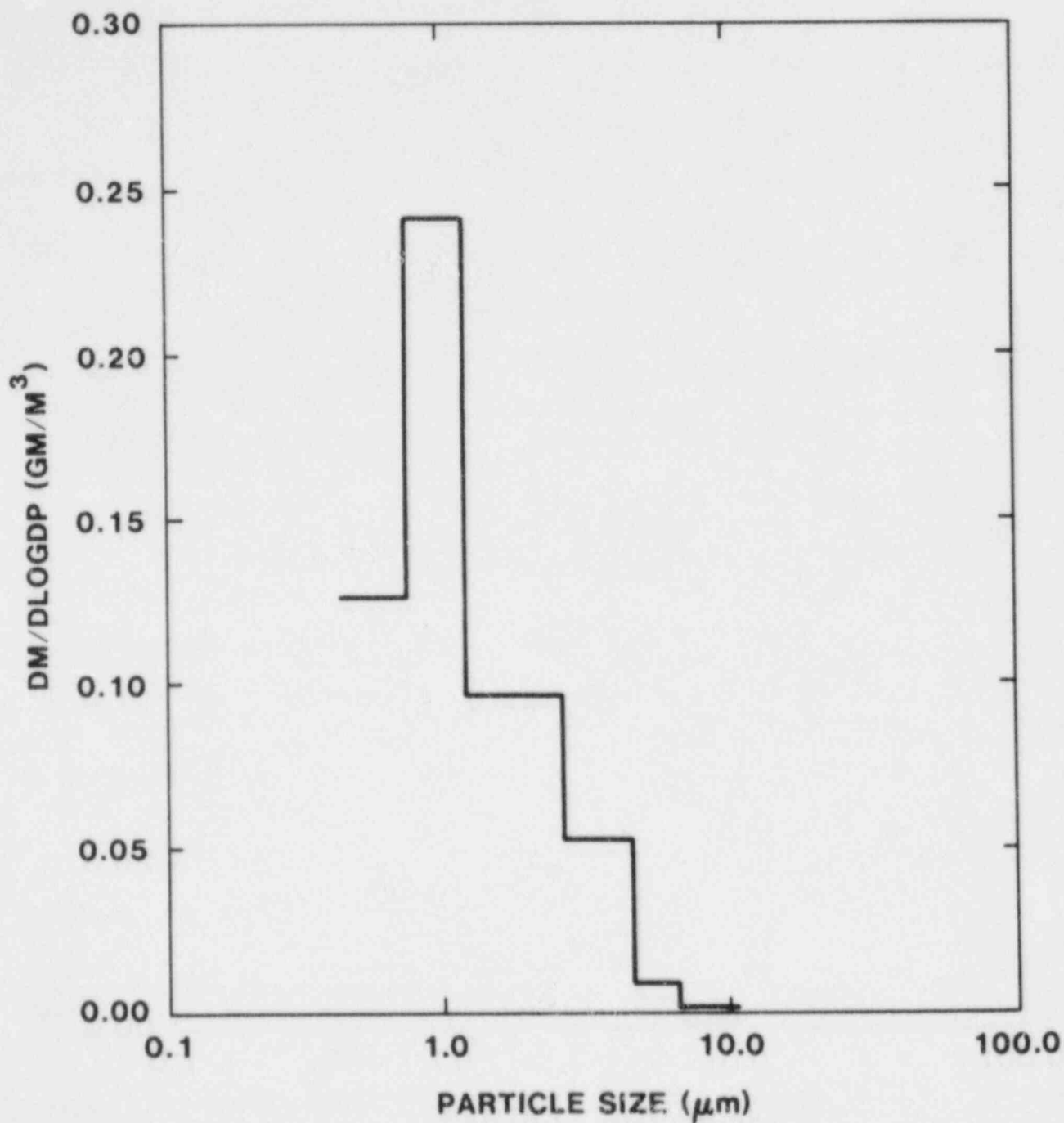


Figure IV.2d Sample Size Distribution
15.0 - 30.0 Min.

ANDERSON #1

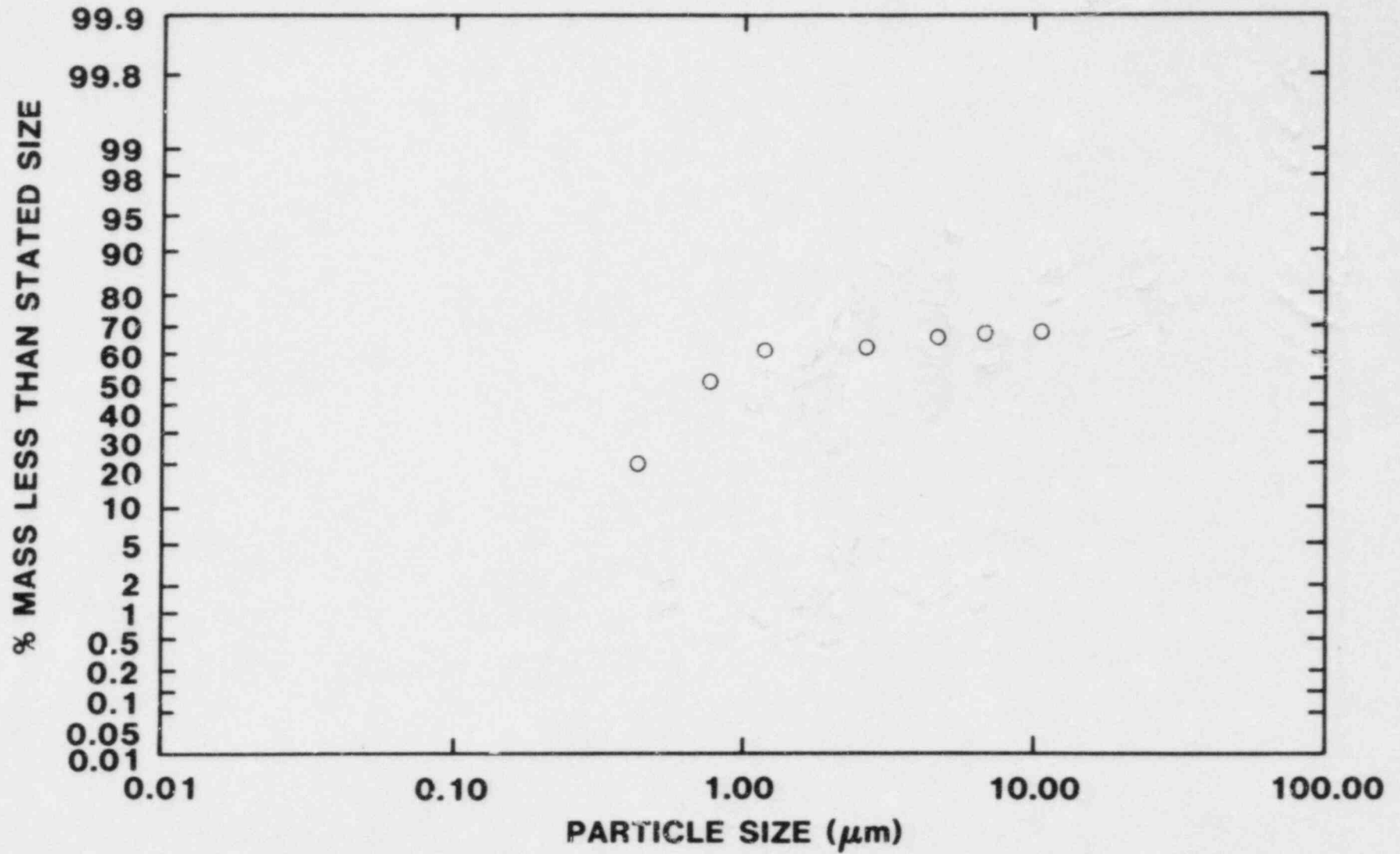


Figure IV.3a Sample Size Distribution (Accumulative),
0.0 - 1.0 Min.

ANDERSON #2

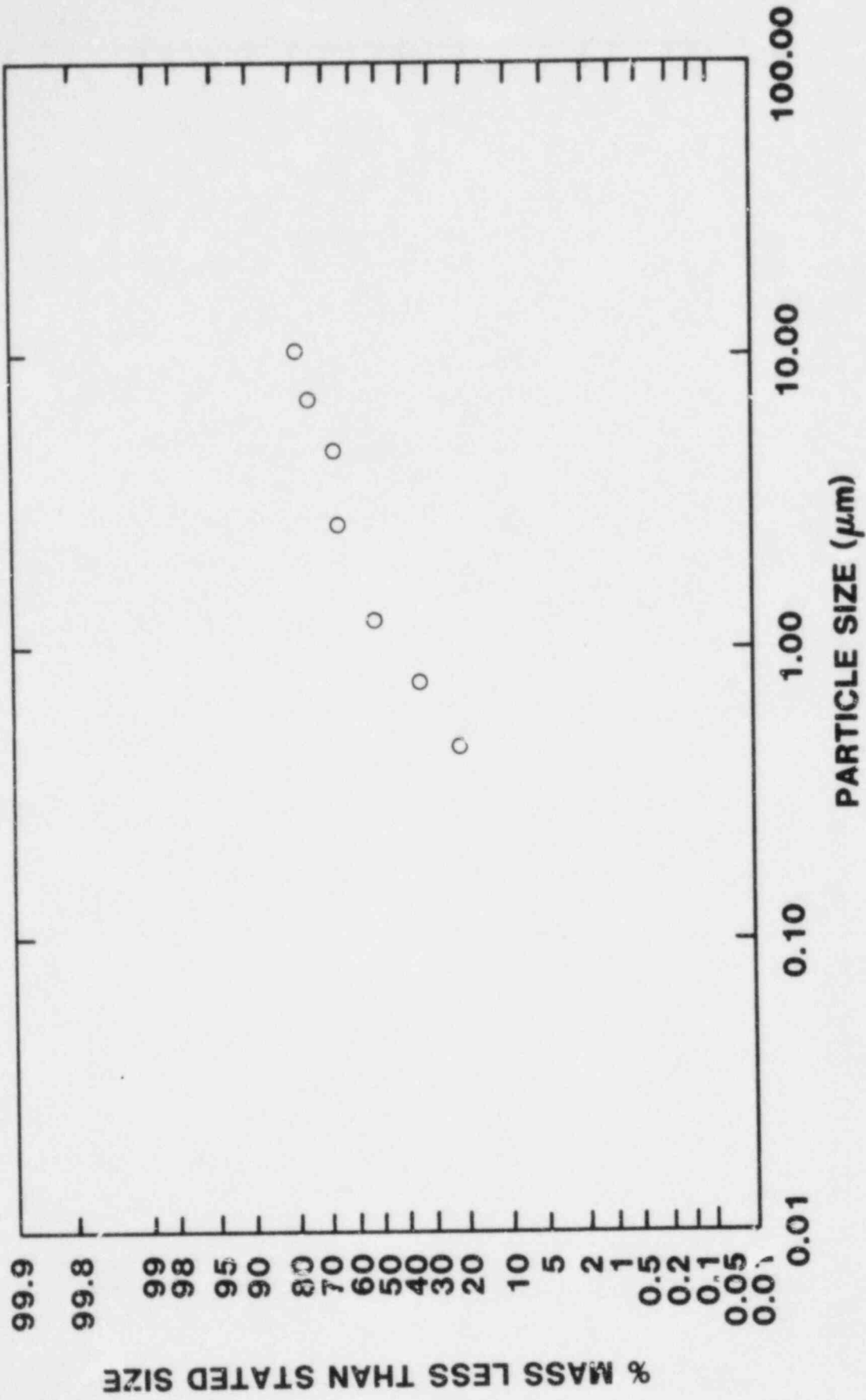


Figure IV.3b Sample Size Distribution (Accumulative),
2.0 - 5.0 Min.

ANDERSON #3

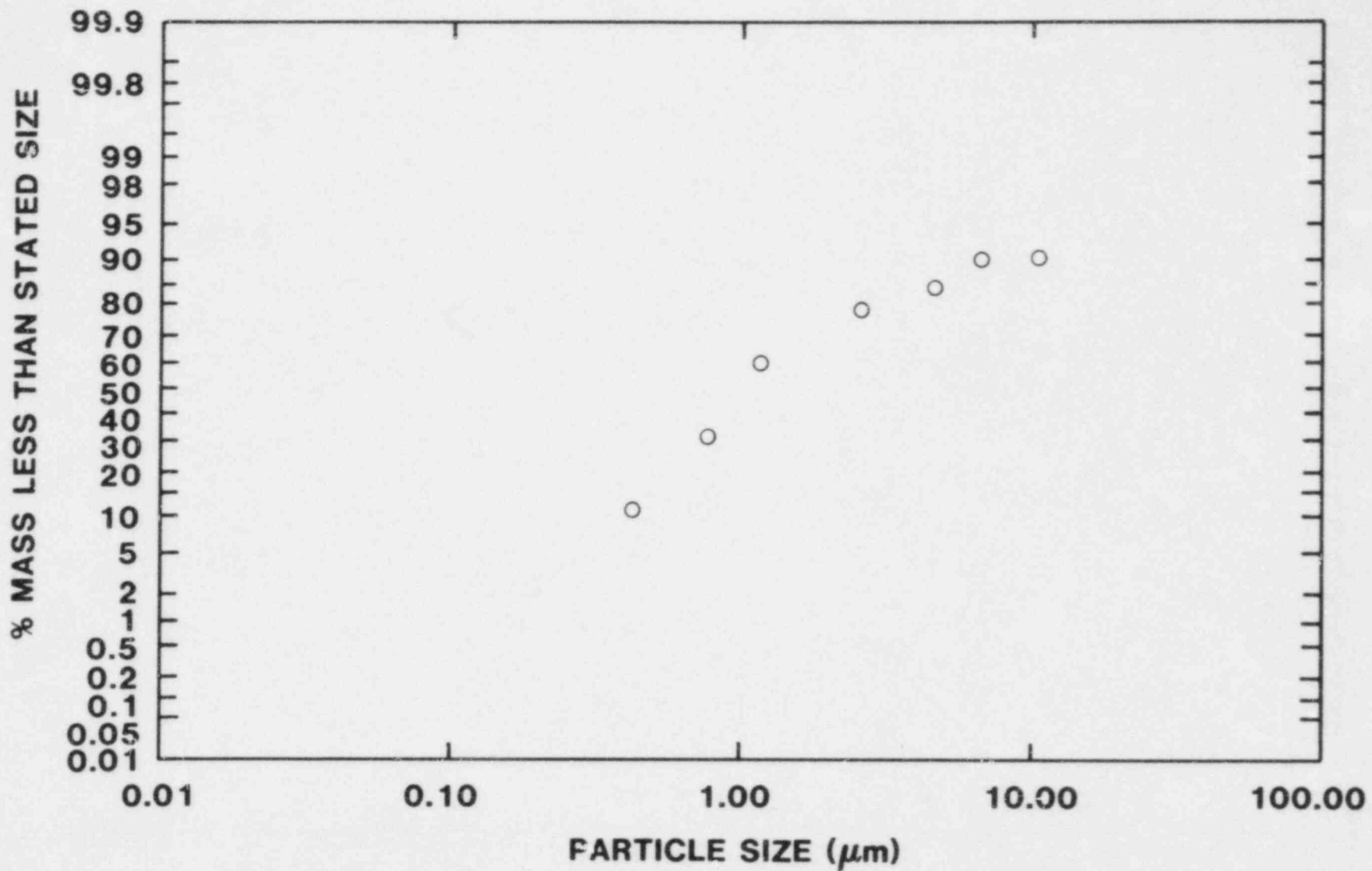


Figure IV.3c Sample Size Distribution (Accumulative),
10.0 - 15.0 Min.

ANDERSON #4

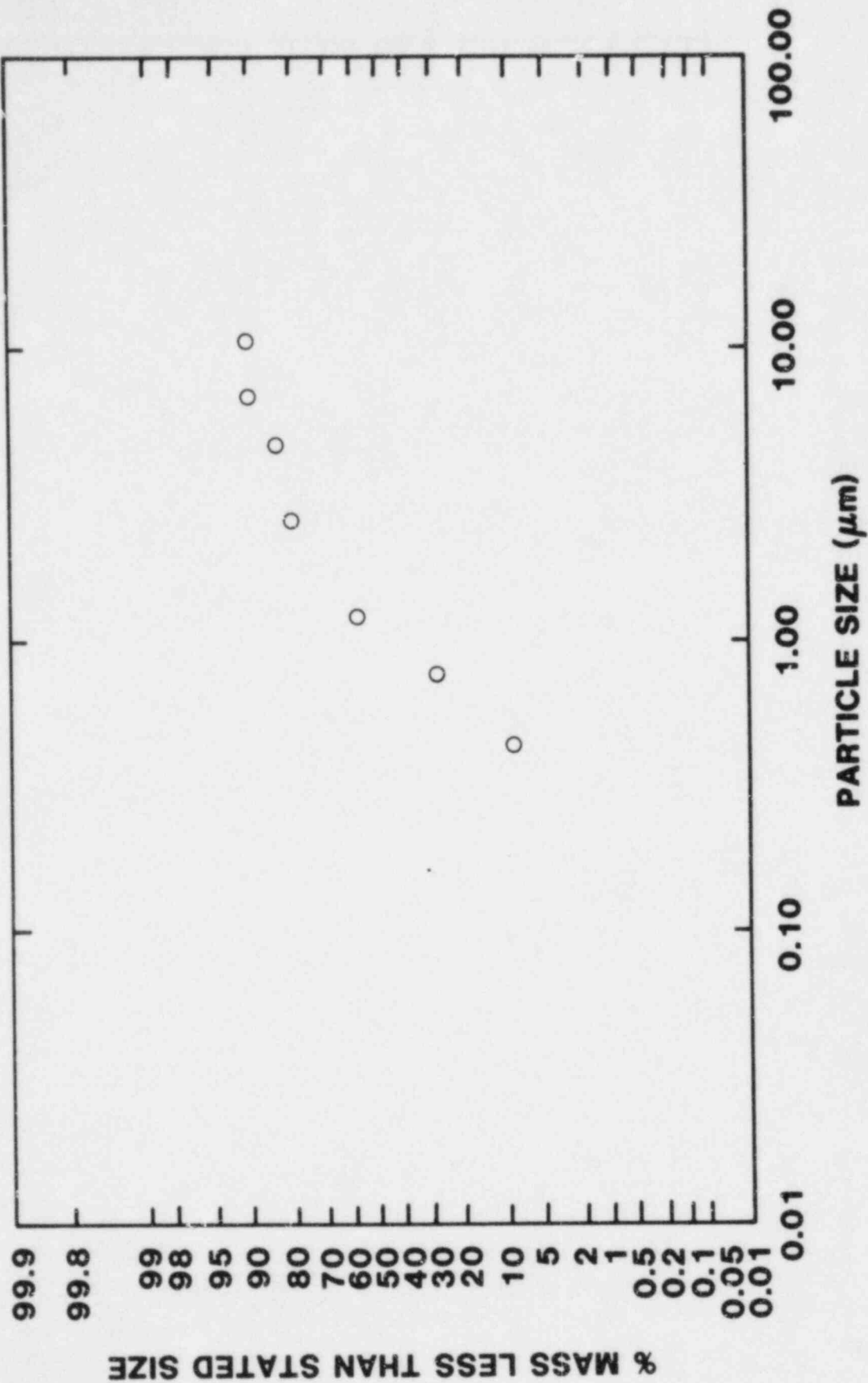


Figure IV.3d Sample Size Distribution (Accumulative),
15.0 - 30.0 Min.

FILTERS

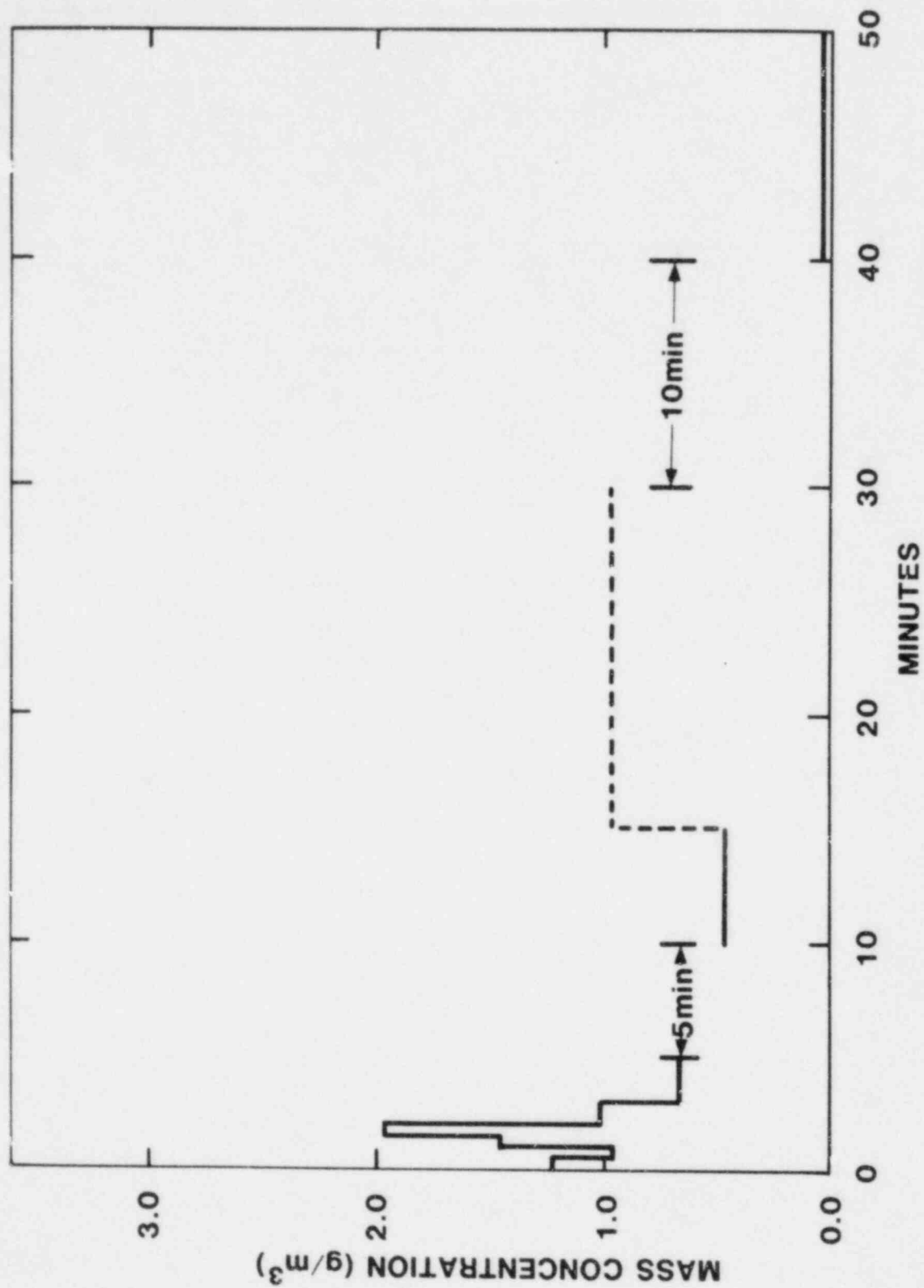


Figure IV.4 Concentration Versus Time, Filter Data

inhomogeneity in the aerosol concentration, leaks in the plumbing, sampling error, or handling error. These questions are being examined. Filter sample number 8 (15 to 30 minutes into the test) indicates an increase in concentration which is out of line with other samples. The filter is also heavily loaded. This may have been caused by either a leaky valve causing some sample to be drawn through the filter for the duration of the test, or valve number 8 being mistakenly switched on at some time prior to 15 minutes.

(4) Source Term Determination

The pour lasted a little over four minutes during which time the stream changed configuration and wandered. Splashing of melt was observed and material from the splashing was collected on the horizontal deposition surfaces. The pour varied from several small streams to two or three main streams. The filter sample data (Figure IV.4) indicate a strong source for two minutes then depletion of the suspended aerosol. The variation in concentration along with the material and aerosols produced by splashing made using of equation (II.1) difficult. An alternate approach has been used.

This approach uses the deposition samples to calculate the total mass aerosolized and divided the total aerosol mass by the four minutes taken for the pour to obtain an average rate.

Total aerosolized mass calculated from total deposition samples was 29 g giving a mass source of 0.12 g/sec for four minutes. The time resolved deposition samples yielded a figure of 51 g on the floor. This was calculated assuming a deposition rate of 4 mg/m²/sec for the time from 5 to 30 minutes (no data available due to equipment malfunction). This was higher than would be expected and consequently gives a high value for the figure. The floor deposition was multiplied by the ratio of total to floor deposition observed on the total deposition samples. This gave an estimate of 103 g for the total aerosolized mass which gives an estimated mass source of 0.43 g/sec for four minutes.

The filter data (Figure IV.4) suggests that the source was very low after two minutes. Alternate source terms are 0.28 g/sec for 105 seconds and 0.98 g/sec for 105 seconds.

(5) MAEROS Calculations

Two MAEROS calculations of aerosol behavior in the test chamber (see Table IV.2 for input conditions) have been performed and results are given in Figures IV.5a,b along with the measured results for mass concentration and deposition rate. Both calculations use a total generated mass of 29 g, and assume spherical particles of 5 g/cm³ density. Two mass source rates give the two calculations. One takes 240 seconds and the other 105 seconds to generate the 29 g of aerosol. The source size distribution is taken from the first cascade impactor sample. The three 500 cfm fans used to stir the chamber are assumed to be the source of the turbulent energy dissipation term. All kinetic energy input by the fans is assumed dissipated by turbulence.

TABLE IV.2
MAEROS CALCULATIONS

Assumes

Spherical particles $\chi = \gamma = 5$
Particle density = 5 g/cm^3

Mass Source = 0.12 g/sec for 4 minutes
 0.28 g/sec for 105 seconds

Mass Size Distribution of Source is Trimodal

D_{gme}	σ_g	% of mass source
.22 μm	1.4	61
1.3 μm	1.5	6
8.9 μm	2.0	33

Turbulent energy dissipation term $\sim 1 \text{ m}^2/\text{sec}^3$

Based on three 500 cfm fans

$$\epsilon = Q(1/2 \rho_g V^2) / (\rho_g \text{ vol})$$

where

Q = total volume flow

V = velocity of gas through fan

ρ_g = density of gas

vol = chamber volume

This assumes that kinetic energy imparted to gas by fans is totally dissipated by turbulence in chamber.

Temperature gradient to walls = 10^4 K/M

Gas Temp - used in-chamber Thermocouple data

Gas Pressure - used in chamber pressure transducer 670 mmHz

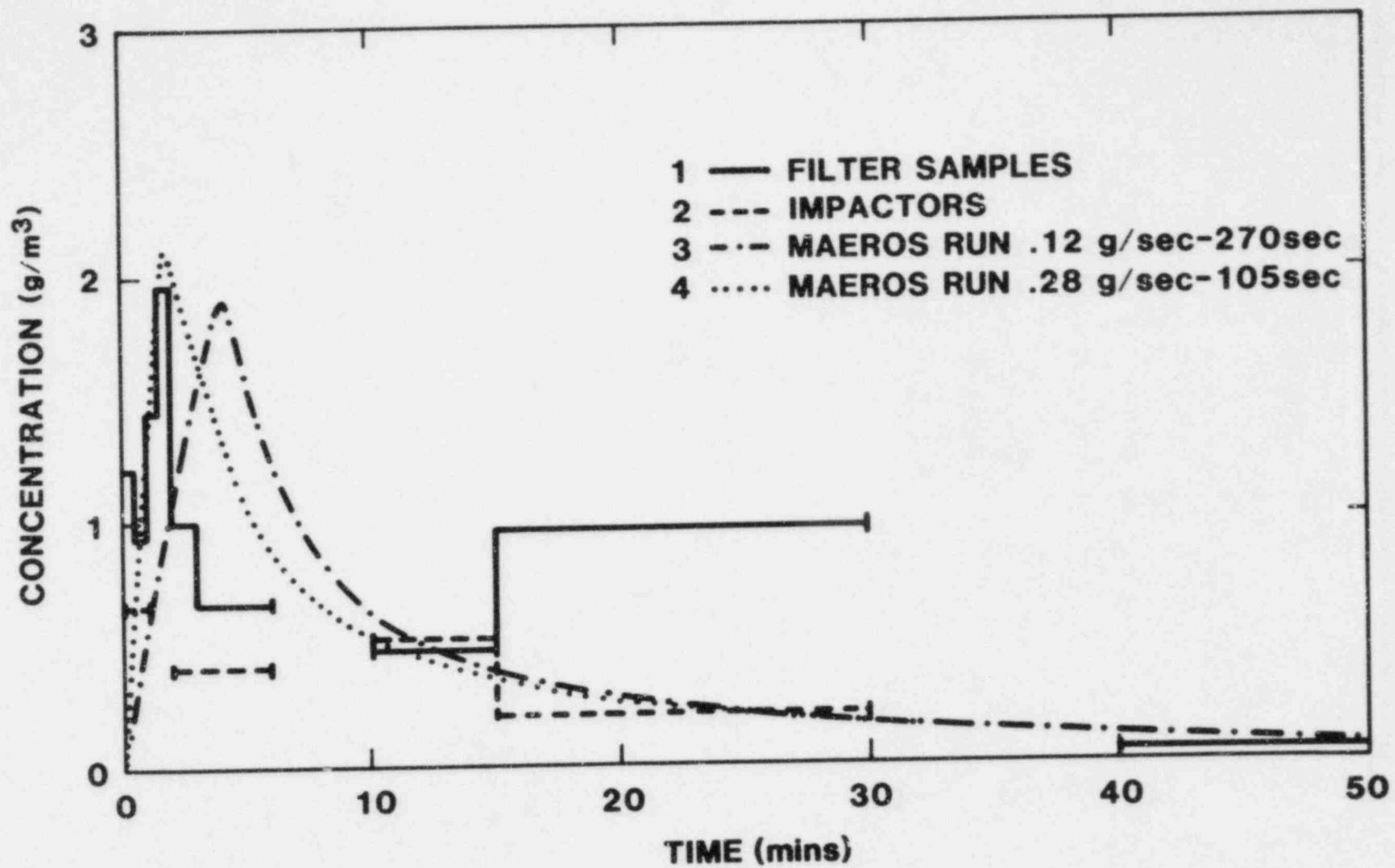


Figure IV.5a Concentration Versus Time

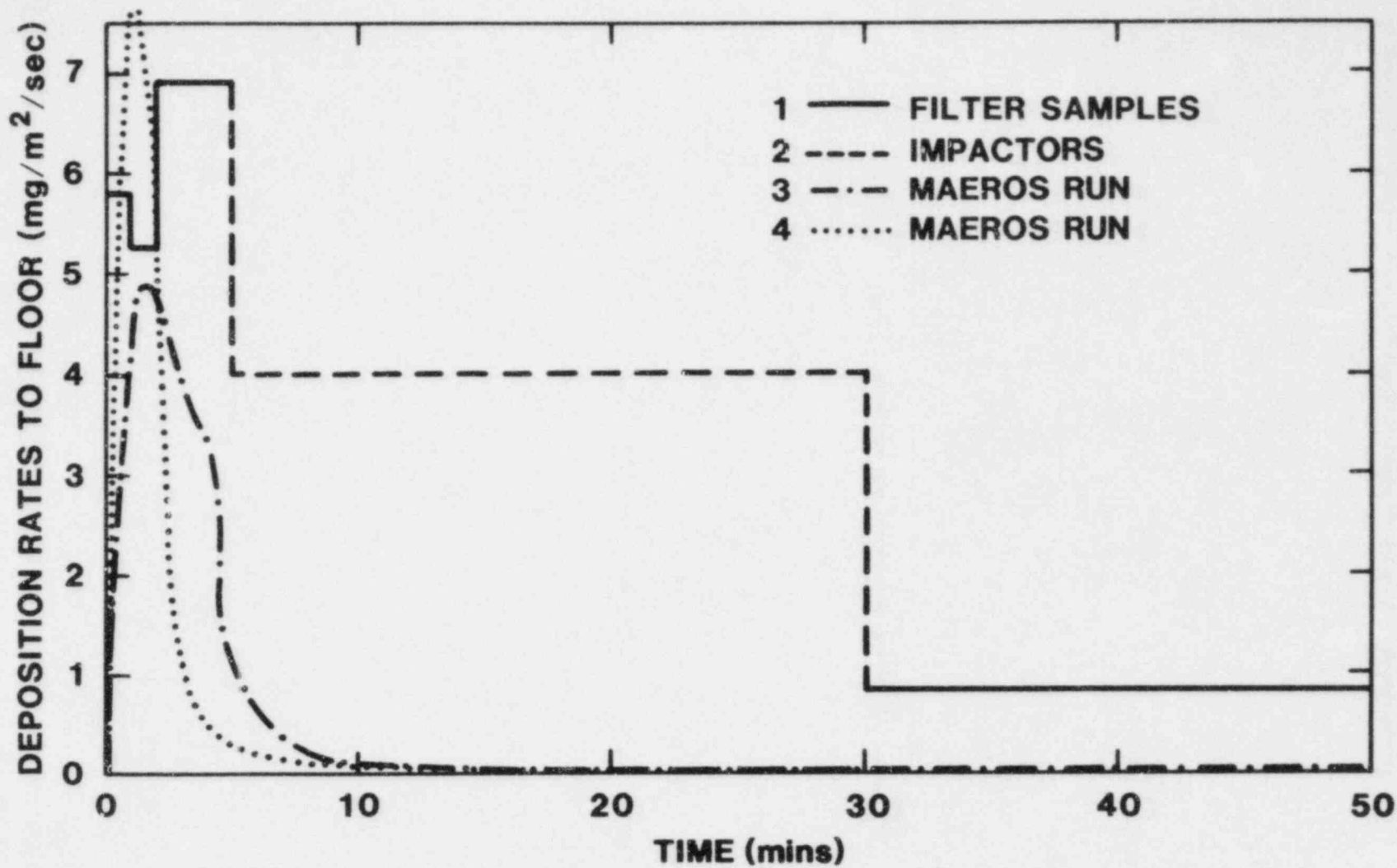


Figure IV.5b Deposition Rate versus Time

Note that while the calculations do not match the data exactly, they show the same general trends. By adjusting input parameters a closer match could be obtained.

b. Gas Data

The gas samples collected were analyzed using a Hewlett-Packard Model 5836 Gas Chromatograph. Samples were injected directly from grab sample bottles into a Porapak Q, 80/100 mesh column which was time-temperature programmed from 223 K to 473 K (-50°C to 200°C). The porous polymer beads in the column provide sharp symmetrical peaks and low retention volumes for polar materials such as water, alcohols, acids and glycols. The use of time-temperature programming allows for the separation of the gases according to their respective molecular weight. This allows identification more readily as a function of elution-retention times.

Detection was accomplished by using a thermal conductivity detector which was finely tuned to the primary standard gas mixture made up of the following constituents: H₂, N₂, Ar, CO, CH₄, CO₂, C₂H₄, C₂H₆, O₂, and H₂O. Only peaks that were assigned to the calibration standard were detected.

The results of gas sampling are tabulated in Table IV.3 and plotted in Figures IV.6 to IV.11:

- Figure IV.6 Volume Percent of N₂ and O₂
- Figure IV.7 Volume Percent of CO₂
- Figure IV.8 Volume Percent of CO
- Figure IV.9 Volume Percent of Ar
- Figure IV.10 O₂/N₂ Ratio
- Figure IV.11 O₂/CO₂ Ratio.

It appeared that initially the test chamber atmosphere was a mixture of air and argon with minor amounts of CO and CO₂. With time oxygen reacted with the carbon and graphite components of the furnace and produced CO₂. No hydrogen generation was detected as a result of the possible reaction of the melt with water in the magnesia bricks.

c. Temperature Data

The thermal response of the magnesia crucible was measured by embedded thermocouples from 1/8 in. to 6 in. below the surface. The data acquisition system was not turned on until 3.17 minutes into the melt pour. Therefore, the early time data were lost.

In general, the central portion of the bottom of the crucible was heated more than the edge of the bottom. This is illustrated in Figure IV.11 where temperature responses at 1/2 in. from the surface for a spot 1.75 in. from the center of the crucible and a spot 5.5 in. from the center of the crucible are compared. One reached 863 K (590°C), the other only 598 K (325°C). Figures IV.12 and IV.13 show the thermal response of the bricks at various depths as a function of time. The highest recorded temperature was 973 K (700°C) at 1/8 in.

TABLE IV.3 Gas Generation Data

Result of Analysis (a)

Sample Time, SECS	Sample I.D.	Sample Duration, SECS	Press, Torr	Volume Percent				
				N ₂	O ₂	Ar	CO	CO ₂
34.5	V5-1	5.25	423	35.766	7.230	55.502	1.119	0.383
39.8	V5-2	11.25	453	35.921	8.221	54.538	1.032	0.288
51.0	V5-3	13.88	471	48.022	12.687	38.417	0.705	0.168
64.9	V5-4	22.88	458	40.402	9.200	49.127	0.879	0.392
87.8	V4-2	28.13	460	34.831	3.769	59.646	0.766	0.977
115.9	V4-3	29.70	459	34.987	3.078	60.546	tr ^(b)	1.390
145.6	V4-4	29.78	484	42.279	5.427	50.997	tr	1.297
175.4	V3-2	31.65	457	40.042	4.748	53.699	tr	1.511
207.0	V3-3	31.95	457	33.627	2.817	61.236	0.627	1.692
239.0	V3-4	40.20	453	35.340	2.633	59.457	0.806	1.764
279.0	V2-2	106.65	459	35.265	2.487	59.399	0.957	1.892
385.8	V2-3	59.93	459	35.142	2.021	60.009	1.003	1.825
445.7	V2-4	34.28	459	33.478	1.982	61.721	0.912	1.907

Note: (a) Plots and Bar Graphs included in Appendix

(b) tr = trace

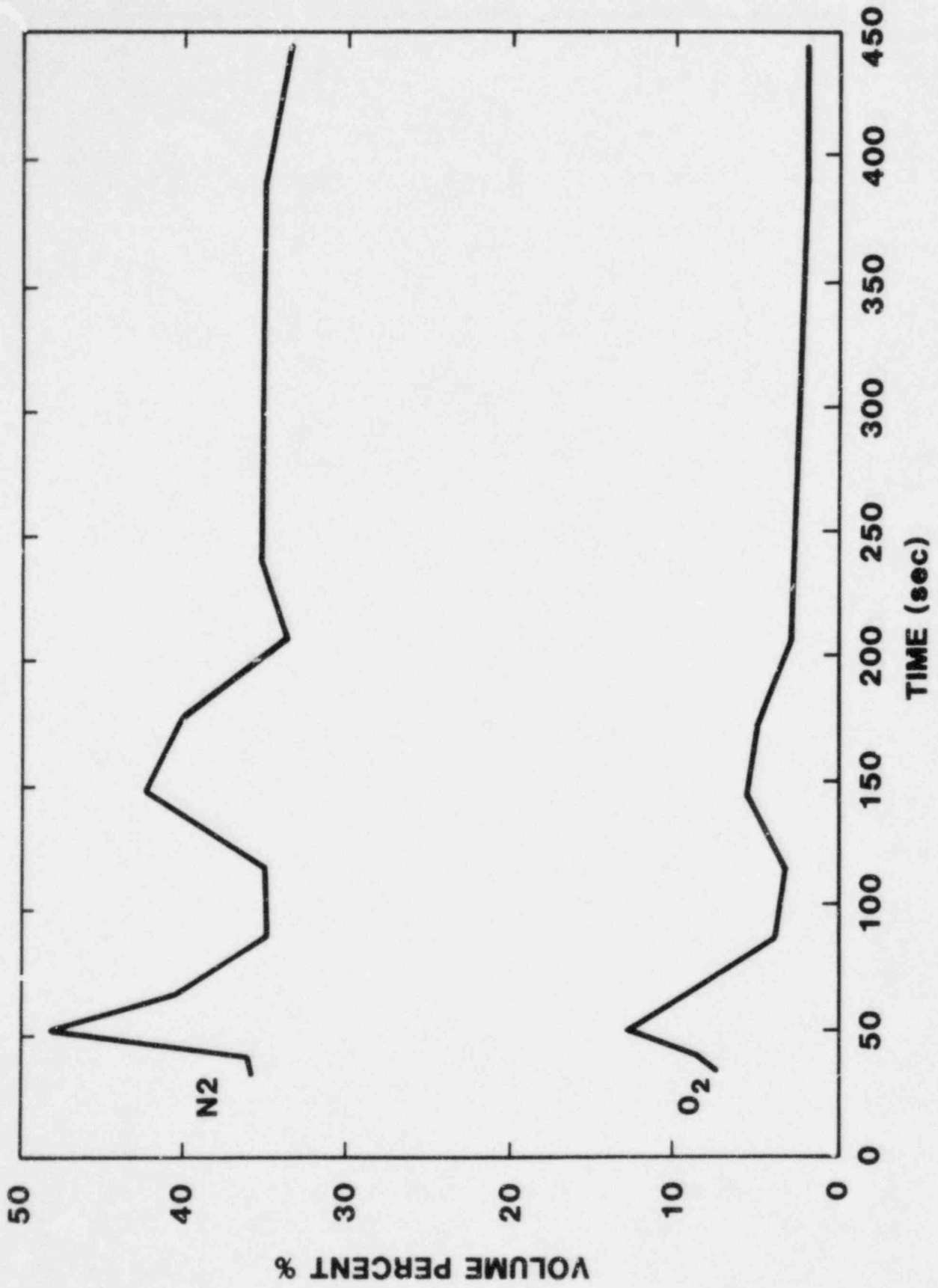


Figure IV.6 N₂ and O₂ Volume Percent Versus Time

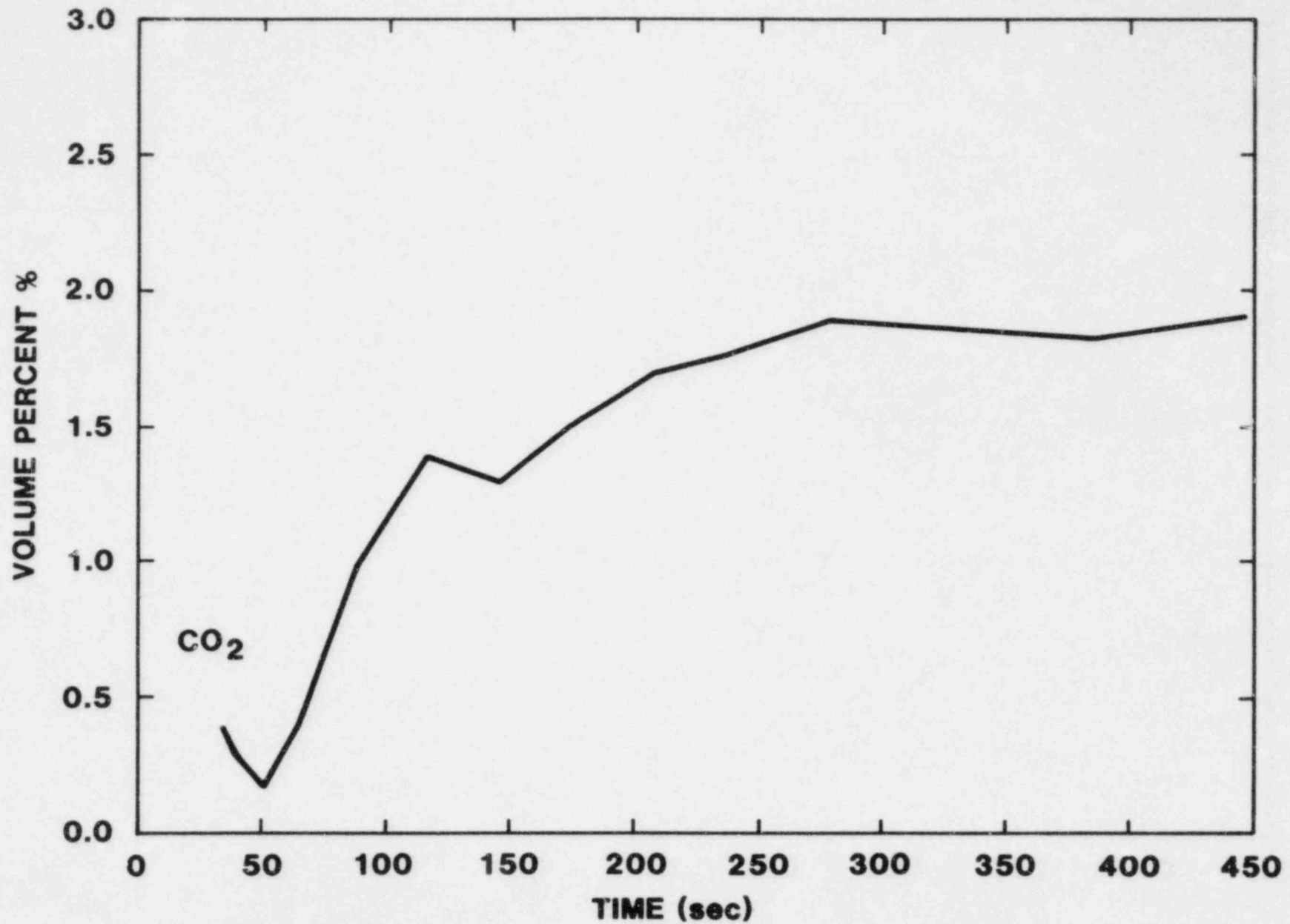


Figure IV.7 CO₂ Volume Percent Versus Time

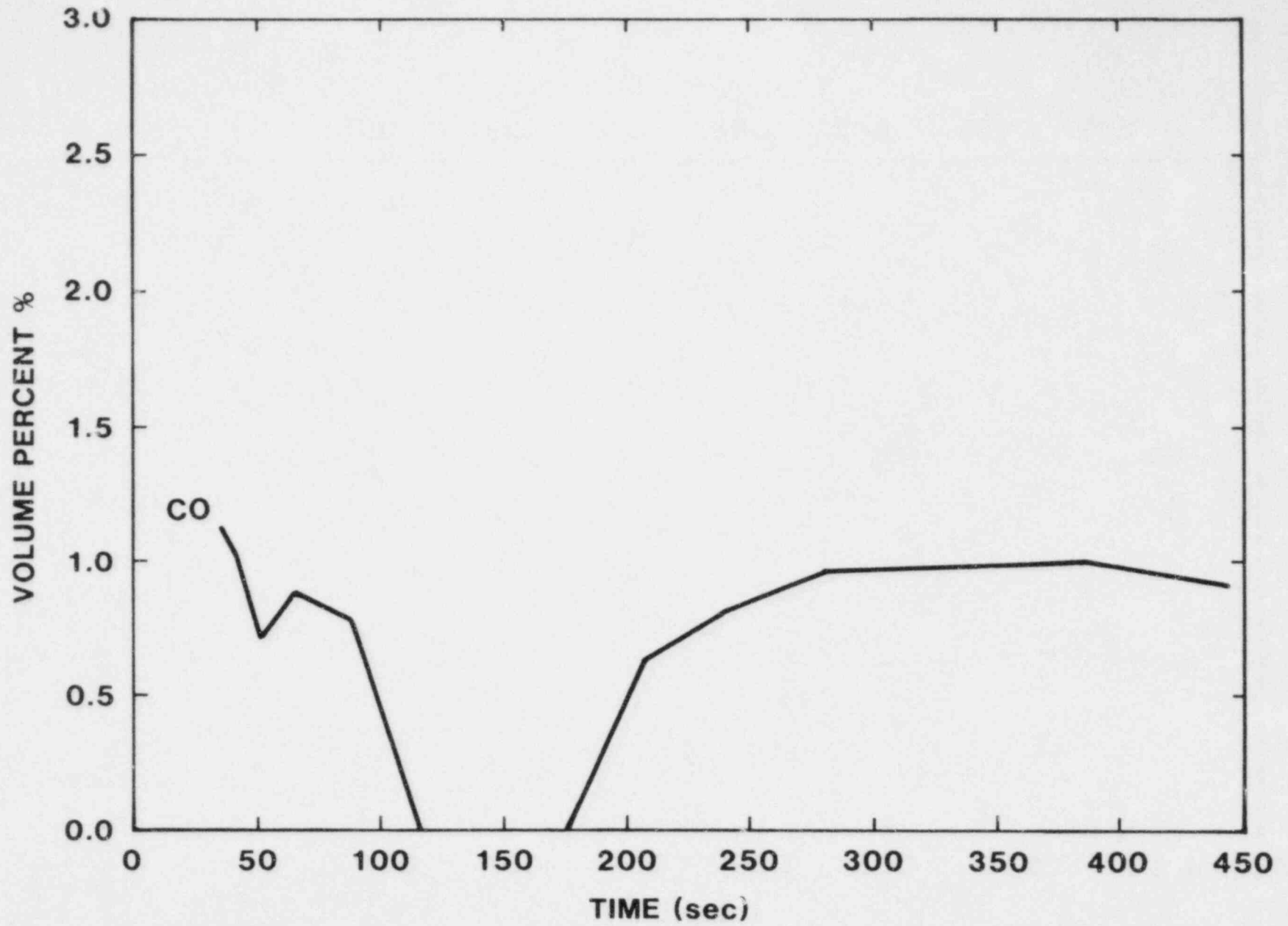


Figure IV.8 CO Volume Percent versus Time

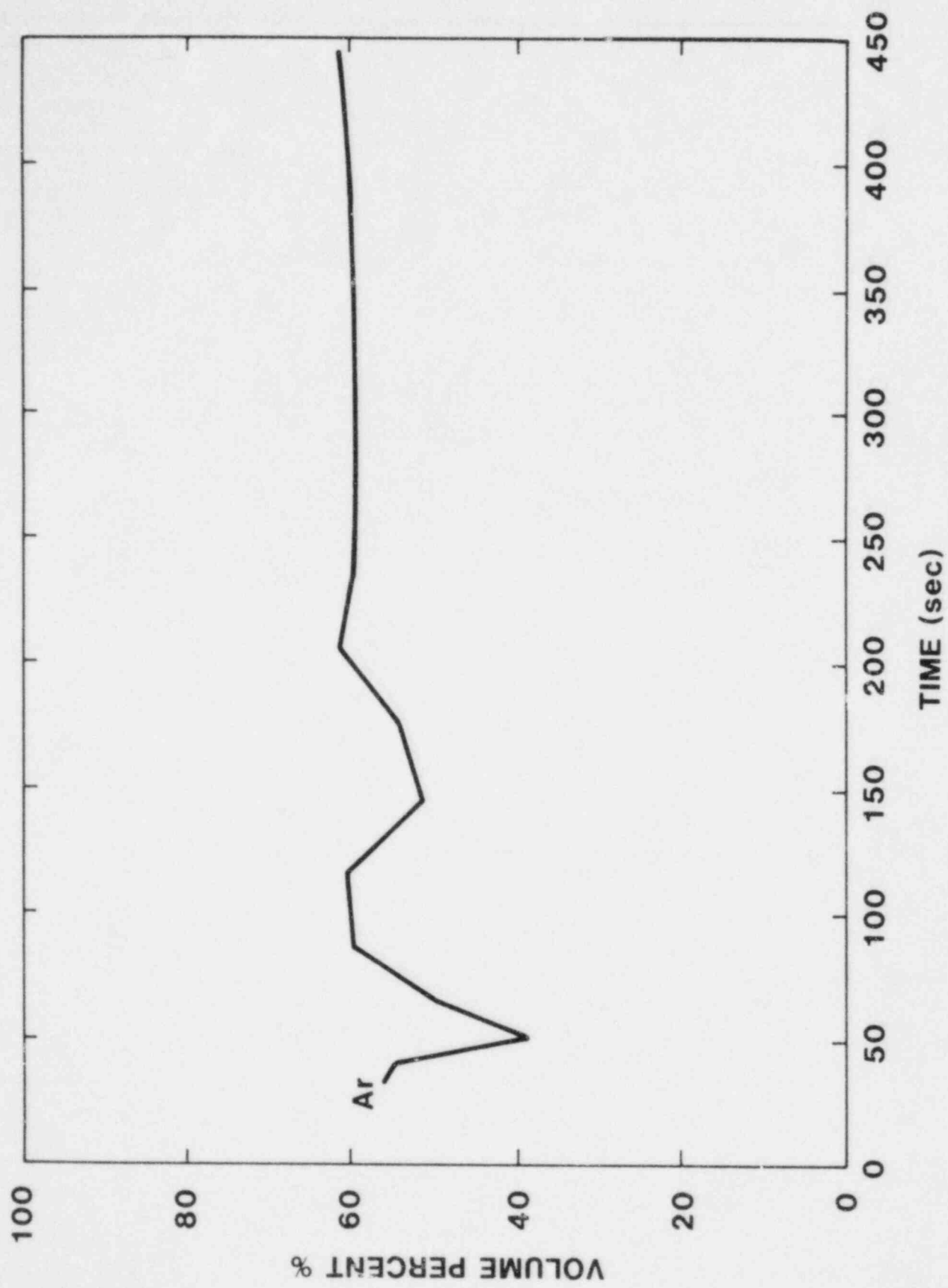


Figure IV.9 Ar Volume Percent Versus Time

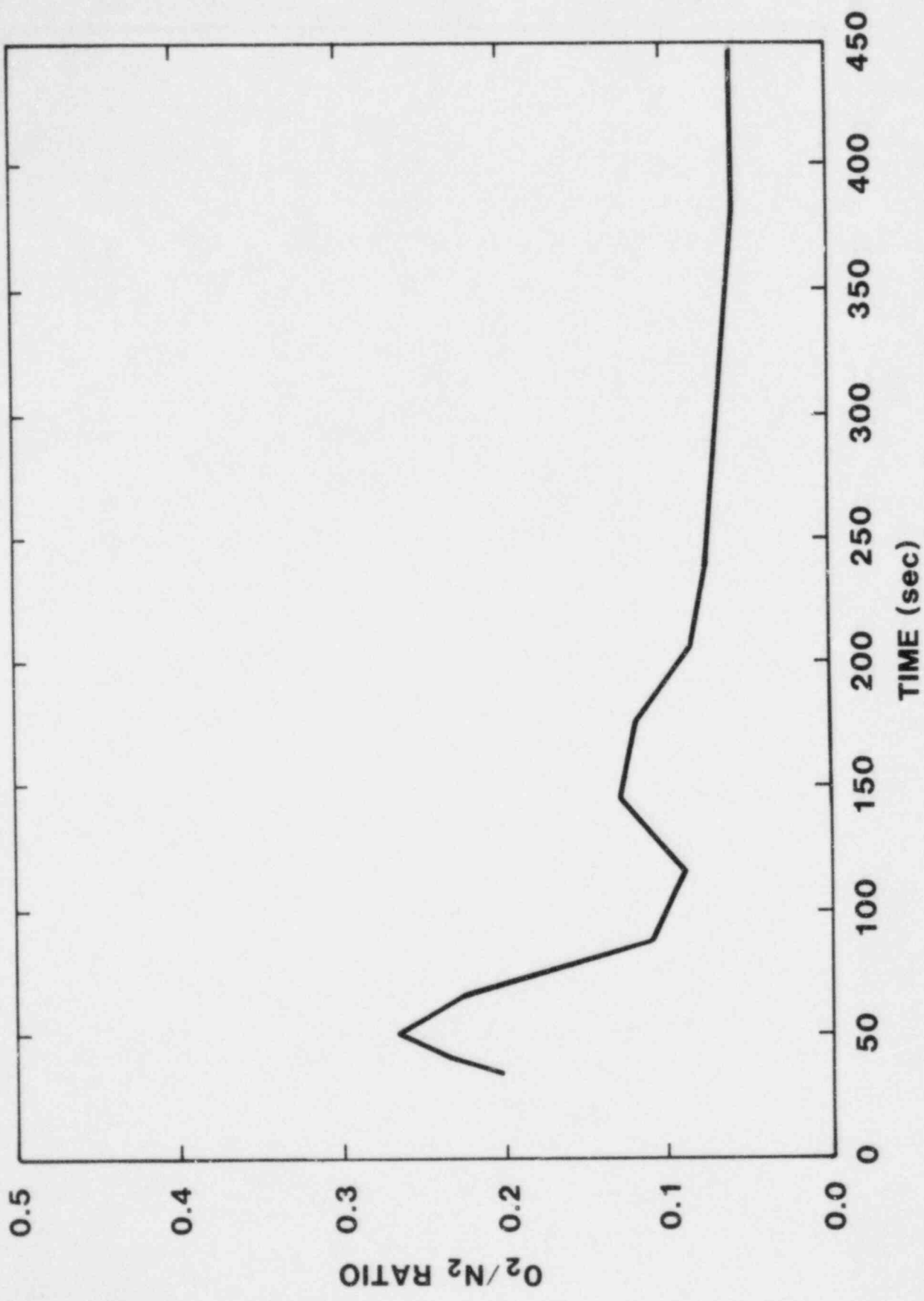


Figure IV.10a O_2/N_2 Ratio Versus Time

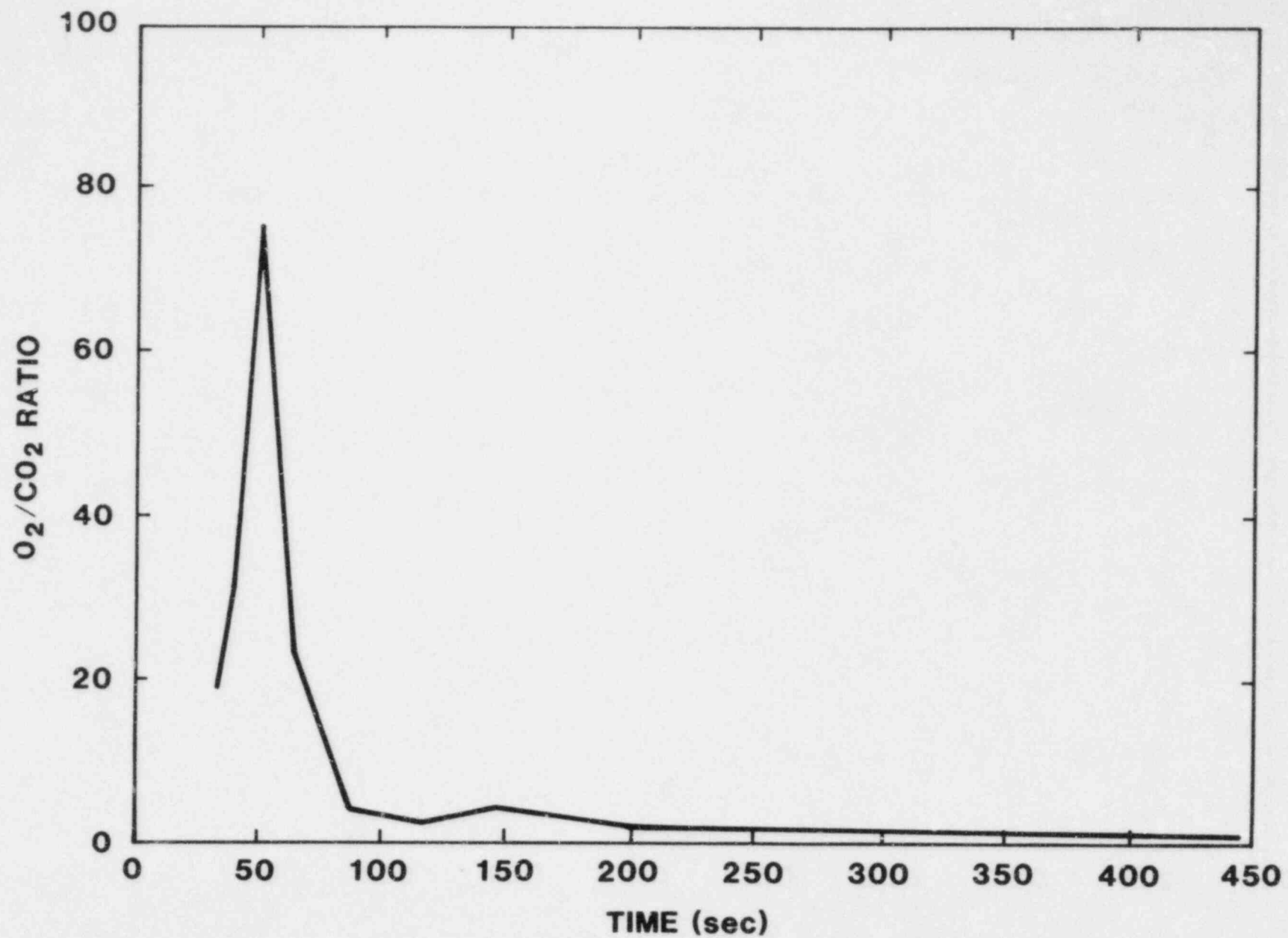


Figure IV.10b O₂/CO₂ Ratio Versus Time

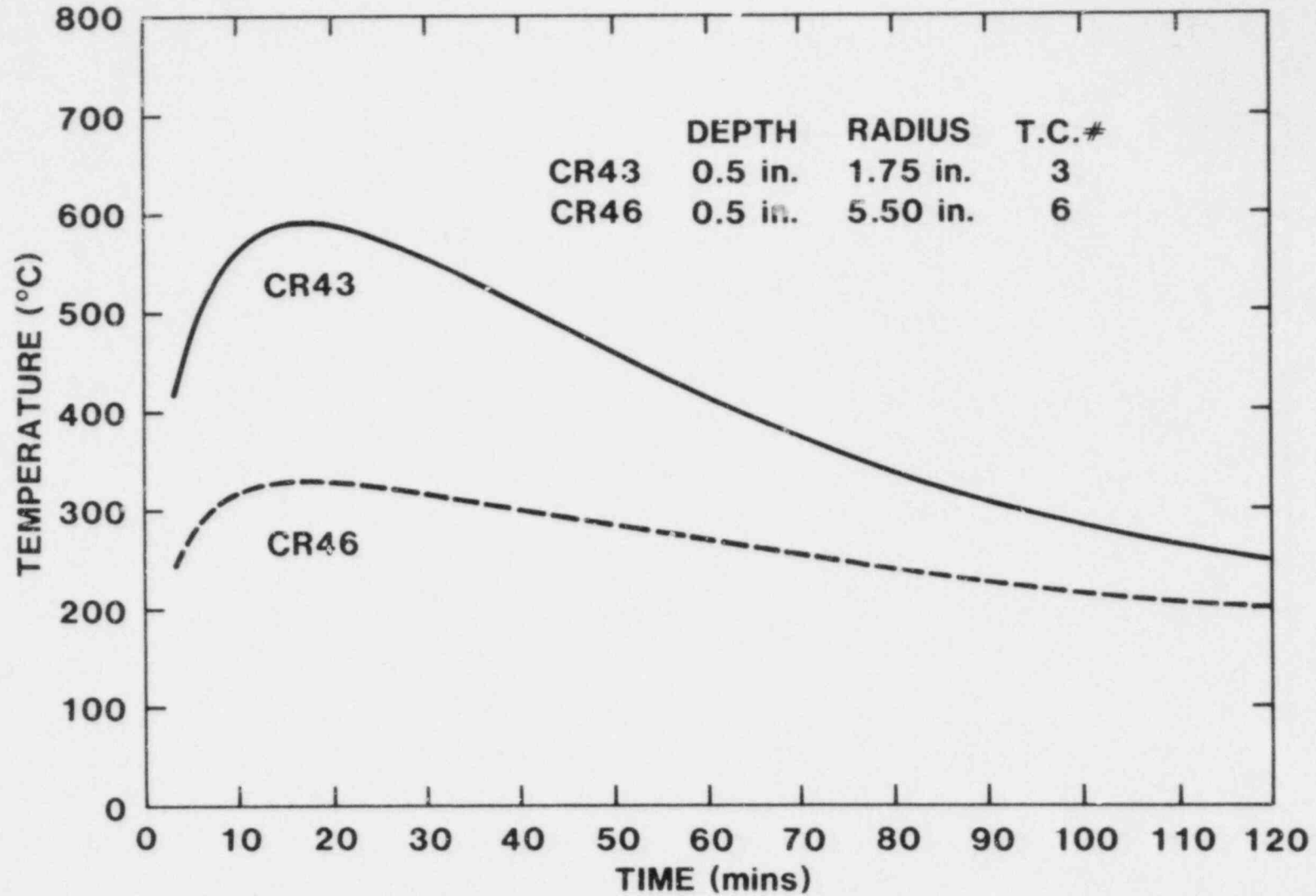


Figure IV.11 Temperature Responses on the Bottom of the Crucible, 1/2 in. Below the Surface 1.75 in. and 5.5 in. from Center of Crucible

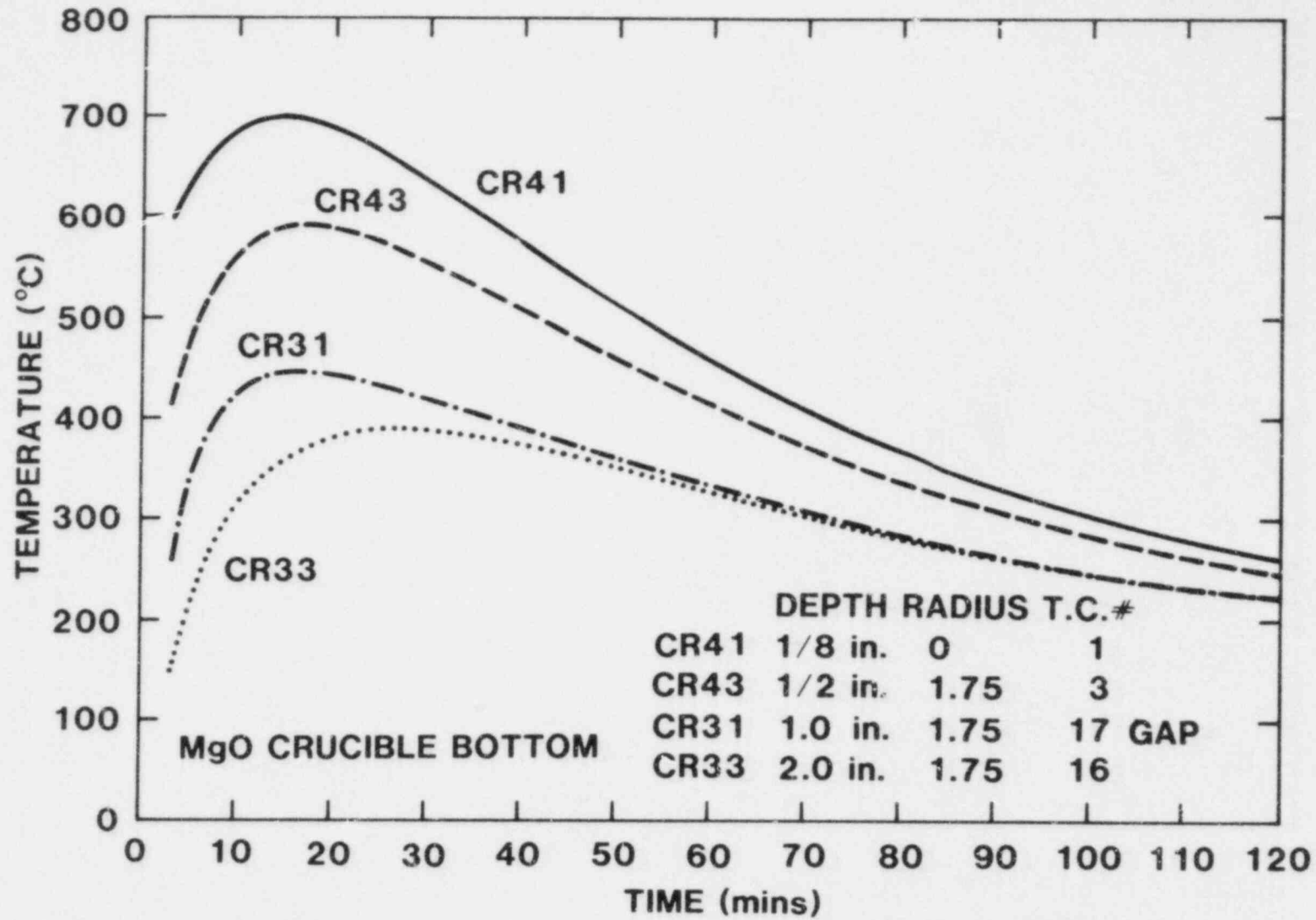


Figure IV.12 Thermal Responses in the Bottom of the Crucible

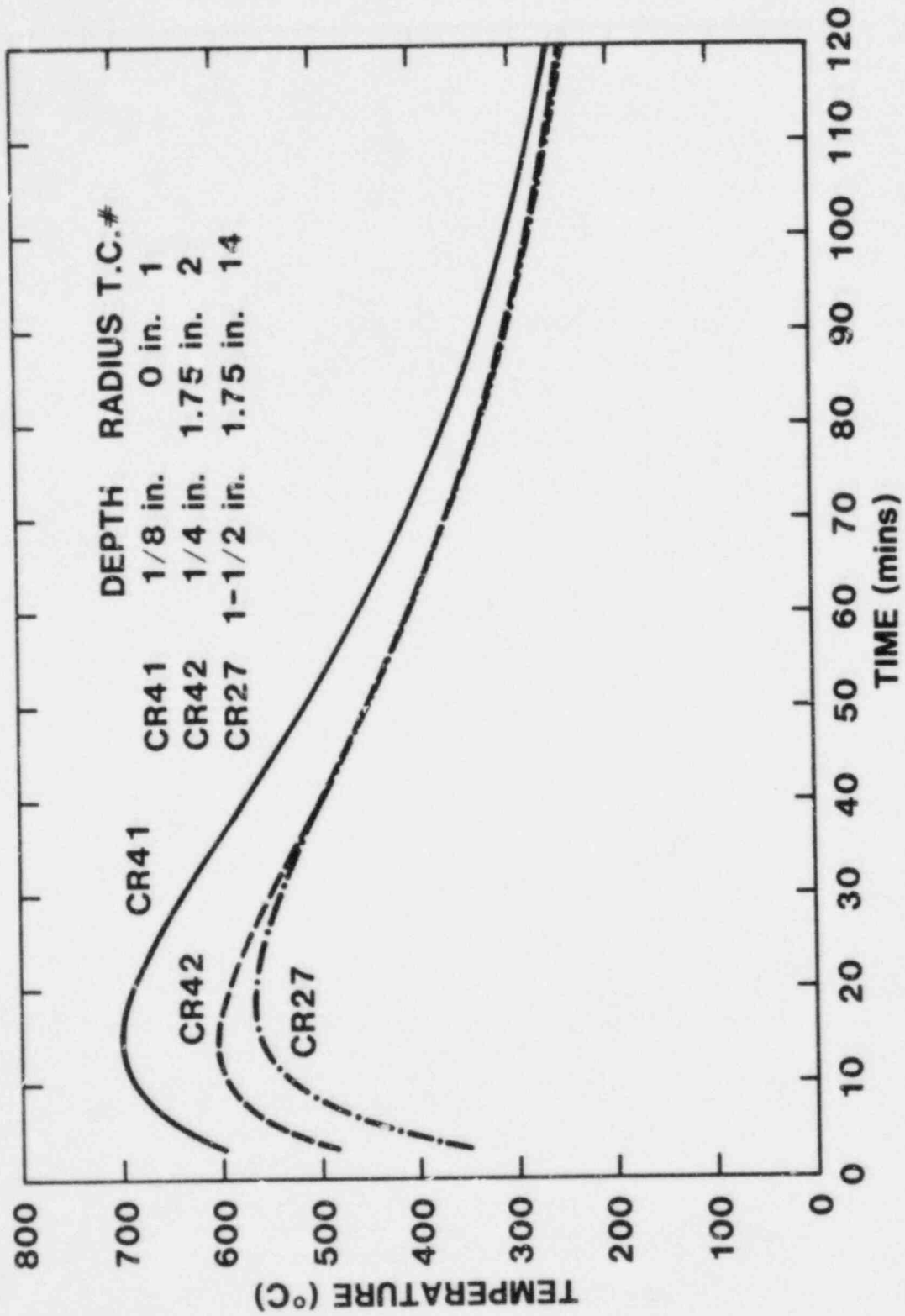


Figure IV.13 Thermal Responses in the Bottom of the Crucible

below the surface, at the center of the crucible. Work is currently underway to use an inverse conduction code to infer the surface flux.

Two thermocouples were installed in cracks between bricks to detect crack penetration, one at 1 in. deep and one at 2 1/2 in. deep, both 3 1/2 in. from the center of the crucible. The thermal responses, Figure IV.14, are quite similar to those in the brick. There is no sharp increase of temperature indicative of gap penetration, at least not to a depth of one inch.

The bricks on the sidewall were heated less than the bottom. A total of six bricks were instrumented in the pool region. The temperature histories in each brick are shown in Figures IV.15 to IV.20. Bricks 1, 4, 7 were neighboring bricks and 13, 16, 19 were opposite 1, 4, 7 (see Figure II.17a for brick locations). Obviously the temperature histories of opposing bricks are not the same. There are two probable reasons: (1) the melt stream was not stationary and for long periods of times off-center, and (2) at least part of the melt did not have much superheat; rather than flowing into a pool the melt simply solidified near the site of impingement.

d. The Upward Heat Flux

The upward heat flux from the melt pool was estimated using four methods: (1) the bottom of the instrumentation shield as a slug gauge, (2) a nickel slug gauge, (3) a thin foil heat flux gauge and (4) a teflon ablation gauge, see Figure IV.21. The vertical distance between the melt surface and the gauge was about 13 in. The data from the first two gauges have been reduced.

Since the instrumentation boom could not be moved over the pool until the end of the melt pour, upward heat flux data was only available five minutes after tapping. The data from the nickel slug gauge, Figure IV.22 show an incoming flux level of about 32 Btu/ft² sec (36 W/cm²) at five minutes and dropped to a quarter of that value three minutes later. The heat shield data, Figure IV.23, shows a flux into the shield of 7.5 Btu/ft² sec (8.5 W/cm²). The two values are different because the nickel gauge was calibrated for incoming flux values whereas the shield simply gives the amount of energy into the shield. The two values should differ by a factor equal to the emissivity of the Al₂O₃ coating on the shield. The emissivity of Al₂O₃ is estimated to be 0.24; therefore, the incoming flux corresponding to 7.5 Btu/ft² sec (8.5 W/cm²) is 31 Btu/ft² sec (35 W/cm²). This is consistent with the value of 32 Btu/ft² sec (36 W/cm²) given by the nickel flux gauge.

e. Brick Cracking Data

Nonuniform heating of a structural shape can induce stress into the material by two distinct mechanisms. The first is a stress gradient that is caused by nonuniform thermal expansion of the structure. This behavior can cause a failure (crack) along a line where the shear stress exceeds the ultimate strength. The second type of stress pattern is caused by the expansion of material against an external constraint. This is represented as a zero-volume expansion that results

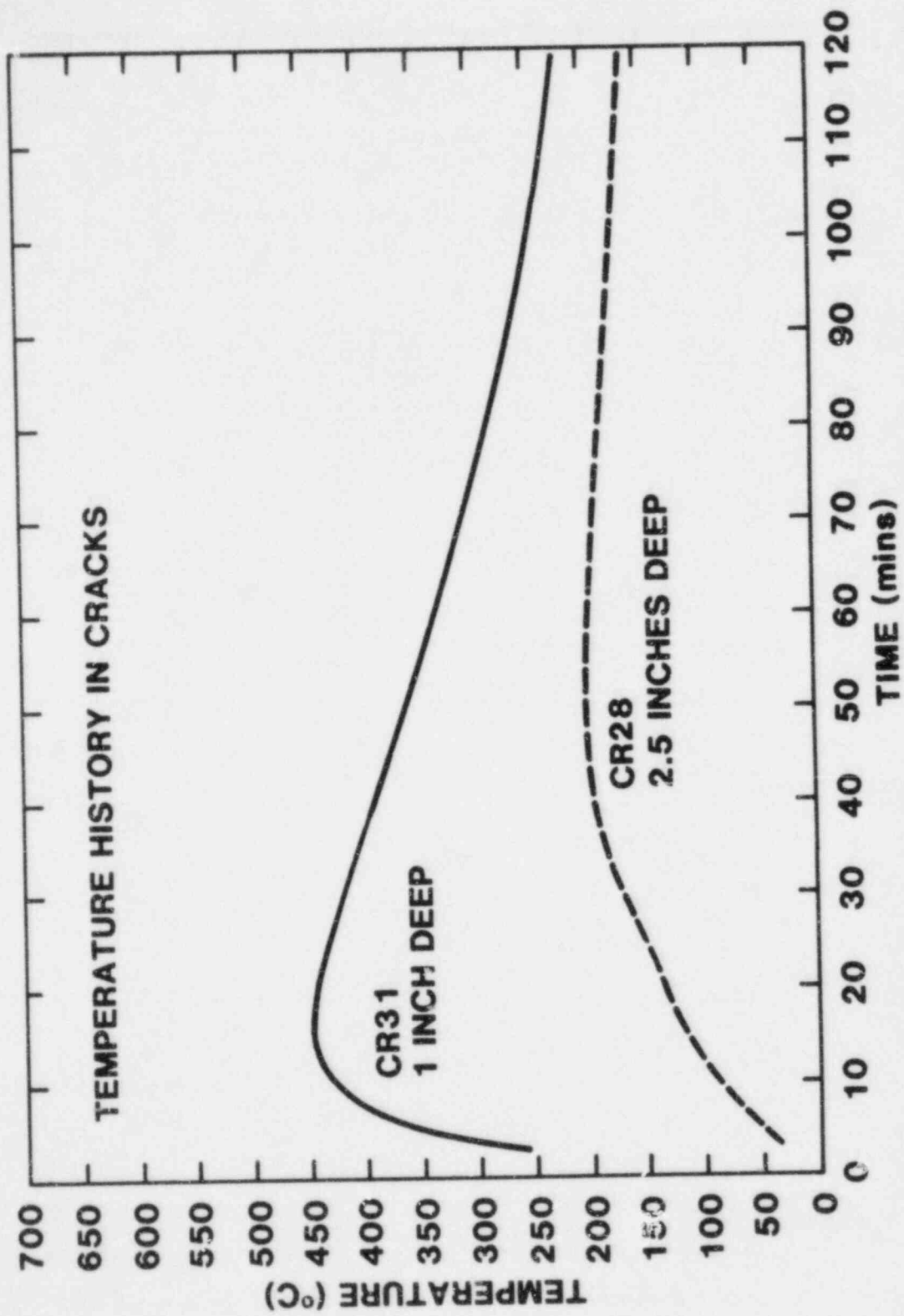


Figure IV.14 Temperature Histories in Cracks

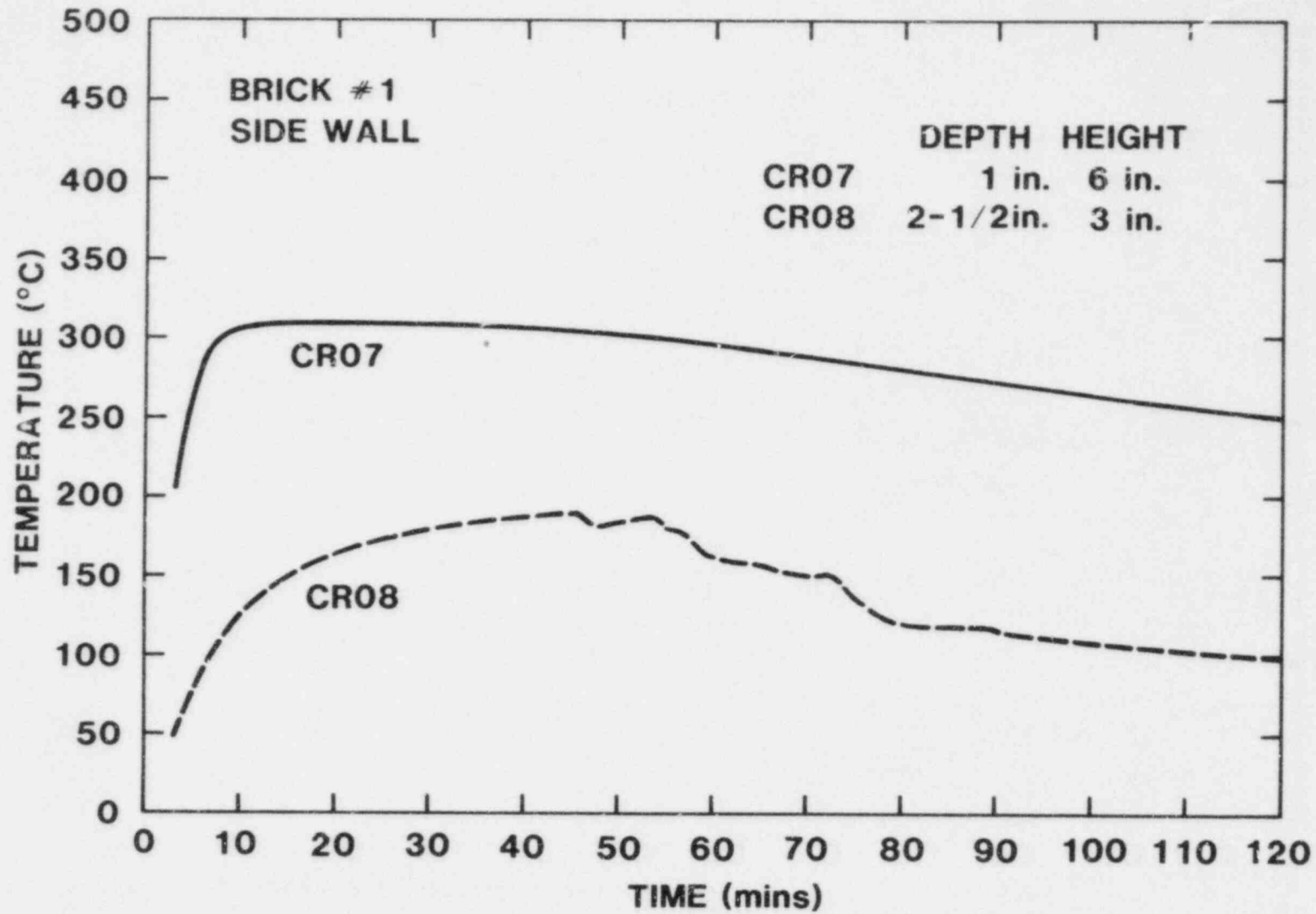


Figure IV.15 Temperature Responses in the Sidewall, Brick #1

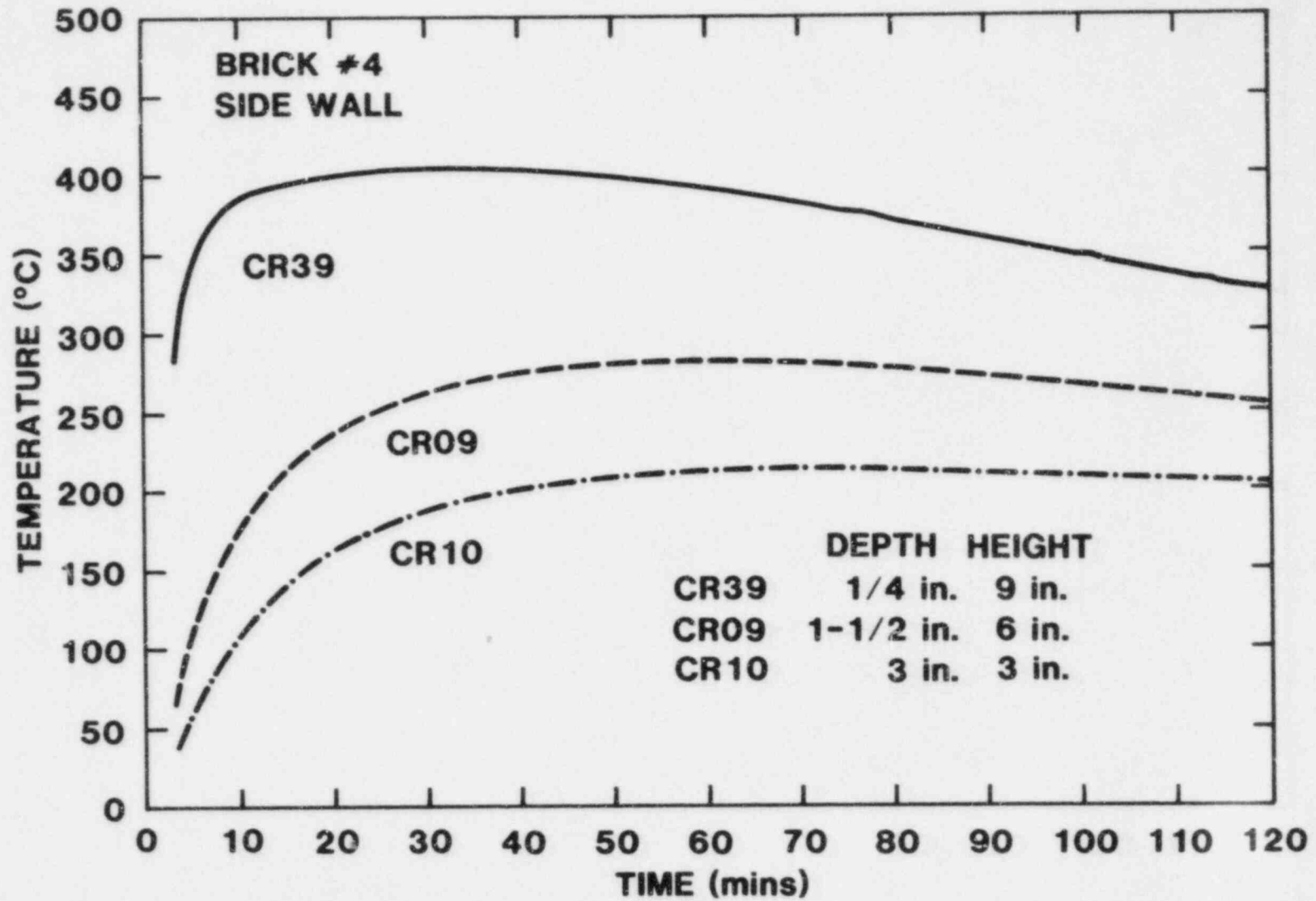


Figure IV.16 Temperature Responses in the Sidewall, Brick #4

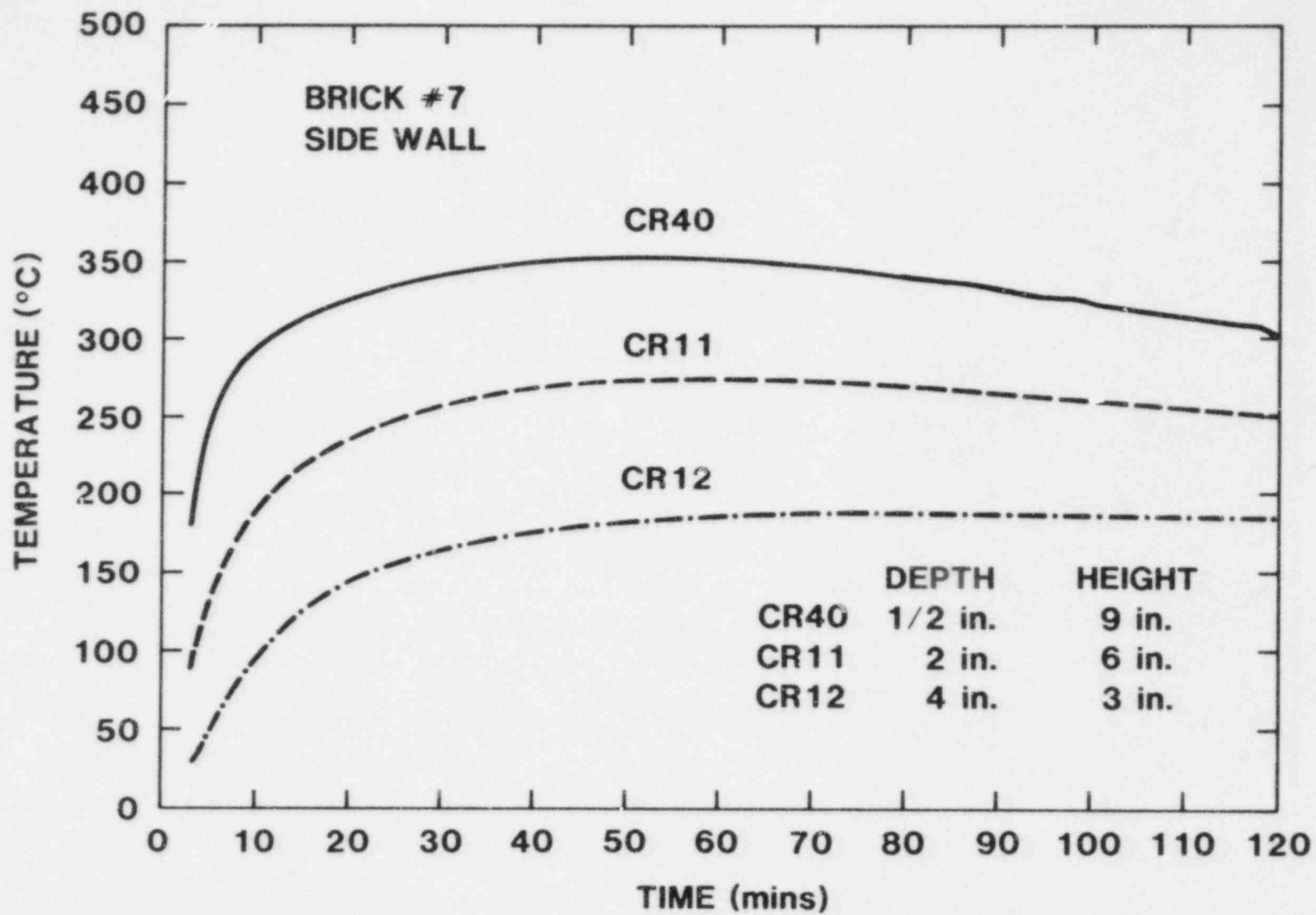


Figure IV.17 Temperature Responses in the Sidewall, Brick #7

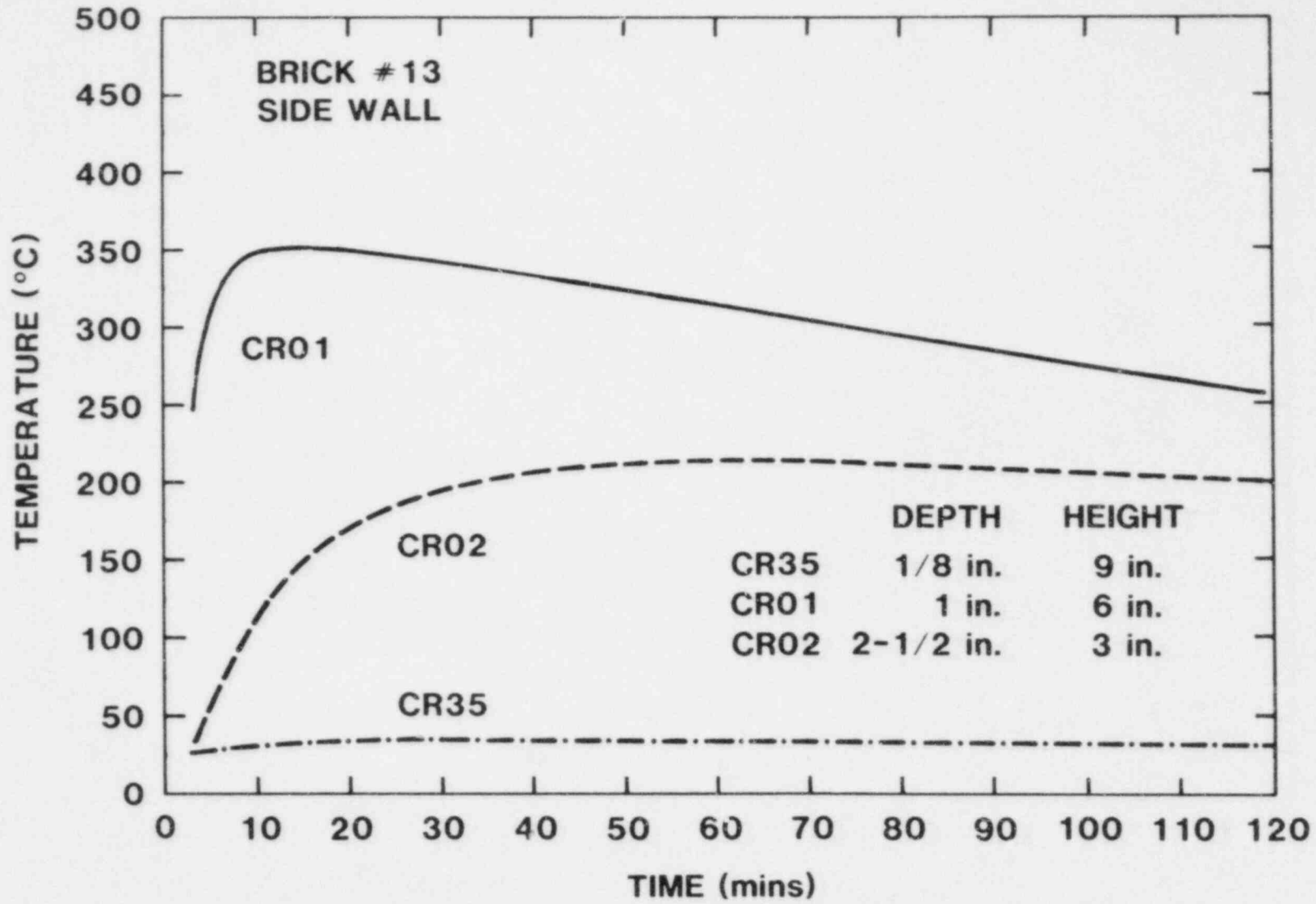


Figure IV.18 Temperature Responses in the Sidewall, Brick #13

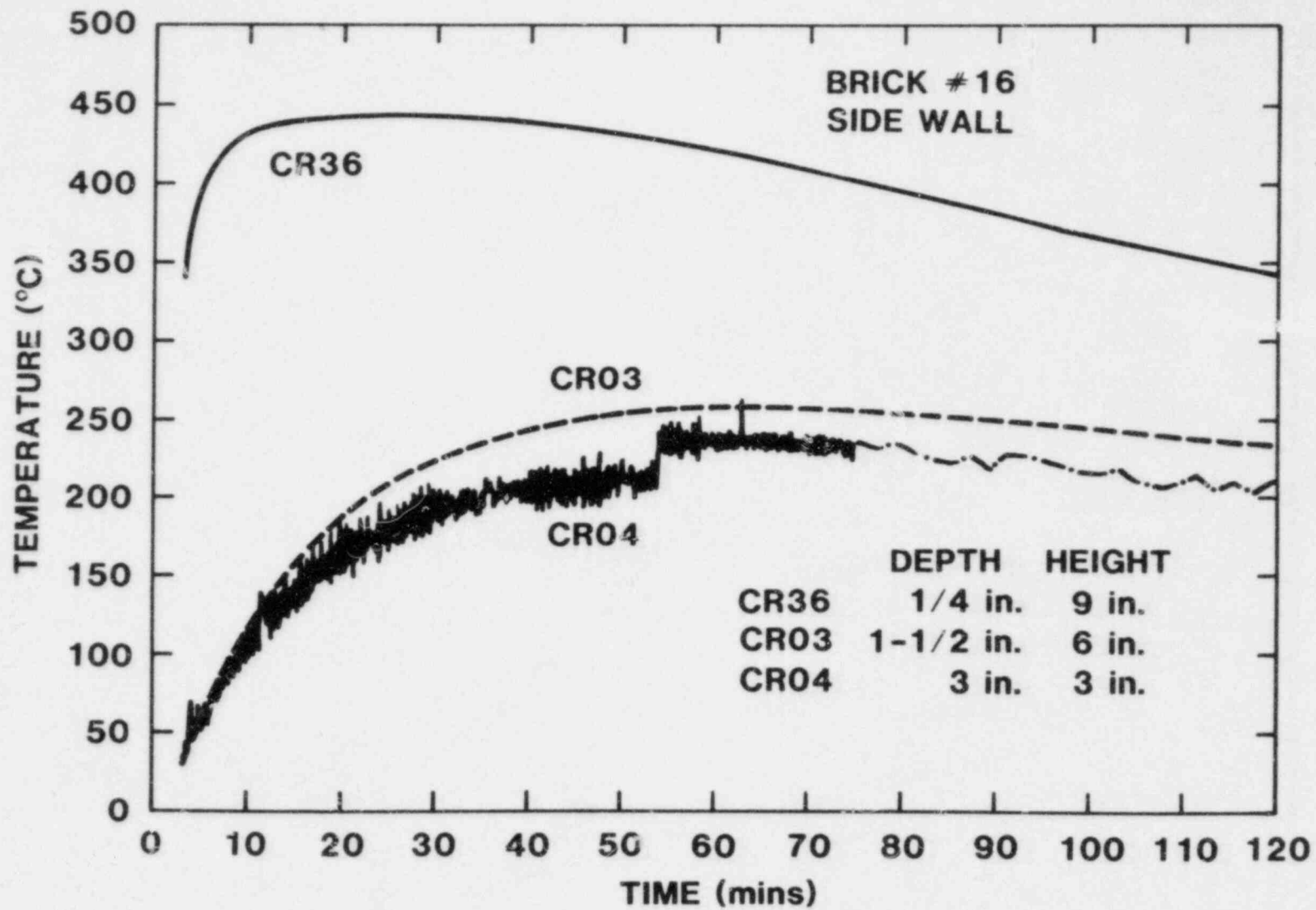


Figure IV.19 Temperature Responses in the Sidewall, Brick #16

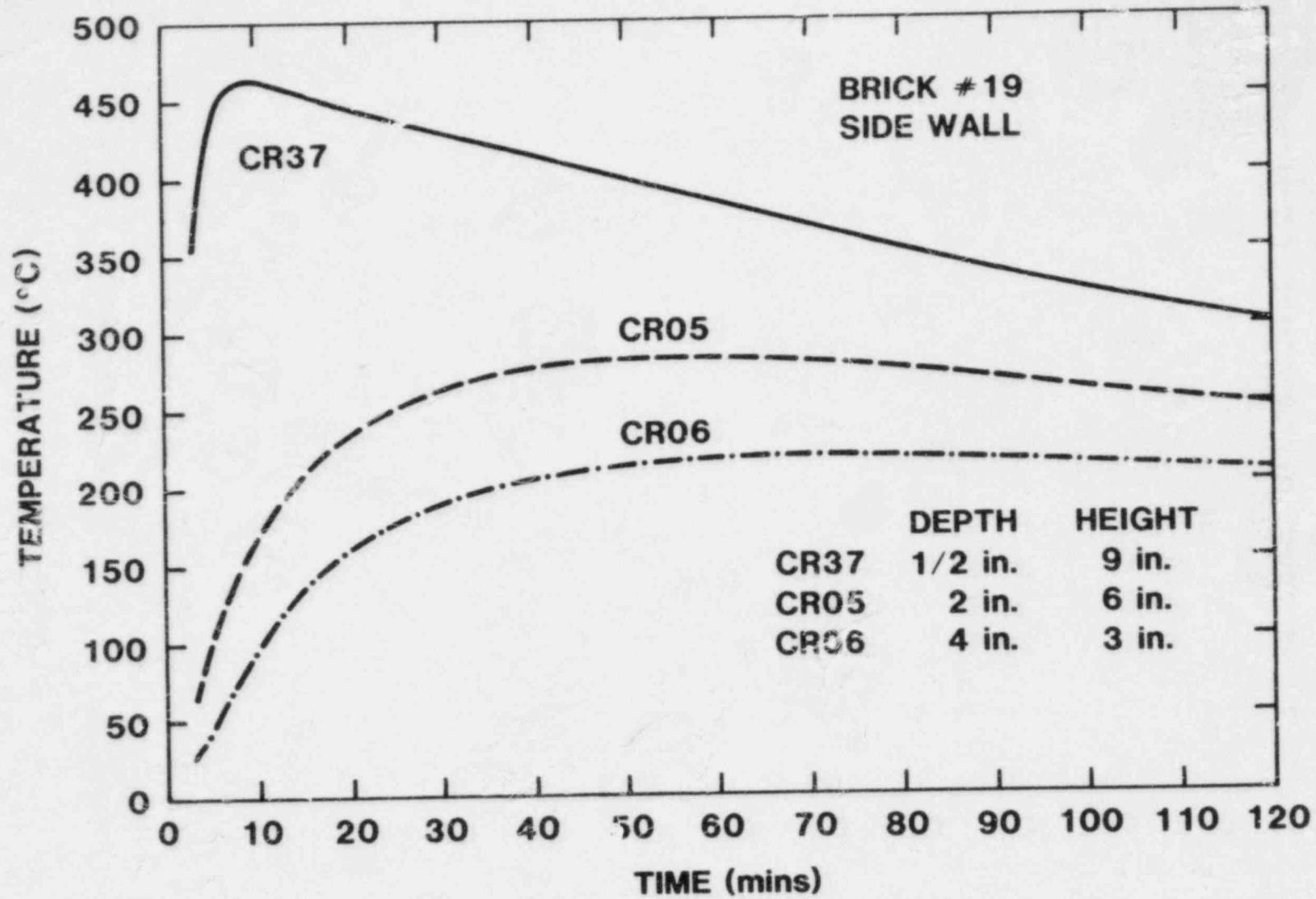
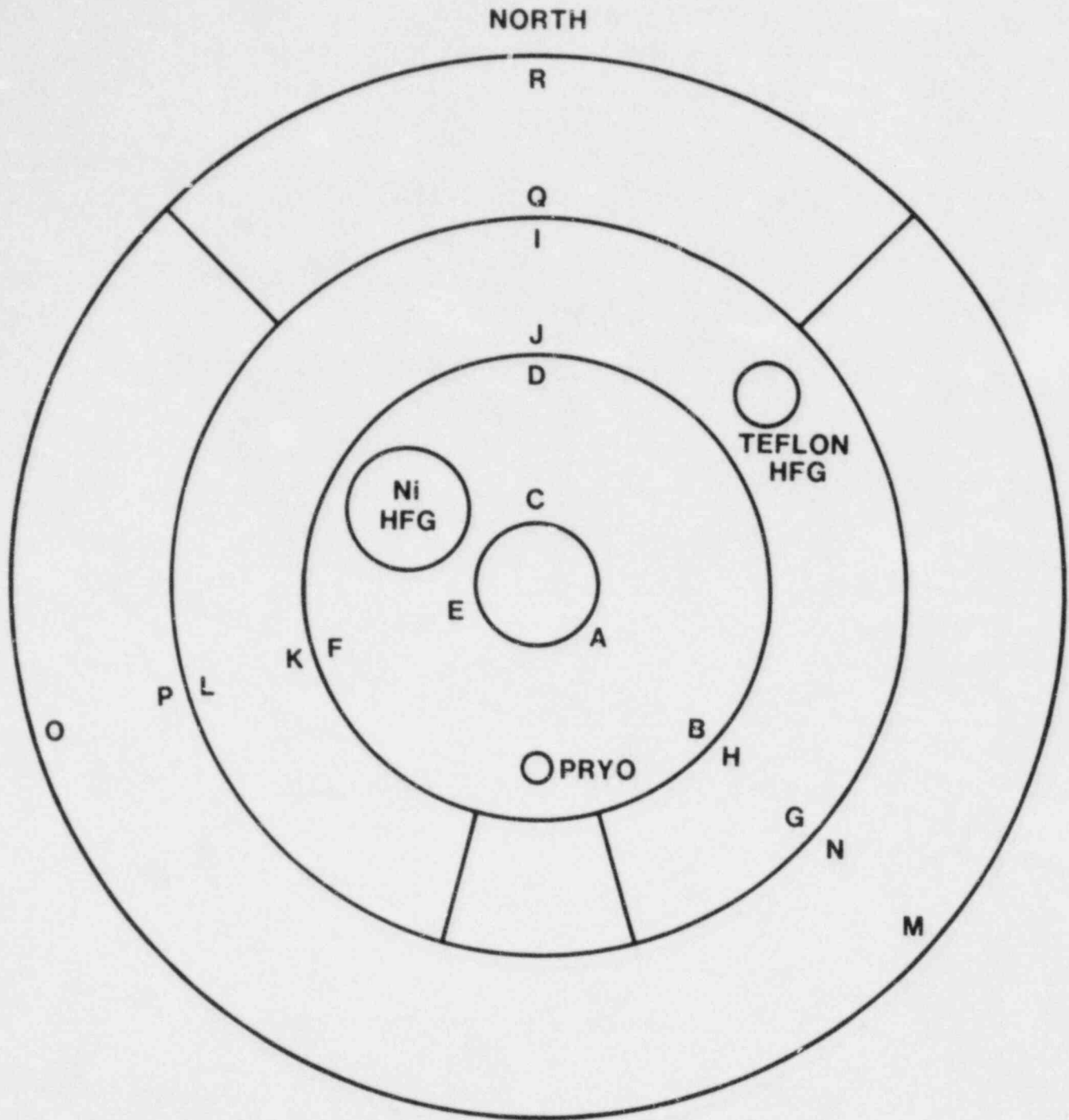


Figure IV.20 Temperature Responses in the Sidewall, Brick #19



X-RAY VIEW LOOKING TOP TOWARD BOTTOM

Figure IV.21 Schematic of Instrumentation in the Shield

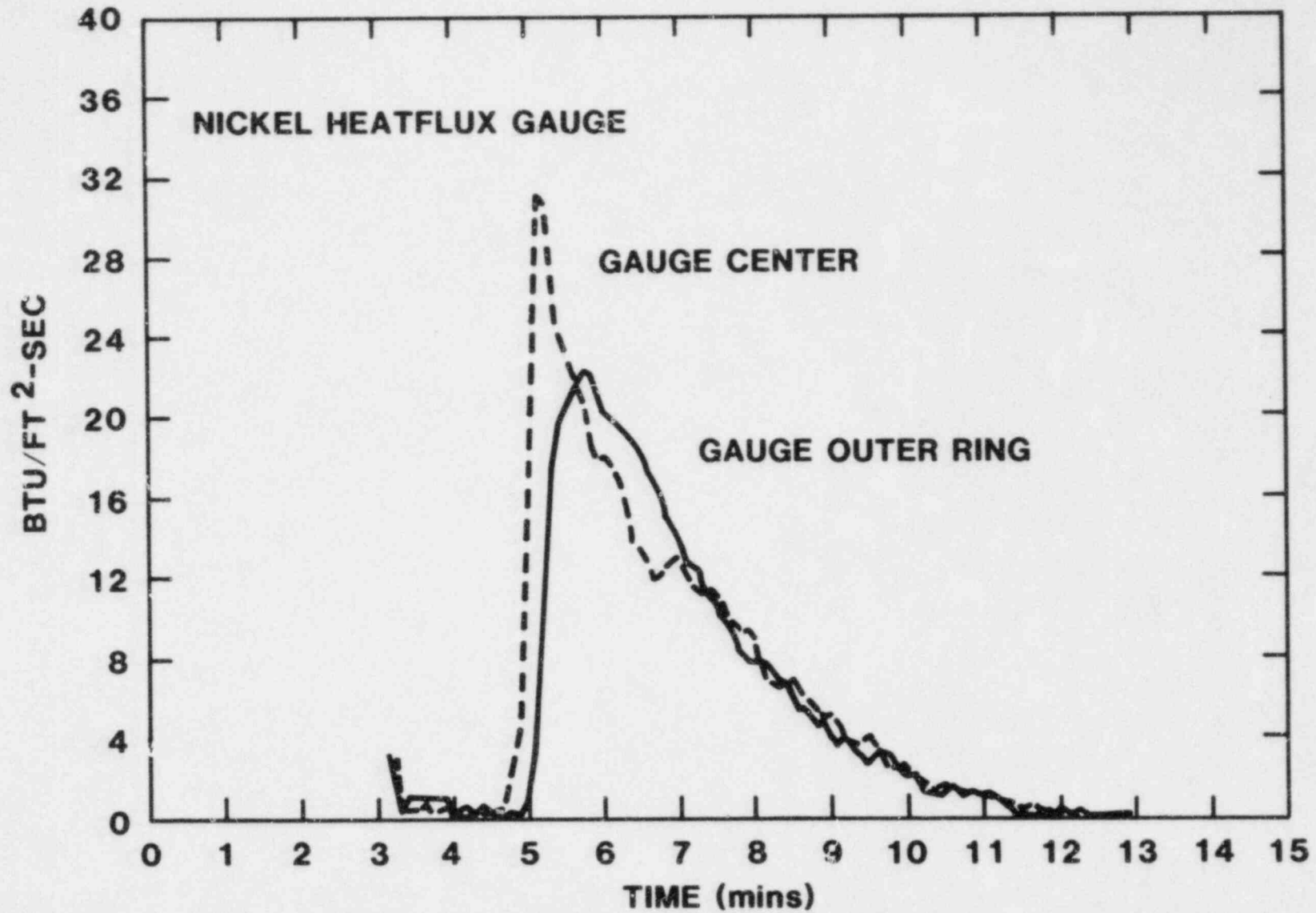


Figure IV.22 Heat Flux Impinging on the Nickel Heat Flux Gauge

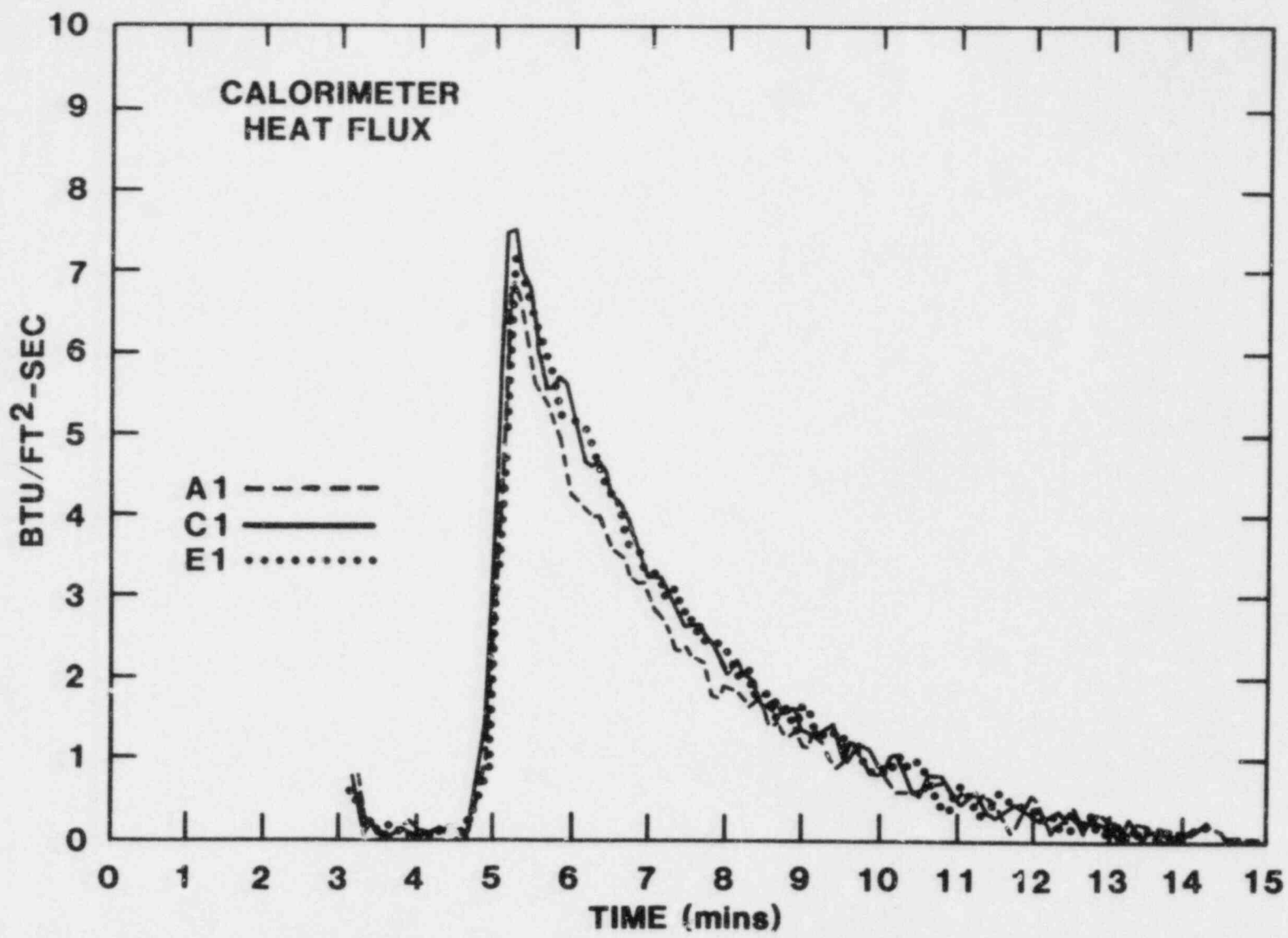


Figure IV.23 Heat Flux into the Heat Shield at Locations: A, C, E

in a net positive stress distribution in the material. This latter type of stress generation is not expected to cause cracking unless the stress is great enough to cause a buckling or spall-type failure.

The response of the brick when exposed to a heat flux on the front face can be estimated by considering the spatial temperature distribution. If the molten pool covers the entire brick face, then the major portion of the brick (away from the lower boundary) can be assumed to behave as a semi-infinite body. The temperature distribution for a constant surface temperature is given as:

$$\frac{T(x,t)-T_s}{T_i-T_s} = \text{erf}\left(\frac{x}{2\sqrt{\alpha t}}\right) \quad (\text{IV.1})$$

where

T - temperature
 x - distance from surface
 α - thermal diffusivity
 t - time
 subscript i,s - initial and surface, respectively
 erf - error function.

The solution of equation IV.1 would have the general form shown in Figure IV.24, with the temperature increasing with time and decreasing with distance. Because magnesia has a positive thermal coefficient of expansion, the behavior shown in Figure IV.24 suggests that the degree of expansion decreases with the distance from the front face.

Near the lower boundary of the brick, the temperature distribution is no longer one-dimensional because of the influence of the horizontal brick bed. The loss of heat downward would cause the isotherms to be nonplanar, curving back towards the front face, as shown in Figure IV.25. As a result, the induced thermal stress pattern will be different in the region at the intersection of the sidewall and horizontal brick bed than that in the remaining portion of the brick.

If the brick is assumed to behave as a flat plate with a uniform face temperature T' and a linear gradient over a small distance d , then the maximum bending stress for fixed ends (worst-case) is given as [9]:

$$S = \frac{1}{2} \frac{\Delta T \alpha E}{(1-\nu)} \quad (\text{IV.2})$$

where:

S = bending stress
 ΔT = temperature difference
 α = thermal coefficient of expansion
 E = modulus of elasticity
 ν = Poisson's ratio.

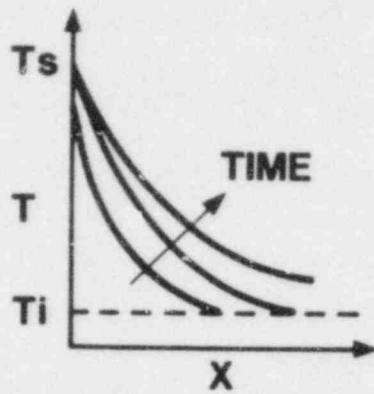


Figure IV.24 Temperature Profiles for Semi-Infinite Body Exposed to a Constant Temperature on One Surface

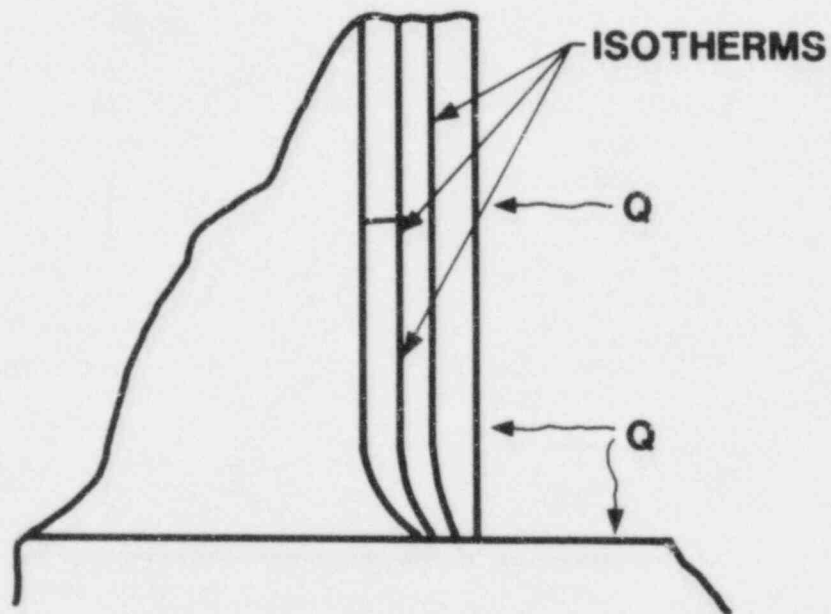


Figure IV.25 Brick Isotherms Near the Floor of the Cavity

An estimate of the temperature differential required to exceed the material strength can be found from equation IV.2 using applicable handbook values* for the other variables.

$$\Delta T = \frac{3000 \text{ lb/in}^2 (2)(1-.2)}{1.44 \times 10^{-5} \text{ in/in/}^\circ\text{C} \ 30 \times 10^6 \text{ lb/in}^2}$$
$$= 11.1^\circ\text{C}$$

This result suggests that relatively small temperature gradients will cause the rupture strength of the magnesia to be exceeded. Representative thermocouple plots Figure IV.26 indicate temperature differences of 100-200°C between sensors located nominally 3 centimeters apart. Extrapolating the temperature profiles to melt deposition time (0 second) indicates that sufficiently large gradients for crack damage existed very early in the event (less than 1 minute). Temperature measurement at locations closer to the exposed surface were not available, but it is assumed that the gradient was even more dramatic.

Data from the test are given in Figure IV.27, with both plots from the same brick. For the duration of the recording time, no change in the output was noted for the second brick, or for other arrays on the same brick. The two traces are from the topmost and bottommost networks of the same brick. Only a single failure, element 1, is seen on the lower array, occurring at 4.75 seconds after start of the melt pour into the crucible. The top array indicated a similar failure approximately 60 seconds later. The delay in the response of the two arrays may be attributed to the duration of the melt pour, so that the full heat to the upper array occurred later. The absence of similar failures in the other arrays, combined with the difference in time between the two failures on the same array, suggests that the crack may not have been parallel to the surface. Thus, the recorded data represents two or more cracks.

Diagonal crack patterns of the type shown in Figure IV.28 were observed in previous tests using molten thermite introduced into a magnesia crucible. The orientation of this type of crack appears to result from a shear failure caused by the bending stress in the horizontal direction and a vertical stress induced by the interference between the expanding sidewall and floor bricks.

The sampling time of the recorders was set to provide a resolution adequate to resolve crack-propagation velocity. The melt was also assumed to have entered the crucible in a time less than 1 minute, so that the heat transfer to the bricks would be very rapid and the crack development would occur very soon after the melt enters the crucible. A longer recording time would have been beneficial in this test because of the slower-than-expected evolution of the crack patterns.

*Engineering Properties of Selected Ceramic Materials, The American Ceramic Society, Columbus, Ohio, 1966.

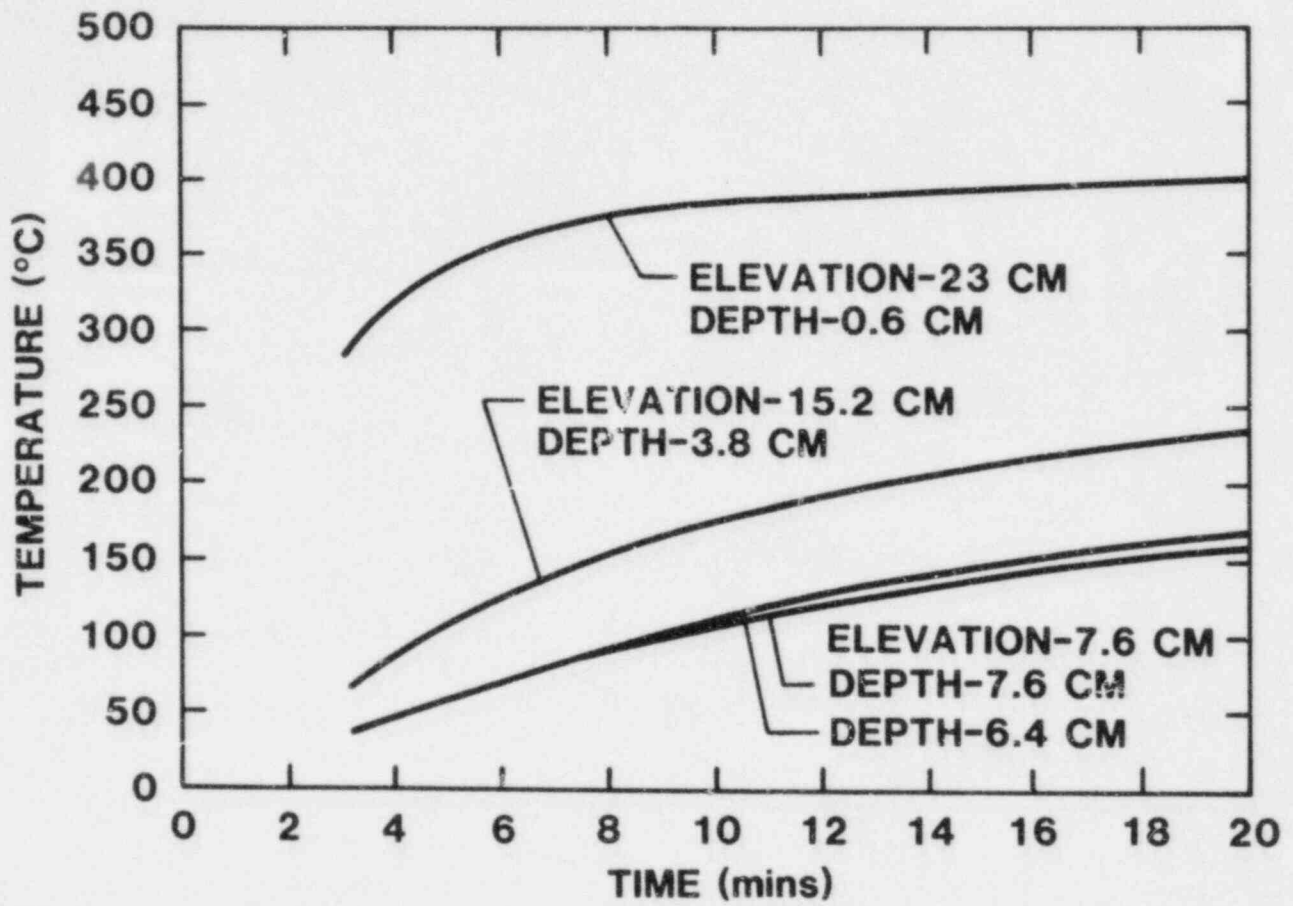


Figure IV.26 Brick Temperature Data

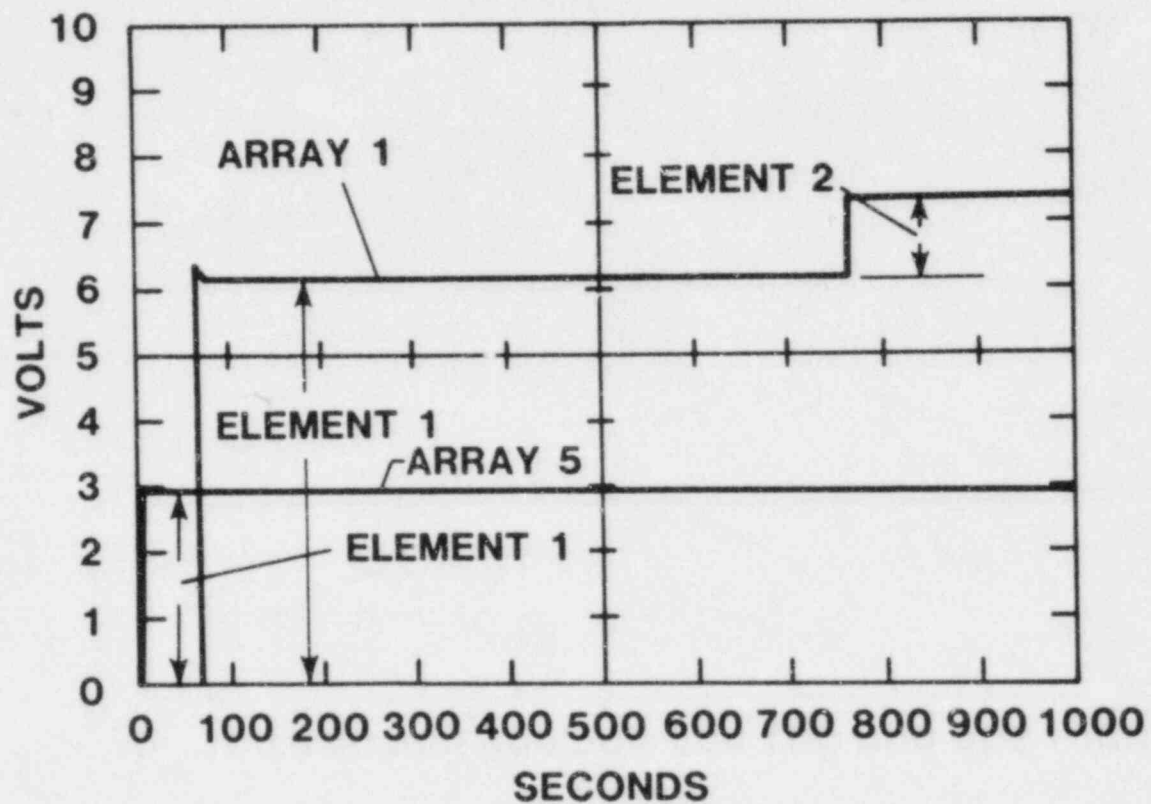


Figure IV.27 Recorded Data from Crack Detection Sensors



BRICK 9

Figure IV.28 Diagonal Crack Patterns Seen in Molten Thermite Tests

Disassembly of the brick crucible is expected to show that damage of the type in Figure IV.28 occurred. The gauge records suggest that diagonal cracks should be apparent at both the top and bottom corners. Longitudinal cracks parallel to the exposed surface have not been diagnosed but may have occurred later. The existence of at least the two diagonal cracks suggests that prompt damage of bricks is possible. If more cracks are found upon disassembly, future tests should use longer recording times to insure that these late-time effects are monitored. Cracks that develop during the cooling period may not be prototypic of accident situations.

V. Early Stages of Post-Test Dissection

a. Melt Crucible

The melt crucible appeared to have been tapped very close to the edge of the susceptor bottom hole, Figure V.1a and V.1b. The melt stream actually eroded away a path approximately 1 in. x 1 in. in the susceptor. Two "dents" are also evident on the bottom of the crucible, one at the center and one 1 1/4 in. away. At this time, investigators are not sure whether the "dents" were unsuccessful penetrations or whether they were simply caused by solidified melt.

The entire outside surface of the crucible was carburized; the carbide layer was approximately 0.04 to 0.05 in. thick. Underneath the carbide layer the Ta-10W outer crucible was found to have melted. In the cylindrical section of the crucible, the hydrostatic pressure of the melt had pushed the carbide layer out against the graphite susceptor, see Figures V.2 and V.3. The Ta-10W in the lid also melted away and the instrumentation passthroughs were held up only by the plasma-sprayed tungsten. The tungsten-sprayed layer, the liner, and the tungsten packing powder in between were sintered into one piece and was essentially intact. Quite remarkably the plasma-sprayed tungsten applied to the inside of the Ta-10W crucible did not seem to have formed any metallurgical bond with the crucible. The crucible simply melted away and left the sprayed layer standing. The surface details of the crucible such as the weld line and machining marks that were replicated at the mating surface between the sprayed layer and the crucible were still visible, Figure V.3.

A view of the inside of the crucible is shown in Figure V.4. The hairline crack initially on the liner grew to a width of 1/8 in. corresponding to an increase of the diameter of 0.04 in. The initial level of the melt could be seen quite distinctly because of a change of color of the liner surface. The melt line was 3.75 in. below the edge of the plasma-sprayed tungsten layer and the undrained, solidified charge was 16 in. below the edge. Two breaks were visible in the liner, one about 1 in. x 1.7 in. just above the melt line, Figure V.5, the other a crack-like break diametrically opposite the first one and 12 in. down from the edge of the tungsten sprayed liner, Figure V.6. Molten material resembling solidified wax dripping appeared under this crack protruding from the solidified melt, Figure V.6. A similar pile of drippings was also observed under the crack in the

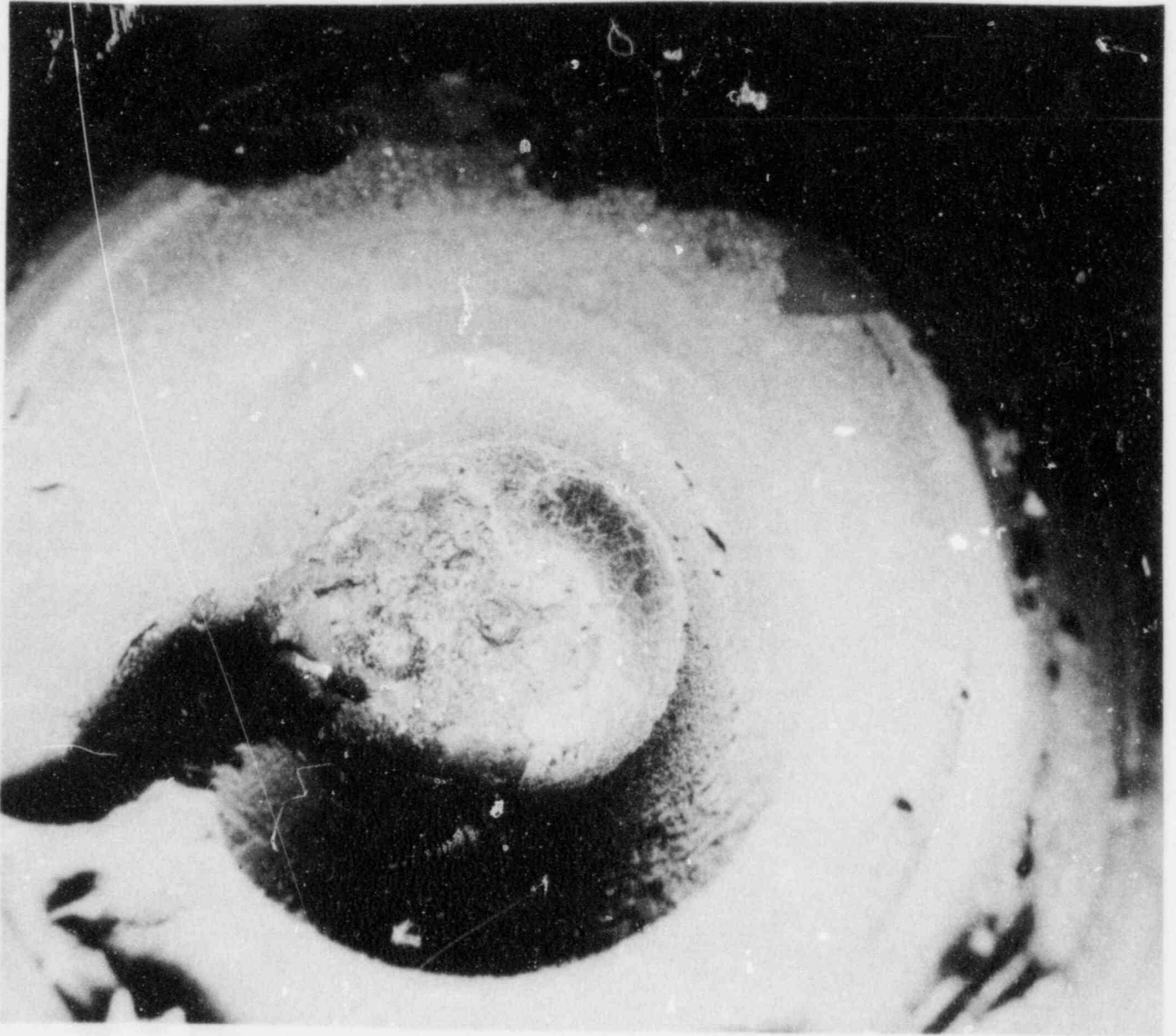


Figure V.1a View of Bottom of Melt Crucible

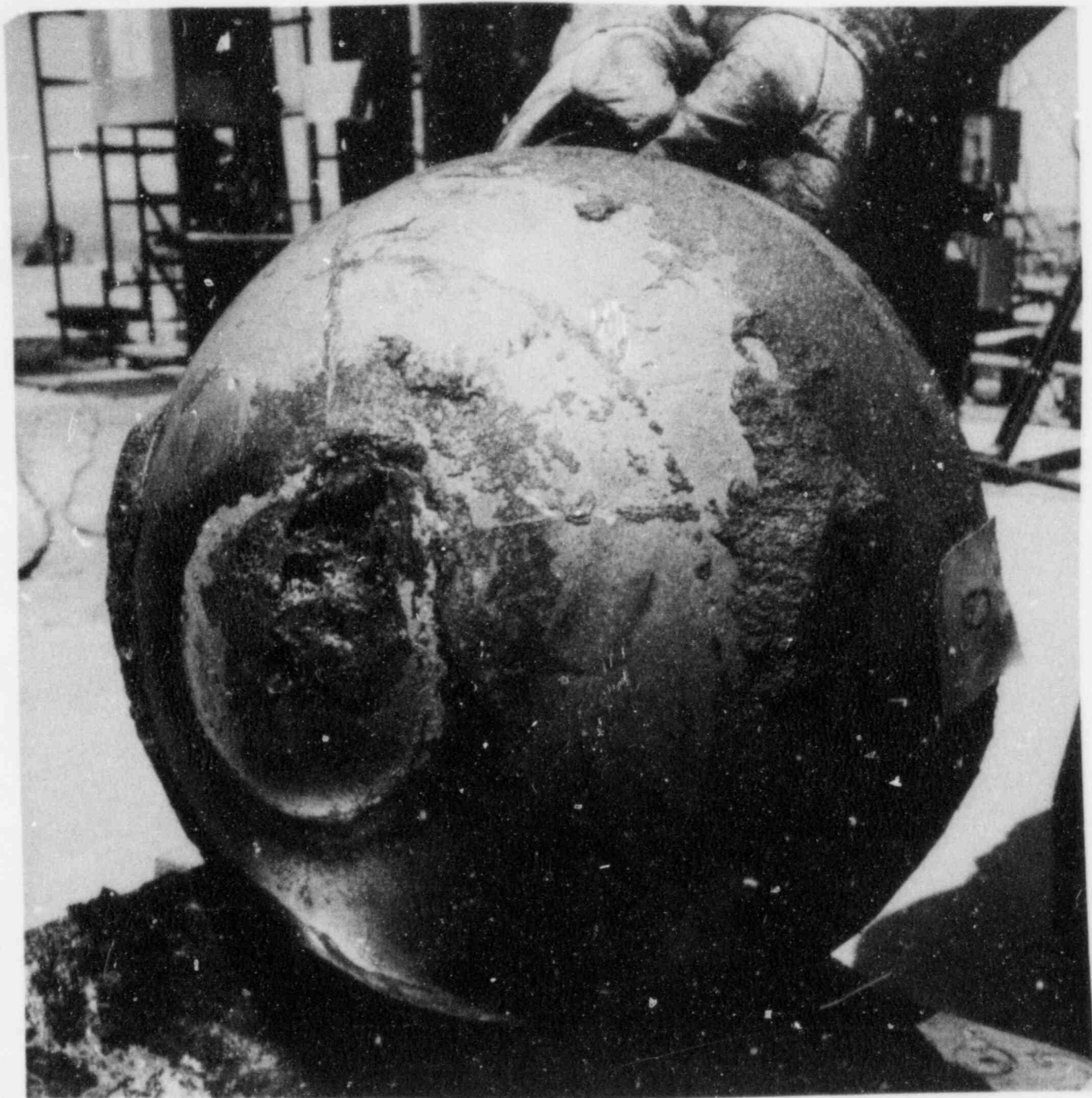


Figure V.1b View of Bottom of Melt Crucible

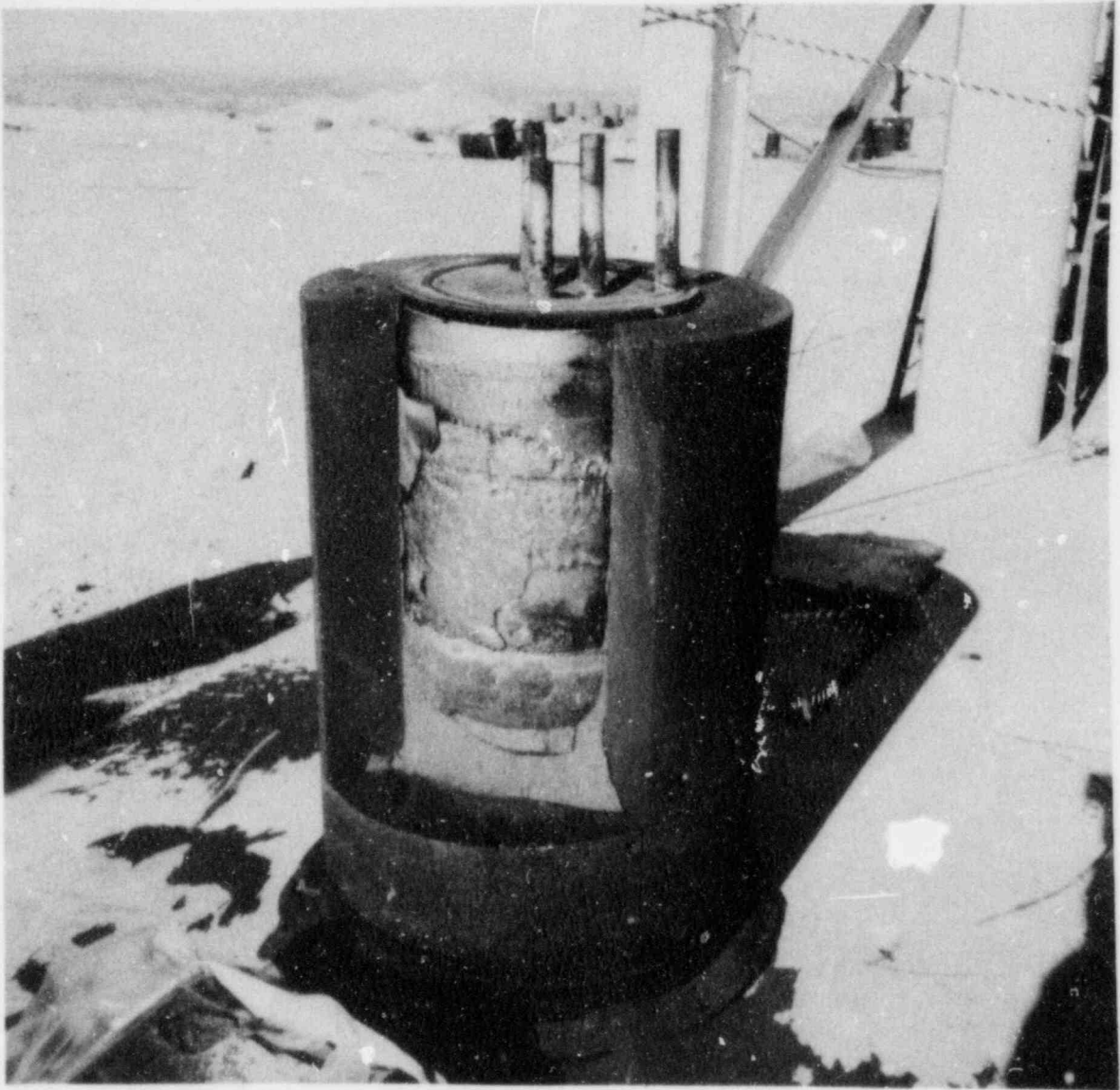


Figure V.2 Melt Crucible After the Test

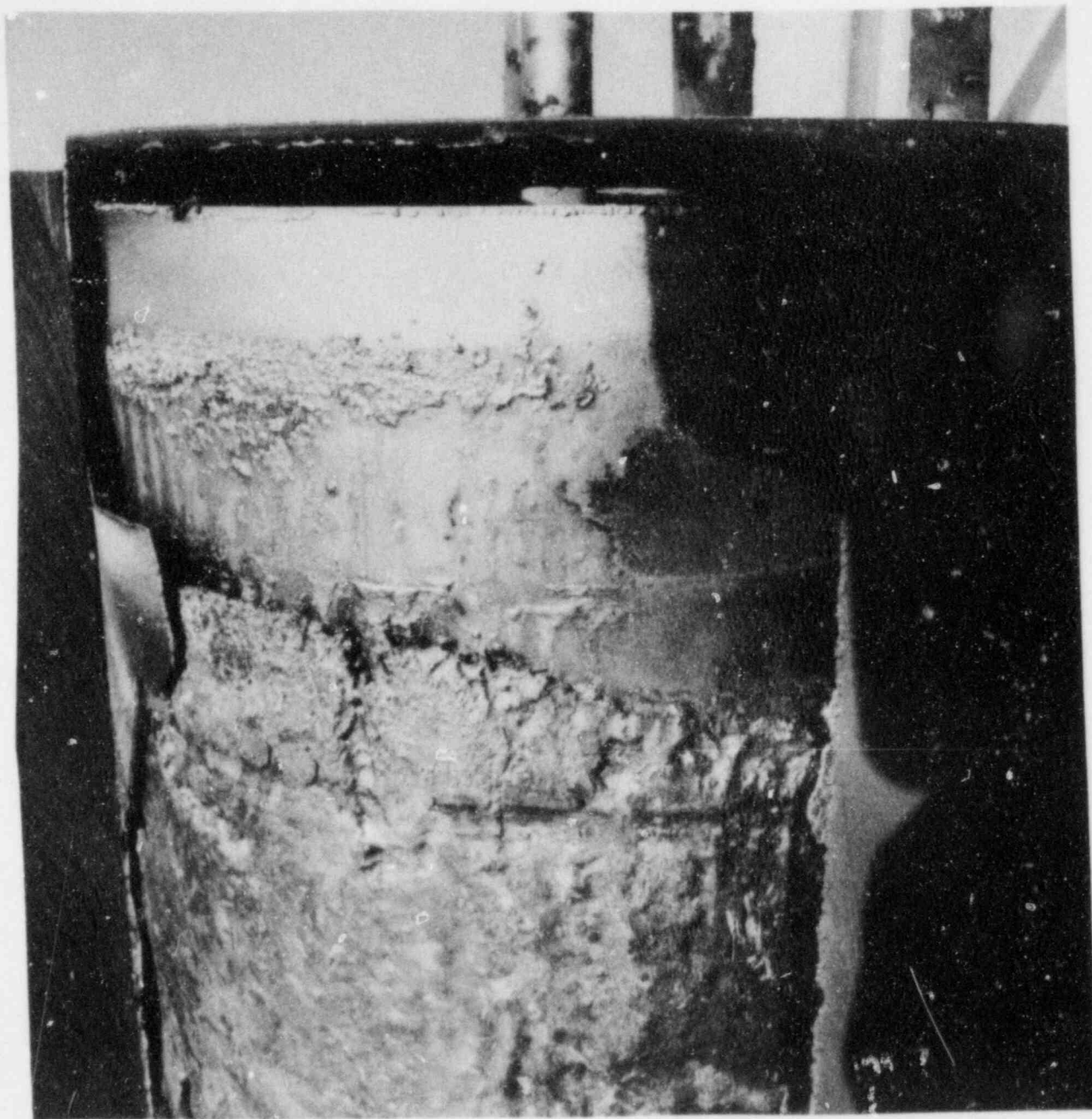


Figure V.3 Melt Crucible After the Test - A Closer View

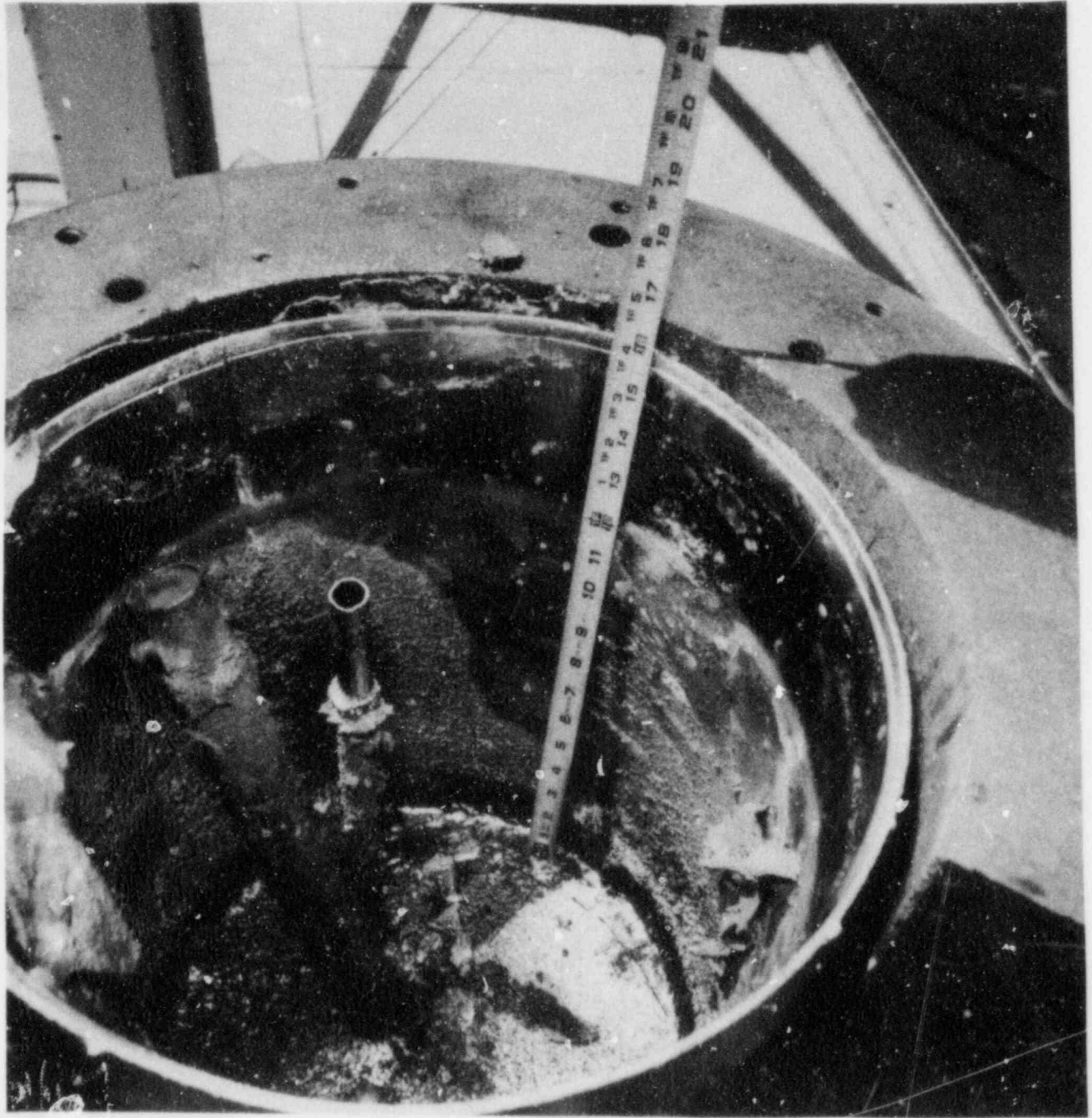


Figure V.4 A View of Inside of the Melt Crucible

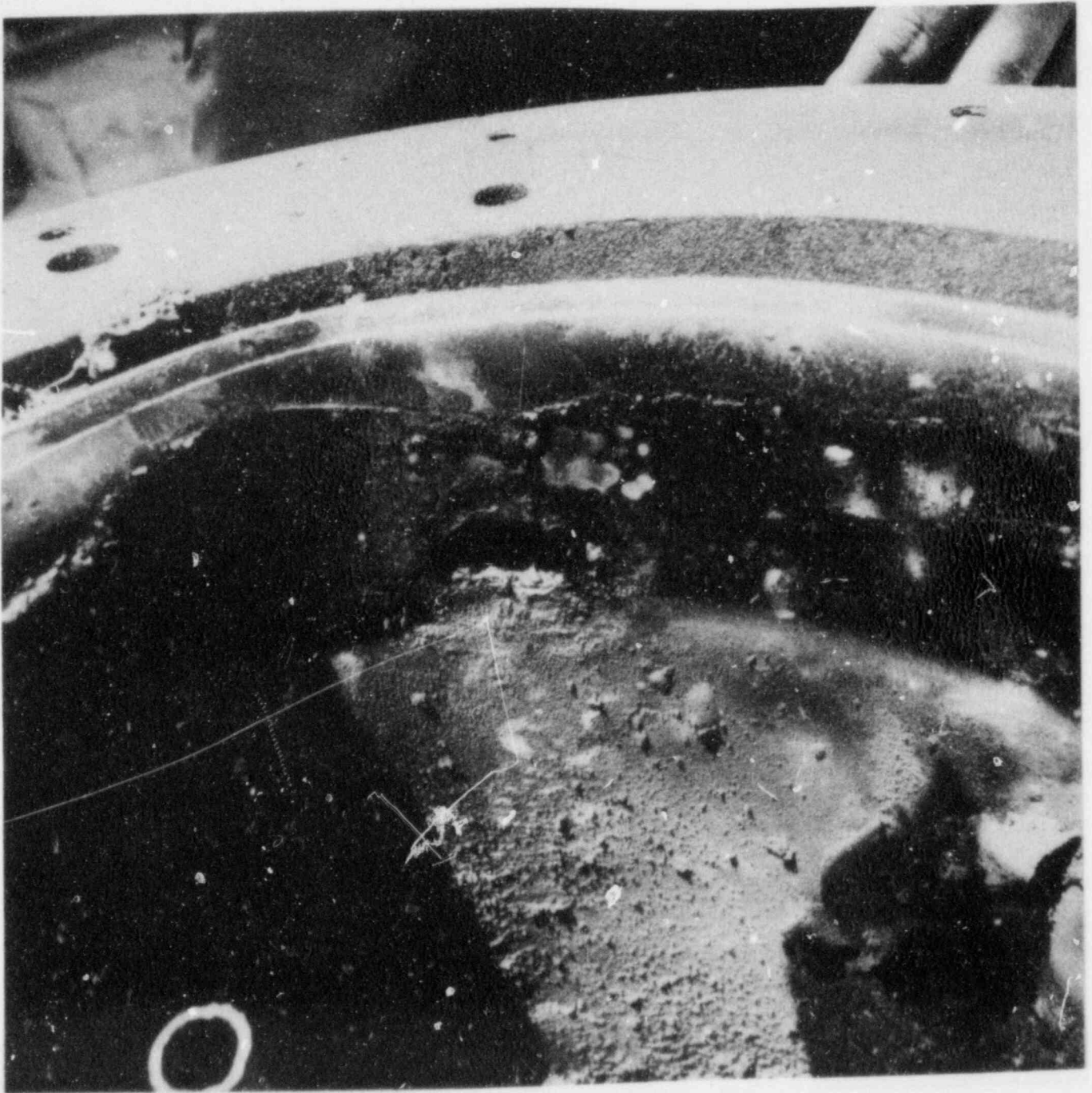


Figure V.5 Break in the Melt Crucible Above the Melt. Line

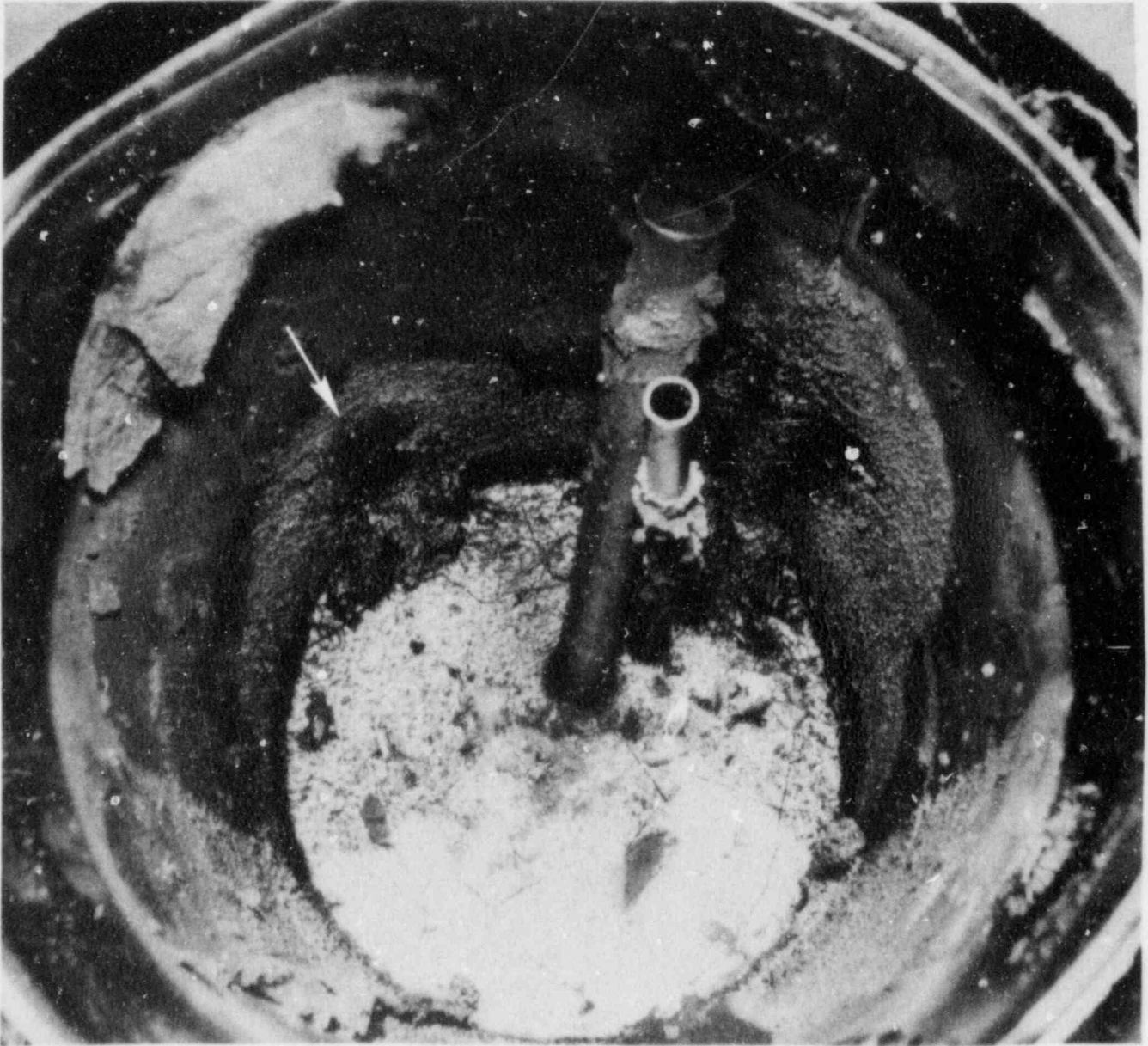


Figure V.6 Crack Like Break in the Liner

liner. When the melt charge was chipped away, the crucible bottom was found to be filled with approximately 2 in. of molten metal, Figure V.7. Apparently the two dripping sites were feeding a molten pool. Molten Ta-10W probably leaked into the crucible from these sites. The surface of the molten metal was very smooth indicating that the metal and the charge were both once molten.

The Ta-10W pyrometer well was melted near the lid and the tungsten sheath attached to it dropped into the melt. Length measurements indicate that the sheath reached all the way to the bottom of the crucible indicating that the charge was totally molten at tapping. Melt level measurements revealed that 85% or 200 kg of the charge was dropped.

b. MgO Crucible

The top of the crucible box was covered with melt debris, Figure V.8. Some of the debris appeared to be frozen crust of melt streams, others were solidified droplets. The crucible was filled to approximately 20 in. deep, about twice as deep as the expected depth of the molten pool. The top of the melt mass consisted of very loosely packed debris with sizes ranging from mm to cm. X-rays were taken of the melt pool. The X-rays showed that two dense areas of melt existed along the center axis of the crucible surrounded by areas of lesser density. The brick melt interface did not appear to be heavily eroded. X-rays did not show any massive cracks in the bricks in the melt area. Above the pool, more than half of the bricks showed horizontal hairline cracks across the brick. It was uncertain whether the bricks in the pool region also had hairline cracks because these cracks were beyond the resolution of the X-rays. Surface spallation was observed on at least one brick above the melt, the spalled thickness was about 1/8 in.

VI. Ongoing Analysis

a. Melt Crucible

(1) Metallographic Analysis

In all twelve samples for metallographic analysis were taken of the various crucible components both at locations where the crucible components were intact and at locations where apparent failure or interaction might have occurred. Metallographic examination, microstructure analysis, X-ray diffraction, SEM, and microprobe analysis will be used as appropriate to determine:

- (a) charge compatibility,
- (b) susceptor compatibility,
- (c) sintering of tungsten powder,
- (d) liner crack behavior, and
- (e) Ta-10W crucible welds and defects.



Figure V.7 Bottom of Melt Crucible with Melt Charge Removed

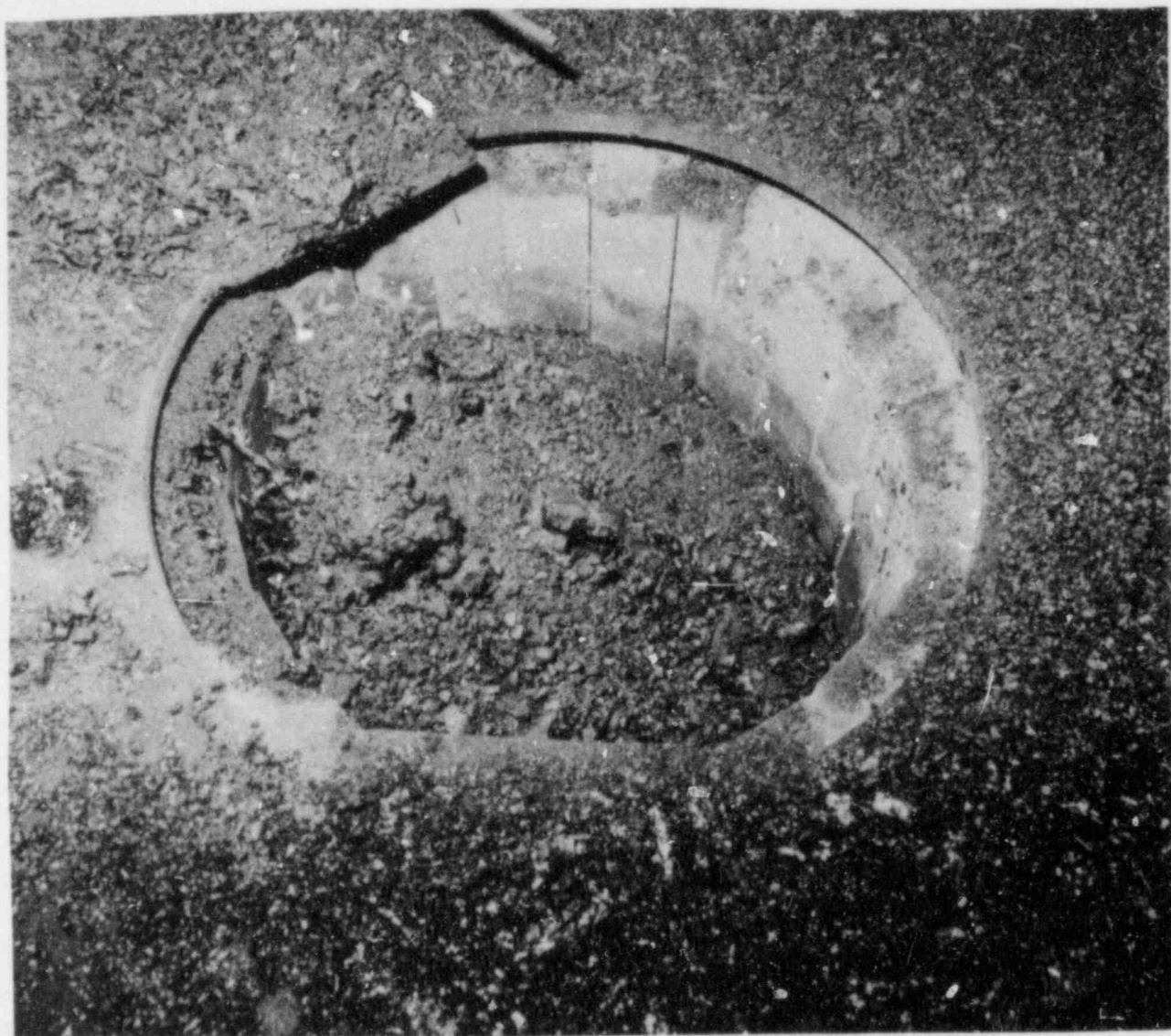


Figure V.8 Top View of Magnesia Crucible

(2) Ta-W-C Phase Diagram

It is not entirely clear why the Ta-10W outer crucible melted while the tungsten sprayed layer remained intact. Because according to published phase diagrams Ta-W-C systems have a liquid phase at 3108 K (2835°C) [10] whereas a W-C system has much lower melting point eutectics. One possibility is that the published phase diagram for T-W-C system may not be accurate. Some independent experiments will be performed to determine the melting regions of the Ta-W-C system.

b. MgO Crucible

The melt in the MgO crucible will be removed layer by layer until all the loose debris are removed. Once the molten pool (one consistent solid piece) is reached, the crucible will be dismantled brick by brick. The material removed will be examined for metal content. This will help to determine the possible sequence of events leading to the failure of the melt crucible. More importantly the melt and the brick will be examined to study:

- (1) melt flow into gaps,
- (2) chemical attack,
- (3) melt composition,
- (4) melt microstructure grain size as a function of location, and
- (5) brick cracking.

c. MgO Thermal Tests and Modeling of Thermal Process

Small scale laboratory tests of magnesia bricks heated by high fluxes (up to 100 W/cm^2) will be conducted, (1) to aid analysis of the LMF test conducted, (2) to define heat transfer in refractory bricks, (3) to assess engineering features in a refractory brick retention device, and (4) to assess the feasibility of backside cooling of a refractory brick crucible.

Existing conduction codes can be used to infer properties and model heat transfer in the brick. In addition, thermal diffusivity and heat capacity measurements will be made of the brick specimens for comparison with code calculations. To understand the molten pool brick interaction work in melting and solidification will be required.

VII. Future Improvements in Melting Technology

a. Tungsten Liner

Because of the butt joint seams on the molybdenum mandrel used for manufacturing the CVD tungsten liner, several ridges appeared on the surface of the liner. The stress resulting from the ridges caused a vertical crack in the liner. To rectify this problem, in the future, the butt joints will be welded and smoothed over. Because the weld will not be strong enough, rivets will still be used to carry the load. The key is to apply just enough heat to melt and close the

joint but not causing the back up rivet plate to recrystallize. Sample sections of the mandrel were manufactured and coated. Preliminary inspection indicates that a ridge-free liner can be manufactured.

b. Tapping

The tapping procedure proved to be not as effective as desired. A number of alternatives are under consideration:

- (1) the use of shaped charge or other explosive driven projectiles
- (2) more powerful tapping gun and projectiles with more penetrating power
- (3) multiple barrel gun and/or multiple firing gun
- (4) the use of an oxygen cutting torch
- (5) the use of an alloy tapping device where an alloying material is brought into contact with the crucible to cause melting of the crucible
- (6) other mechanical piercing devices.

c. Temperature Measurements

Clearly more development work will be required to achieve the desired combination of accuracy and ruggedness for the ultrasonic thermometers. For the present because of the signal attenuation problems associated with long probes, one possibility is to concentrate on making shorter probes with fewer measuring intervals more reliable. With this objective achieved, work can again be directed at using the device to obtain profile measurements. Another possible solution would appear to be the use of pulses having much lower frequency content and thus resulting in significantly less attenuation. This has not yet been investigated. However, it must be stressed that this will result in degradation of the resolution of the instrument, limiting the number of measuring zones to probably no more than two or three.

Pyrometers were shown to be quite useful especially at the later stages of the experiment. More locations for this type of measurement will be useful in future experiments. Two color pyrometers or pyrometers using fiber optics conduits are under consideration. Using these techniques, measurements can be made at locations previously inaccessible or too small for line of sight measurements.

VIII. Concluding Remarks

This test represents the largest simulation of a nuclear reactor core meltdown accident ever carried out with prototypic materials, 200 kilograms of molten core material was dropped into a magnesia brick crucible at Sandia National Laboratories Large-Scale Melt Facility. The test provided important data on the ability of magnesia bricks as a material for core ladle.

The crucible was most effective in containing the molten core material produced. No violent interactions occurred. Aerosols generated during the test were orders of magnitude less than they would have been had the material been dropped onto concrete or into water. No detectable amount of combustible gas was observed during the interaction.

With this facility operational, Sandia is now in a unique position to address many of the complex questions related to the most severe accidents that can occur in nuclear reactors. In the future, the facility will be used to study other core retention concepts and the interactions between prototypic reactor core debris and concrete.

References

1. FNP Core Ladle Design and Safety Evaluation, Topical Report No. 36A59, Offshore Power Systems, April 1979.
2. Ex-Vessel Core Catcher Concept Evaluation Report, WARD-D-0103, Westinghouse Electric Corp., October 1975.
3. K.H. Sigurdson and T.Y. Chu, Thermal Analysis of Large Melt Furnace - Performance Evaluation of Susceptor-Crucible Design, SAND81-1262, Albuquerque, NM, Sandia National Laboratories, July 1983.
4. R.E. Taylor and H.Groot, Thermal Diffusivity of $UO_2-Y_2O_3$ A Report to Sandia Laboratories, TPRL 253, Purdue University, Thermophysical Properties Research Laboratory, 1982.
5. M. Pilch, MgO and 70W% UO_2 -30W% Y_2O_3 : Thermophysical and Transport Properties, SAND81-1230, Albuquerque, NM, Sandia National Laboratories, Feb. 1982.
6. H.W. Godbee and W.T. Zeigler, J. App. Phys. 37, 1, 56 1966.
7. Advanced Reactor Safety Research Quarterly Report, April to June, 1980, NUREG/CR-1594 (2 of 4); SAND80-1646 (2 of 4), Albuquerque, NM, Sandia National Laboratories, May 1981.
8. A.W. Mullendore and S.F. Duliere, "Analysis of Laboratory Crucible Melt Materials," Memo to D. A. Powers, Sandia National Laboratories, Albuquerque, NM, Nov. 1982.
9. R.J. Roark and W.C. Young, Formulas for Stress and Strain, 5th Edition, p. 538, McGraw-Hill, New York, 1975.
10. E. Rudy, Compendium of Phase Diagram Data, AFM-TR-65-2, Part 5, pp. 502-505, Air Force Materials Laboratory, Metals and Ceramics Division Wright-Patterson AFB, Ohio, May, 1969.

Distribution:

U.S. NRC Distribution Contractor (CDSI) (275 copies)
7300 Pearl Street
Bethesda, MD 20014
275 copies for R7

U.S. Nuclear Regulatory Commission (7)
Office of Nuclear Regulatory Research
Washington, DC 20555
Attn: O. E. Bassett
B. S. Burson
R. T. Curtis
C. N. Kelber
J. Larkins
T. Lee (5)
W. Pasedag
M. Silberberg
L. S. Tong
R. W. Wright
T. Walker

U.S. Nuclear Regulatory Commission (4)
Office of Nuclear Regulatory Regulation
Washington, DC 20555
Attn: L. G. Hulman
P. Easky
J. Rosenthal
J. Mitchell

U.S. Department of Energy (2)
Albuquerque Operations Office
P.O. Box 5400
Albuquerque, NM 87185
Attn: J. R. Roeder, Director
Operational Safety Division
D. K. Nowlin, Director
Special Programs Division
For: C. B. Quinn
D. Plymale

U.S. Department of Energy
Office of Nuclear Safety Coordination
Washington, DC 20545
Attn: R. W. Barber

Electric Power Research Institute
3412 Hillview Avenue
Palo Alto, CA 94303
Attn: R. Vogel
R. Sehgal

Distribution (cont)

Professor T. Theofanous
Purdue University
School of Engineering
West Lafayette, IN 47907

Dr. R. Henry
Fauske & Associates
16W070 West 83rd Street
Burr-Ridge, IL 60521

M. L. Corradini
Nuclear Engineering Dept.
University of Wisconsin
Madison, WI 53706

I. Catton
UCLA
Nuclear Energy Laboratory
405 Hilgard Avenue
Los Angeles, CA 90024

Brookhaven National Laboratory (4)
Upton, NY 11973
Attn: R. A. Bari
T. Pratt
G. Greene
T. Ginsberg

Professor R. Seale
Department of Nuclear Engineering
University of Arizona
Tucson, AZ 85721

Oak Ridge National Laboratory (2)
Oak Ridge, TN 37830
Attn: T. Kress
S. Hodge

K. Holtzclaw
General Electric - San Jose
Mail Code 682
175 Kurtner Avenue
San Jose, CA 95125

Argonne National Laboratory (2)
9700 South Cass Avenue
Argonne, IL 60439
Attn: D. Pedersen
D. Cho

Distribution (cont)

Cathy Anderson
Nuclear Safety Oversight Commission
1133 15th St., NW
Room 307
Washington, DC 20005

Battelle Columbus Laboratory (3)
505 King Avenue
Columbus, OH 43201
Attn: P. Cybulskis
R. Denning
J. Gieseke

H. Sheinberg
CMB-06, MS-770
Los Alamos National Scientific Lab.
Los Alamos, NM 87545

J. E. Antill
Berkeley Nuclear Laboratory
Berkeley GL 139 PB
Gloucestershire,
United Kingdom

W. G. Cunliffe
Bldg. 396
British Nuclear Fuels, Ltd.
Springfields Works
Salwick, Preston
Lancs
United Kingdom

Reactor Development Division (4)
UKAEA - Atomic Energy Establishment
Winfrith, Dorchester
Dorset
United Kingdom
Attn: R. G. Tyror, Head
T. Briggs
R. Potter
A. Nichols

Projekt Nucleare Sicherheit (3)
Kerforschungszentrum Karlsruhe
Postfach 3640
75 Karlsruhe
Federal Republic of Germany
Attn: J. P. Hoseman
Albrecht
H. H. Rininsland

Distribution (cont)

Mr. G. Petrangeli
Direzione Centrale della Sicurezza
Nucleare e della Protezione Sanitaria (DISP)
Ente Nazionale Energie Alternative (ENEA)
Viale Regina Margherita, 125
Casella Postale N. 2358
I-00100 Roma A.D.,
ITALY

Dr. K. J. Brinkman
Reactor Centrum Nederland
P. O. Box 1
1755 ZG Petten
THE NETHERLANDS

Mr. H. Bairiot, Chief
Department LWR Fuel
Belgonucleaire
Rue de Champde Mars. 25
B-1050 Brussels,
BELGIUM

Dr. S. Saito
Japan Atomic Energy Research Institute
Takai Research Establishment
Tokai-Mura, Naku-Gun
Ibaraki-ken
JAPAN

Wang Lu
TVA
400 Commerce, W9C157-CK
Knoxville, TN 37902

M. Fontana
Director, IDCOR Program
Technology for Energy, Inc.
P.O. Box 22996
10770 Dutchtown Rd.
Knoxville, TN 37922

H. J. Teague (3)
UKAEA
Safety and Reliability Directorate
Wigshaw Lane
Culcheth
Warrington, WA3 4NE
United Kingdom

Distribution (cont)

Dr. Frau Reusenbach
Gesellschaft fur Reaktorsicherheit (GRS mbH)
Postfach 101650
Glockengasse 2
5000 Koeln 1
Federal Republic of Germany

1831 A. W. Mullendore
1833 R. W. Fisher
1833 F. J. Zanner
3141 C. M. Ostrander (5)
3151 W. L. Garner (1)
6000 E. H. Beckner
6400 A. W. Snyder
6410 J. W. Hickman
6420 J. V. Walker
6420 J. B. Rivard
6421 T. R. Schmidt
6422 D. A. Powers (5)
6422 F. E. Arellano
6422 J. E. Brockmann
6422 R. M. Elrick
6422 E. R. Copus
6422 T. Kerley
6422 D. Lucero
6422 A. L. Ovellette, jr.
6422 J. E. Gronager
6422 E. Randich
6422 A. R. Taig
6423 P. S. Pickard
6425 W. J. Camp
6425 M. Pilch
6425 D. Bradley
6425 A. Suo Anttila
6425 W. Frid
6427 M. Berman
6440 D. A. Dahlgren
6442 W. A. Von Rieseemann
6449 K. D. Bergeron
6450 J. A. Reuscher
6454 G. L. Cano
6454 M. E. Field
7530 T. B. Lane
7531 B. F. Blackwell
7537 N. R. Keltner
7537 T. Y. Chu (5)
7537 R. U. Acton
7537 J. H. Bentz
8424 M. A. Pound

BIBLIOGRAPHIC DATA SHEET

3 TITLE AND SUBTITLE

Report on Large Scale Molten Core/Magnesia Interaction Test

2 Leave Blank

4 RECIPIENT ACCESSION NUMBER

5 DATE REPORT COMPLETED

MONTH YEAR
June 1984

6 AUTHOR(S)

T. Y. Chu, J. H. Bentz, F. E. Arellano,
J. E. Brockmann, M. E. Fields, and J. D. Fish

7 DATE REPORT ISSUED

MONTH YEAR
August 1984

8 PERFORMING ORGANIZATION NAME AND MAILING ADDRESS (Include Zip Code)

Sandia National Laboratories
Albuquerque, New Mexico 87185

9 PROJECT/TASK/WORK UNIT NUMBER

10 FIN NUMBER

A-1227

11 SPONSORING ORGANIZATION NAME AND MAILING ADDRESS (Include Zip Code)

12a TYPE OF REPORT

12b PERIOD COVERED (Inclusive dates)

13 SUPPLEMENTARY NOTES

14 ABSTRACT (200 words or less)

A molten core/material interaction experiment was performed at the Large-Scale Melt Facility at Sandia National Laboratories. The experiment involved the release of 230 kg of core melt, heated to 2923°K, into a magnesia brick crucible. Descriptions of the facility, the melting technology, as well as results of the experiment, are presented. Preliminary evaluations of the results indicate that magnesia brick can be a suitable material for core ladle construction.

15a KEY WORDS AND DOCUMENT ANALYSIS

15b DESCRIPTORS

Molten core
High temperature melts
Magnesia
Core retention

16 AVAILABILITY STATEMENT

Unlimited

17 SECURITY CLASSIFICATION (This report)

Unclassified

18 NUMBER OF PAGES

129

19 SECURITY CLASSIFICATION (This page)

Unclassified

20 PRICE

\$

